

DENSE GAS IN THE MONOCEROS OB1 DARK CLOUD
AND ITS RELATIONSHIP TO STAR FORMATION

by

Grace Annamarie Wolf

Copyright © Grace Annamarie Wolf 1992

A Dissertation Submitted to the Faculty of the

DEPARTMENT OF ASTRONOMY

In Partial Fulfillment of the Requirements
For the Degree of

DOCTOR OF PHILOSOPHY

In the Graduate College

THE UNIVERSITY OF ARIZONA

1 9 9 2

INFORMATION TO USERS

This manuscript has been reproduced from the microfilm master. UMI films the text directly from the original or copy submitted. Thus, some thesis and dissertation copies are in typewriter face, while others may be from any type of computer printer.

The quality of this reproduction is dependent upon the quality of the copy submitted. Broken or indistinct print, colored or poor quality illustrations and photographs, print bleedthrough, substandard margins, and improper alignment can adversely affect reproduction.

In the unlikely event that the author did not send UMI a complete manuscript and there are missing pages, these will be noted. Also, if unauthorized copyright material had to be removed, a note will indicate the deletion.

Oversize materials (e.g., maps, drawings, charts) are reproduced by sectioning the original, beginning at the upper left-hand corner and continuing from left to right in equal sections with small overlaps. Each original is also photographed in one exposure and is included in reduced form at the back of the book.

Photographs included in the original manuscript have been reproduced xerographically in this copy. Higher quality 6" x 9" black and white photographic prints are available for any photographs or illustrations appearing in this copy for an additional charge. Contact UMI directly to order.



University Microfilms International
A Bell & Howell Information Company
300 North Zeeb Road, Ann Arbor, MI 48106-1346 USA
313/761-4700 800/521-0600

Order Number 9307668

**Dense gas in the monoceros OB1 dark cloud and its relationship
to star formation**

Wolf, Grace Annamarie, Ph.D.

The University of Arizona, 1992

Copyright ©1992 by Wolf, Grace Annamarie. All rights reserved.

U·M·I
300 N. Zeeb Rd.
Ann Arbor, MI 48106

DENSE GAS IN THE MONOCEROS OB1 DARK CLOUD
AND ITS RELATIONSHIP TO STAR FORMATION

by

Grace Annamarie Wolf

Copyright © Grace Annamarie Wolf 1992

A Dissertation Submitted to the Faculty of the

DEPARTMENT OF ASTRONOMY

In Partial Fulfillment of the Requirements
For the Degree of

DOCTOR OF PHILOSOPHY

In the Graduate College

THE UNIVERSITY OF ARIZONA

1 9 9 2

THE UNIVERSITY OF ARIZONA
GRADUATE COLLEGE

2

As members of the Final Examination Committee, we certify that we have
read the dissertation prepared by Grace Annamarie Wolf

entitled DENSE GAS IN THE MONOCEROS OBL DARK CLOUD

AND ITS RELATIONSHIP TO STAR FORMATION

and recommend that it be accepted as fulfilling the dissertation
requirement for the Degree of Doctor of Philosophy

Christopher K. Walker
Christopher K. Walker

11/9/92

Date

Charles J. Lada
Charles J. Lada

11/9/92

Date

John H. Black
John H. Black

11/9/92

Date

Robert C. Kennicutt
Robert C. Kennicutt

11/9/92

Date

Date

Final approval and acceptance of this dissertation is contingent upon
the candidate's submission of the final copy of the dissertation to the
Graduate College.

I hereby certify that I have read this dissertation prepared under my
direction and recommend that it be accepted as fulfilling the dissertation
requirement.

Christopher K. Walker
Dissertation Director

Christopher K. Walker

11/9/92

Date

STATEMENT BY AUTHOR

This dissertation has been submitted in partial fulfillment of requirements for an advanced degree at The University of Arizona and is deposited in the University Library to be made available to borrow under the rules of the Library.

Brief quotations from this dissertation are allowable without special permission, provided that accurate acknowledgment of source is made. Requests for permission for extended quotation from or reproduction of this manuscript in whole or in part may be granted by the copyright holder.

SIGNED: Grace Ann Marie Wolf

ACKNOWLEDGMENTS

I could easily make these acknowledgments as long as the dissertation, but time and grad college requirements limit me. Nevertheless, there is no way I can possibly sum up what amounts to a third of my life, not to mention give appropriate credit to those who came before, in one page. Therefore, I suggest that readers interested in this part of the thesis check out Appendix A as well. Even so, I apologize to anyone who gets slighted. I'm afraid I can't possibly list everyone who I feel has had a part in this work individually! I'll do the best I can, in semi-chronological order.

My love of science in general, and astronomy and the space program in particular, began with the 1960's Mercury, Gemini, and Apollo missions, and with a dream (phenomenon?) known as "Star Trek", brought to us by a man named Gene Roddenberry, who I suspect will be remembered for a very long time to come. Although, we have not achieved in space what many of us back then thought we would have by now, I hope I never lose the ideals that began my interest in this field so many years ago. The Tasco 4.5-inch reflector my mother bought me for my sixteenth birthday was a source of unending pleasure during many cold winter nights in the backyard of our house in N.J., but it was during summer vacation in the Catskills that I came to appreciate what really dark skies were about. My high school physics teacher, Mr. Greenberg, deserves special mention.

My years both as an undergraduate at Cornell, and a graduate student at the University of Arizona, evoke many mixed emotions. There have been some pretty dark times, but through it all there have been some very exceptional people to make life bearable even when it wasn't, who have helped me fulfill my dream. From my Cornell years, I want to thank my advisor Joe Veverka, Steve Ostro for getting me started in research, and my friends; in particular, Keith Schroeder for his companionship in the early years following my mother's death, Anne Arrison and Terry Steinberg for their continuing support and thoughtfulness, and Jim DeMarco for always being there and being able to make me laugh.

I owe a very special thanks to Lee and Geneva Emerson who have been "second grandparents" since my mother's death, and are two of the most selfless people it has ever been my pleasure to know. They helped me look out for my grandmother and return to my studies at Cornell subsequent to my mother's death. A lot of self-proclaimed "Christians" could take some lessons from these two on what it really means to live by the teachings of Christ.

DEDICATION

This work is dedicated to the memories of Ruth Schnabel Wolf (1927 - 1977), who for the first nineteen years of my life, was my mother, father, and best friend, and Anna Marie Schnabel (1893 - 1988), my grandmother, who helped raise me. From my mother, I learned to love life, learning, never to give up my dreams, and never to use the word "impossible". How she managed to take care of a child, mother, and house, all on a private duty nurse's salary, and still always have time to spend with me and to give me virtually everything I wanted, certainly all I needed, is beyond me. It saddens me greatly that she didn't live long enough to see me graduate from Cornell and go on ^{to} graduate school. From my grandmother, who was sent to work on a farm at the age of thirteen and never had the opportunity to attend even high school, I learned the differences between knowledge and wisdom, understanding and faith. As grateful as I am for the educational opportunities I've been given, I've come to place a higher value on wisdom. What I learned from both of them is most beautifully summed up in the following quotation:

The Storyteller's Creed: I believe that imagination is stronger than knowledge. That myth is more potent than history. That dreams are more powerful than facts. That hope always triumphs over experience. That laughter is the only cure for grief. And I believe that love is stronger than death.

- Robert Fulghum, "All I Really Need To Know I Learned in Kindergarten"

TABLE OF CONTENTS

LIST OF ILLUSTRATIONS	10
LIST OF TABLES	12
ABSTRACT	13
I. INTRODUCTION	15
1.1. Definition of Outflow	15
1.2. Significance to Protostellar Evolution	16
1.3. Studies to Date	17
1.3.1. Individual Outflows	17
1.3.2. Surveys of Individual GMCs	17
1.4. The Mon OB1 Dark Cloud - Background	18
1.4.1. Molecular Line Observations	19
1.4.2. Unbiased Outflow Survey	23
1.5. Goals of this Thesis	25
II. OBSERVATIONS AND DATA ANALYSIS	28
2.1. Introduction	28
2.2. Observations from the Literature	30
2.3. Observations Done in this Work	30
2.4. LTE Analysis: C ³² S, C ³⁴ S	35
2.4.1. CS Cloud Cores	35

	7
2.4.2. CS Outflows	37
2.5. LTE Analysis: CS 2→1, 5→4, 7→6	38
2.6. Summary	42
III. RELATIONSHIP OF DENSE GAS TO OUTFLOWS	43
3.1. Introduction	43
3.2. CS Morphology	44
3.2.1. CS Spectra	44
3.2.2. Comparison of CS and CO Spectra	56
3.2.3. CS Distribution	63
3.2.4. Comparison of CS, CO, and NH ₃ Distribution	69
3.2.5. Comparison of CS and CO Wing Maps	76
3.3. CS Velocity Structure	81
3.3.1. LV Maps	82
3.3.2. Channel Maps	91
3.4. CS LTE Analysis	102
3.4.1. Cloud Core Masses	103
3.4.2. Outflow Masses and Energetics	104
3.5. CS Dynamical Analysis	110
3.5.1. Observed Centroid Velocity Plots	110
3.5.2. The NCL Cylindrical Structure	114
3.5.3. The SCL CS 5→4 and 7→6 Cores	122
3.6. Comparison of Different Techniques	122
3.7. Summary	124

IV. RELATIONSHIP OF DENSE GAS TO YSOS	127
4.1. Introduction	127
4.2. IRAS Sources	127
4.2.1. Central Object SEDs	127
4.2.2. Association of Dense Gas with Outflows	128
4.2.3. Relationship of Outflow to YSO Evolutionary Stage ..	136
4.3. Summary	140
V. IMPACT OF OUTFLOWS ON CLOUD EVOLUTION	142
5.1. Introduction	142
5.2. Outflow Component within Spectral Line Cores	142
5.3. CS vs. CO Outflow Parameters	144
5.4. Interaction of Outflows with Cores	147
5.5. Evidence for Fossil Outflows	148
5.6. CS Sources Unassociated with CO Flows	153
5.7. Mass Fraction of Cloud Participating in Outflows	153
5.8. Implications for Cloud Support	154
5.9. Summary	155
VI. SUMMARY AND CONCLUSIONS	157
VII. SUGGESTED FUTURE WORK	163
7.1. Unbiased Molecular Cloud Surveys	163
7.2. Surveys for Fossil Outflows	164

APPENDIX A	165
REFERENCES	168

LIST OF ILLUSTRATIONS

Figure 1.1. Mon OB1 cloud, outflows and IRAS sources	22
Figure 2.1. CS 2→1 data points for SCL and NCL	34
Figure 2.2. Optically thin CS line ratio vs. T_{ex}	41
Figure 2.3. Optically thick CS line ratio vs. T_{ex}	41
Figure 3.1. CS 2→1 spectra map for outflow B region	48
Figure 3.2. CS 2→1 spectra map for outflow C region	49
Figure 3.3. CS 2→1 spectra map for outflow D region	50
Figure 3.4. CS 2→1 spectra map for outflow H region	51
Figure 3.5. CS and C ³⁴ S 2→1 spectra for SCL	53
Figure 3.6. CS and C ³⁴ S 2→1 spectra for IRAS 4 and 5	54
Figure 3.7. CS and C ³⁴ S 2→1 spectra for NCL	55
Figure 3.8. Outflow B CO 1→0 and CS 2→1 spectra	59
Figure 3.9. Outflow C CO 1→0 and CS 2→1 spectra	60
Figure 3.10. Outflow D CO 1→0 and CS 2→1 spectra	61
Figure 3.11. Outflow H CO 1→0 and CS 2→1 spectra	62
Figure 3.12. a) SCL CS 2→1 integrated intensity map	66
Figure 3.12. b) NCL CS 2→1 integrated intensity map	66
Figure 3.13. CS 2→1, CS 5→4, and CS 7→6 integrated intensity maps	67
Figure 3.14. 1.3 mm continuum map, CS 5→4, and CS 7→6 peak temperature maps	68
Figure 3.15. SCL CS 2→1, CS 3→2 and 170 μ m, and NH ₃ (1,1) integrated intensity maps	75

Figure 3.16. a) SCL CS 2→1 outflows map	80
Figure 3.16. b) SCL CO 1→0 outflows map	80
Figure 3.17. CS 2→1 Position-velocity maps in RA for SCL	86
Figure 3.18. CS 2→1 Position-velocity maps in DEC for SCL	88
Figure 3.19. CS 2→1 Position-velocity maps in RA for NCL	89
Figure 3.20. CS 2→1 Position-velocity maps in DEC for NCL	90
Figure 3.21. CS 2→1 channel maps for SCL	95
Figure 3.22. CS 2→1 channel maps for NCL	100
Figure 3.23. a) Velocity centroid map for outflow D region	113
Figure 3.23. b) Velocity centroid map for outflow H region	113
Figure 3.24. Illustration depicting the NCL cylinder	120
Figure 3.25. Illustration depicting the SCL outflows and cores	121
Figure 4.1. CS 2→1 integrated intensity vs. IRAS luminosity	132
Figure 4.2. CS 2→1 peak temperature vs. IRAS luminosity	133
Figure 4.3. CS 2→1 integrated intensity vs. IRAS (12 μ /25 μ) temp.	134
Figure 4.4. CS 2→1 peak temperature vs. IRAS (12 μ /25 μ) temperature	135
Figure 5.1. Average CS 2→1 spectrum over outflow H region	151
Figure 5.2. Average CS 2→1 spectrum over entire NCL	151
Figure 5.3. CS 2→1 integrated intensity maps of velocity components and CO outflow H in NCL	152

LIST OF TABLES

Table 2.1. Comparison of beam sizes	33
Table 3.1. CS 2→1 SCL LTE column densities and masses	105
Table 3.2. CS 2→1 NCL LTE column densities and masses	106
Table 3.3. CS 5→4 and 7→6 SCL core LTE column densities and masses	107
Table 3.4. a) CS 7→6 and 5→4 optical depths	108
Table 3.4. b) CS line intensity ratios	108
Table 3.5. CS outflow LTE column densities and masses	109
Table 3.6. CS outflow LTE masses and energetics	109
Table 4.1. a) CS 2→1 detections in Mon OB1	138
Table 4.1. b) CS 2→1 line parameters	139
Table 5.1. Comparison of CO and CS outflow parameters	146

ABSTRACT

We have conducted a CS survey of the 10 outflows and 30 IRAS sources identified by Margulis (1987) in the Mon OB1 dark cloud to study the relationship between outflows, YSOs, and dense cores in this cloud. We have found that the CS $J=2\rightarrow 1$ transition traces a large portion of the dense, low-velocity components of the outflows in Mon OB1. We find the mass of this component to be nearly an order of magnitude greater than previous estimates of the outflow “core” component. We detected little CS gas around the quiescent sources in this cloud. CS $2\rightarrow 1$ temperatures and integrated intensities are 2 to 7 and 2 to 14 times higher, respectively, in the vicinities of IRAS sources associated with outflow activity than about the quiescent sources. This implies CS abundances, temperatures and/or densities are enhanced in regions where outflows impact the ambient cloud. The CS $2\rightarrow 1$ emission is concentrated in two regions encompassing 4 of the 10 previously identified outflows in this cloud. Four of these six outflows are identifiable in CS. Two, previously identified as monopolar outflows, exhibit bipolar structure in CS.

We have detected the CS $J=5\rightarrow 4$ transition in the vicinity of 4 of the 10 outflows in this cloud, and around *none* of the quiescent IRAS sources. The CS $5\rightarrow 4$ emission is extended around two of the outflow sources and has been mapped in these regions. CS $J=7\rightarrow 6$ emission has been mapped about the brightest outflow source in this cloud. The morphology of the $7\rightarrow 6$ region suggests it may have been part of the collimating structure for the outflow associated with this sources. The velocity structure and binding

energies of the $5 \rightarrow 4$ and $7 \rightarrow 6$ cores suggest the outflows are disrupting these cores.

The addition of the low-velocity CS outflow component to previous estimates of outflow energetics implies multiple generations of outflows *need not* be required to support this cloud against collapse. Our results neither support nor rule out the existence of fossil outflows in this cloud. A full-cloud, unbiased survey is required to search for such outflows.

CHAPTER 1

INTRODUCTION

1.1. Definition of Outflow

Outflows around young stellar objects (YSOs) have typically been identified from the asymmetric high velocity wings often observed in CO spectra. These spectra tend to be extremely non-gaussian, and indicate the presence of non-random, bulk motions in the cloud, often involving significant fractions of the masses of the clouds. Studies of the masses and energetics involved in these phenomena indicate central masses required to gravitationally bind the observed mass in a rotational flow are too high (Bally and Lada 1983). These outflows exhibit varying geometries and degrees of collimation, but, in general, tend to be bipolar, with red- and blueshifted gas spatially separate on the sky. The optical depths in the high-velocity gas are often significantly greater than one, but antenna temperatures are typically low. Since optically thick CO is thermalized at H_2 densities of only a couple hundred, this implies the gas is clumpy. Beam-filling factors are often on the order of a tenth. Filling factors tend to be greater in the lower-velocity line wings. The general picture which fits these various characteristics is one in which an initially isotropic stellar or disk wind is collimated by a disk, magnetic field, or some combination of the ambient density and magnetic field structure. As the outflow evolves and sweeps up more and more ambient material, it enters a snowplow

phase, with most of the material lying in a shell which plows into the ambient cloud and surrounds a mostly-evacuated cavity containing some of the higher-velocity material.

In some cases the filling factors in the high-velocity gas are high and the line “wings” become detached from the line core rather than appear as pedestal features. Such is the case for the prototype outflow, L1551, identified by Snell *et al.* (1980). More recently, it has been shown that these “detached wings” may be a common feature of old flows which have swept up large amounts of ambient material, as in the case of Mon R2 (Wolf, Lada, and Bally 1990).

1.2. Significance to Protostellar Evolution

Since the outflow phenomenon appears to be ubiquitous among young stars of one or more solar masses, and involves the transfer of large amounts of energy to the parent molecular clouds, it is apparent that the outflow stage is important to early stellar evolution. It has been suggested that outflows aid infall onto YSOs through centrifugally driven winds that arise due to interaction of material in surrounding accretion disks with frozen-in magnetic fields which thread the disks (eg. Shu *et al.* 1988). These winds carry off angular momentum, slowing the rotation of the disk and allowing accretion from the disk onto the YSO, while clearing the young star of its embryonic cocoon of dust and gas. Outflows may also be responsible for the high degree of turbulence observed in many molecular clouds, support of clouds against large-scale collapse, and regulation of star-forming efficiencies

in molecular clouds.

In order to assess accurately the effects of outflows on molecular clouds and star formation, more needs to be known of the geometry, velocity field, and total energetic input into the parent molecular clouds. Much of the structure of outflows previously studied in CO is lost in the broad line-cores of these spectra, and cannot be separated from the ambient cloud. If, indeed, a large fraction of outflows are moving at relatively low velocities (this is certainly true for outflows which are seen close to the plane of the sky in projection), we are missing a lot of information on the overall structure of these objects.

1.3. Studies to Date

1.3.1. Individual Outflows

Bally and Lada (1983) and Lada (1985) provide good reviews of general outflow characteristics. Early outflow studies were biased toward searching for outflows around the brighter identified infrared sources (IRSs), so the outflows reported in these references tend to be among the most massive and energetic of those currently mapped.

1.3.2. Surveys of Individual GMCs

Although the study of outflows on an individual basis is instructive

for understanding parameters of specific outflows, this approach tells us little of the global significance of this incredible period in the early evolution of stars. To truly understand the total contribution of outflows to the molecular cloud environment, their frequency of occurrence, and their impact on subsequent star formation, it is necessary to study their overall effects in individual molecular clouds.

The present generation of multi-beam and high-sensitivity receivers makes it possible to map fully large portions of molecular clouds in several molecular transitions over reasonable periods of time, thus enabling a much more complete picture of the environment and processes which accompany early stellar evolution. Several surveys of individual clouds have been completed to date. E. Lada conducted an unbiased survey for dense gas in the L1630 (Orion B) molecular cloud (Ph. D. thesis, 1990) to determine the spatial distribution of dense cores, core properties such as size, shape, and mass spectra, and to compare clump and stellar mass spectra to investigate the origin of the initial mass function (IMF). She found that star formation efficiencies were not constant throughout the cloud, and that the bulk of star formation was confined to the 3 most massive dense cores, which collectively account for only 30% of the total mass of dense gas and $\leq 8\%$ of the total gas mass in the surveyed area. Results of the first unbiased CO survey for outflows, upon which this thesis is partially based, will be discussed subsequently.

1.4. The Mon OB1 Dark Cloud - Background

1.4.1. Molecular Line Observations

The Mon OB1 dark cloud was first mapped in CO by Blitz (Ph. D. thesis, 1978) using the Columbia 1.2 m telescope. The large-scale structure of the cloud is shown in Figure (1.1). This figure was taken from Margulis (Ph. D. thesis, 1987). The region of NGC 2264, in the southern portion of this cloud, was mapped in the CO and ^{13}CO $J=1\rightarrow 0$ transitions by Crutcher et al. (1978), using the 4.6 m telescope of the Aerospace Corporation. It has since been studied in a number of different molecules and transitions. Schwartz et al. (1985) mapped a region in the southern portion of the cloud in the vicinity of the open cluster NGC 2264 in the CO $J=1\rightarrow 0$, C^{18}O $J=1\rightarrow 0$, and CS $J=3\rightarrow 2$ transitions at the NRAO 11 m telescope, and in the $\text{NH}_3(1,1)$ and $\text{NH}_3(2,2)$ transitions at the NRAO 43 m telescope.

Krügel et al. (1987) mapped the same region in $\text{NH}_3(1,1)$ and $\text{NH}_3(2,2)$ at the Effelsberg 100 m telescope, and also the immediate vicinity around Allen's star (NGC 2264 IRS) in the CO, ^{13}CO , and C^{18}O $J=1\rightarrow 0$ transitions at the IRAM 30 m telescope, the CO $J=2\rightarrow 1$ transition at the NRAO 12 m telescope, and the CO $J=4\rightarrow 3$ transition using the MPIfR indium antimonide hot electron mixer mounted on the 1.5 m telescope on Mt. Lemmon, Arizona.

Margulis (Ph. D. thesis, 1987) conducted an unbiased CO $J=1\rightarrow 0$ survey for outflows over a large portion of the cloud previously mapped by Blitz, using the NRAO 12 m and FCRAO 14 m telescopes. I will next discuss the results of this survey which lead into some of the research discussed in this thesis. We adopt a distance to Mon OB1 of 800 pc (Walker

1956); the same distance adopted by Margulis. More recent estimates of 700 ± 40 pc and 790 pc are given by Feldbrugge and van Genderen (1991) and Sagar and Joshi (1983) based on VBLUW and UBV photometry of stars in the young cluster NGC 2264.

Fig. 1.1. (Margulis 1987). Schematic diagram of the Mon OB1 molecular cloud overlaid on the POSS red plate of the region. The large irregularly shaped box denotes the region mapped by Margulis in the CO $J=1\rightarrow 0$ transition. The smooth line is the 6 K peak temperature contour. Outflows are indicated by small boxes and were given letter designations by Margulis (not shown) of A to I from south to north. The intermediate-sized box in the southern portion of the cloud denotes a region of extended, low-intensity outflow emission. IRAS sources (+) have number designations (not shown) of 1 to 30 from south to north. The insert is a peak temperature map of the entire cloud complex adopted from Blitz (1978). The contour interval is 1 K.

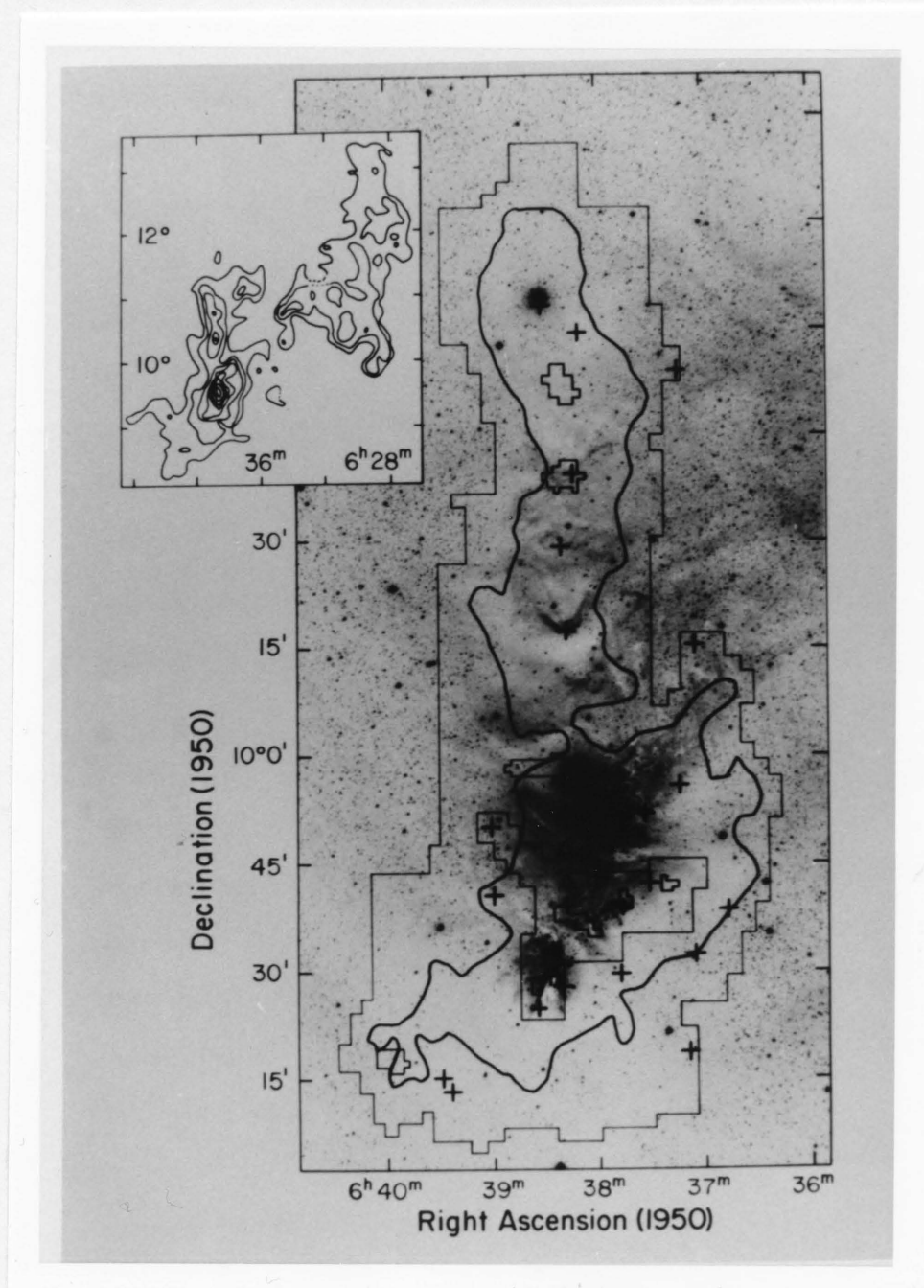


Figure 1.1

1.4.2. Unbiased Outflow Survey

The first unbiased survey for outflows and YSOs over a large portion of a dark cloud was carried out in Mon OB1 by Margulis (1987). Outflows were identified by the presence of high velocity wings in a complete survey of the CO J=1→0 transition. YSOs were identified from the IRAS data. A comparison of the outflows to previously identified outflows was made, a birthrate estimated, and the ability of the outflows to affect cloud structure and dynamics was assessed. Attempts were made to place the YSOs in an evolutionary sequence and to assess the propensity of a YSO to be associated with an outflow. Summarizing his results, Margulis found:

- (1) Nine, later 10 (Hasegawa 1987, private communication) outflows and 30 FIR sources were identified over the extent of the surveyed region, which contains $3 \times 10^4 M_{\odot}$ of gas.
- (2) Four spatially isolated ($< 10'$) regions of high velocity gas were identified, with 5 relatively strong, spatially distinct peaks within an extended region of weak, high velocity emission in the southern portion of the cloud. 19% by area of the portion of the cloud where the CO temperature is > 6 K showed some evidence of high velocity emission, comprising 9% of the entire mapped region.
- (3) It was determined that 6 out of the 9 outflows might be associated with an IRAS source (the tenth outflow may also be associated with an IRAS source). The other 3 may either be associated with sources of significantly lower bolometric luminosity than L1551 IRS 5 or with sources of similar or greater luminosity, but more steeply rising energy distributions.

- (4) If all stars as luminous as the IRAS sources detected in this survey undergo an outflow phase, then since about $\frac{1}{5}$ of these sources are likely to be associated with a high velocity outflow, the sources may spend roughly $\frac{1}{5}$ of their lifetimes in the outflow phase.
- (5) In comparing the Mon OB1 outflows to outflows in general, one distinction that stands out is the lack of bipolarity in 5 of the 9 outflows. These 5 flows exhibit redshifted high velocity gas only. The most likely explanation for this appears to be that the survey was not sensitive enough to detect the blue high velocity emission in these outflows.
- (6) Low mass, low luminosity outflows appear to be more abundant in Mon OB1 than in general, which probably reflects the fact that previous searches for outflows have tended to be made towards luminous YSOs.
- (7) The large total mechanical luminosity of these outflows suggests the possibility of cloud support by the outflows, however, support against gravitational collapse depends upon the efficiency with which the outflows impart energy into the surrounding medium and the ability to spread the mechanical luminosity of the outflows throughout the entire cloud.
- (8) Based on the IRAS luminosity classifications of the YSOs in this study, the outflow phase occurs between Class I and II objects, around the time YSOs lose a large fraction of their circumstellar envelopes. Outflows B and E, which are associated with Class II objects, have the smallest velocities of the source-associated outflows, which is consistent with their being older flows. Class I objects without associated outflow may be pre-outflow objects, perhaps dominated by infall.
- (9) The fossil remains of an old episode of outflow activity were found in

the southern portion of the cloud, indicating outflows expand over 5 - 6 pc before becoming indistinguishable from gas moving at ambient velocity. It was found this component doesn't significantly contribute to the total energy balance in the cloud.

1.5. Goals of this Thesis

After more than ten years of study, some of the most basic questions about the production, collimation, and evolution of molecular outflows are not yet well understood. This thesis will primarily be addressing questions regarding the structure and evolution of outflows by studying their effects in a single molecular cloud.

- 1) How do outflows alter their environments and vice versa?
 - a) How strongly do outflows interact with the ambient cloud cores and what is the effect on the structure and dynamics of both outflow and ambient cloud?
- 2) Is there evidence of more than one outflow epoch among individual YSOs?
 - a) Is there evidence of "fossil" outflows? (Shells of old outflows which are no longer being driven).
- 3) What percent of the ambient molecular gas has been entrained in outflows?
 - a) How much of the outflow material is moving at low velocities, indistinguishable from the ambient gas when CO is used as an outflow probe?

b) Does this help explain why there appears to be a paucity of outflow activity in certain molecular clouds or in certain regions of molecular clouds, or has there been no outflow activity in such regions?

c) Since most of the molecular gas in an outflow is believed to be swept-up ambient gas (Wolf, Lada, and Bally 1990), could lack of sufficient molecular gas in the vicinity of YSOs suggest emission from high velocity gas may just be below present limits of detectability?

The major goal of this work is the investigation of the interrelationship of outflows, YSOs and dense gas within a single molecular cloud. I have searched for the presence of dense gas in the vicinity of all the IRAS sources and outflows in the Mon OB1 cloud which were identified in Margulis' thesis. Where CS was detected in the presence of outflow, it was fully mapped.

At the time of Margulis' survey, outflows were primarily identified by the high velocity wings in CO spectra, with virtually nothing known of the outflow component within the line core. As mentioned earlier, this component may be substantial and we may be missing a significant component of outflows by exclusively using CO as a probe of outflow structure. To effectively determine the full effect of outflows on the molecular cloud environment, one needs to know the full contribution of outflows to cloud energetics. Walker (1988) showed that using dense molecular gas tracers, it is possible to identify and separate out the spectral signatures of the effects of outflow and core rotation. There is indication that a large amount of outflow gas moves at low velocities. There is also

indication that YSOs may go through several generations of outflow activity, and that the older generation or “fossil” outflows may only be detectable at low velocities. Since outflows sweep up more and more ambient cloud material over the course of their lifetimes, outflow material is eventually swept-up into a dense shell at the periphery of the outflow. Such dense shells have been detected in CS (eg. Walker 1990). Is it possible to determine at what densities and sizes we are truly seeing “ambient” gas by multitransitional mapping?

I have studied the dense gas component of all the outflows identified by Margulis in the Mon OB1 dark cloud, and have searched for CS around IRAS sources in notably quiescent regions of this cloud, where no outflows were detected, in an attempt to study the entire outflow contribution to the energetics of the cloud, the interaction of the outflows with the ambient cloud environment, and to determine the presence of CS gas in outflow vs. quiescent parts of the cloud.

CHAPTER 2

OBSERVATIONS AND DATA ANALYSIS

2.1. Introduction

In this chapter, we will discuss the molecular line observations carried out in this work, observations which have been used or referred to from prior work, and the LTE analysis performed to calculate physical parameters of the molecular gas. In the following chapter we will compare our results with prior analyses available for this cloud, as well as dynamical analyses of the cloud components we have mapped. The purpose of this chapter is to describe the LTE analysis used to obtain column densities and masses of the dense gas component in order to assess the contribution of this component to the overall dynamics in this cloud.

We have searched for CS gas in the vicinity of all the known outflows and IRAS sources in this cloud. The initial survey was carried out using the $J=2\rightarrow 1$ and $J=5\rightarrow 4$ transitions of CS. Two extended regions of CS $J=2\rightarrow 1$ emission were identified in Mon OB1, which will be referred to as the South Cloud (SCL) and the North Cloud (NCL) throughout this thesis. The SCL contains two bright clumps of emission which were also detected in the $J=5\rightarrow 4$ transition. The southern clump peaks on Allen's IRS, the brightest infrared source in Mon OB1. This clump was also detected and mapped in the $J=7\rightarrow 6$ transition of CS. The $7\rightarrow 6$ transition was not detected to the 230 mK level in the vicinity of the clump to the northwest.

These two clumps are situated in the regions occupied by the two most massive outflows in Mon OB1, which also carry the most momentum. This is not surprising as one would expect an outflow which has accumulated a large amount of matter to have access to a dense reservoir of gas.

The critical excitation density for a transition is given by

$$n_c(H_2) = \frac{A_{ul}}{\Sigma \gamma_{ul}(1 - e^{-h\nu/kT})},$$

where A is the spontaneous transition rate and γ is the collisional rate coefficient. $\gamma_{ul} = C_{ul}/n$, where C is the collisionally induced transition rate and n is the volume density of collision partners. The exponential term is the correction for the stimulated emission at the temperature of the radiation field. As the CS transitions have much shorter lifetimes than CO, the critical densities for excitation are several orders of magnitude larger for the CS transitions. For the CS J=2→1 transition, the critical density $n_c \approx 2.2 \times 10^5 \text{ cm}^{-3}$ for $T \approx 10 \text{ K}$. The three most massive CO outflows (B, C, and D) are located in the SCL and show up prominently in the CS J=2→1 spectra and spatial distribution of the gas. The morphology of the CS spectra suggest that a fourth outflow (H) located in the NCL, is dramatically affecting the structure of the ambient gas in this region. This suggests these outflows have swept up a considerable amount of ambient gas into dense shells.

To determine the contribution of the dense gas component to the molecular outflows in Mon OB1, I have used an LTE analysis on the C³²S J=2→1 and C³⁴S J=2→1 data. Estimates of the gas optical depth, excitation temperature, (T_{ex}), column density, (N_ν), and mass were obtained.

I have performed a conventional analysis of the energetics of the outflows in this cloud. These data were also used to perform an analysis on the core gas component, along with the CS $J=5\rightarrow4$ and $J=7\rightarrow6$ data available for the two clumps in the SCL.

2.2. Observations from the Literature

Table 2.1 gives a comparison of beam sizes at different frequencies and different telescopes for observations that are used, compared, or referred to in this thesis. Blitz (1978) mapped the large-scale CO structure of the Mon OB1 cloud depicted in Figure (1.1). In Chapter 3, we compare the CS $3\rightarrow2$ and $170\ \mu\text{m}$ maps of Schwartz et al. (1985) and $\text{NH}_3(1,1)$ map of Krügel et al. (1987) to our CS $2\rightarrow1$ map of the region we have designated as the SCL. Our CS $5\rightarrow4$ and $7\rightarrow6$ maps are compared to the $1.3\ \text{mm}$ continuum map of Walker et al. (1990). We compare the morphology of our CS $2\rightarrow1$ spectra and wing maps to the CO $1\rightarrow0$ spectra and wing maps of Margulis to determine the CS outflow components in Mon OB1.

2.3. Observations Done in this Work

The CS $J=2\rightarrow1$ and $\text{C}^{34}\text{S } J=2\rightarrow1$ data were acquired at the $12\ \text{m}$ mm wave telescope operated by NRAO and located on Kitt Peak near Tucson, Arizona. Data were obtained in September and October 1986, October 1990, and May and December 1991. The beamsize of the telescope at $98\ \text{GHz}$ is approximately $64''$. The data were taken by position switching

to an absolute off position. (Four off positions were used in mapping the Mon OB1 cloud due to the cloud's 2° extension in declination). Most of the data were obtained with a dual-channel 3 mm SIS receiver. The backend spectrometer consisted of 100 kHz and 250 kHz filterbanks that yielded respective velocity resolutions of 0.31 and 0.76 km s $^{-1}$. The September 1986 data were taken using a 3 mm cooled Schottky receiver. Data were calibrated by chopping between sky and an ambient temperature load. M17SW was used as a calibration source for the 1986 data and Orion A was used as a calibration source for the 1990 and 1991 data. For M17SW, temperatures were checked against T_R^* values for M17SW given by Snell et al. (1984). For Orion A, CS 2 \rightarrow 1 T_R^* values were typically about 12 K. Line temperatures and pointing were double-checked by returning to the map center position several times during an observing session. The line profiles near the central positions of the two large mapped cloud components are quite distinctive, and change fairly dramatically over small spatial distances, so this procedure served as a good double-check of the pointing obtained using planets, which were not always available. CS J=2 \rightarrow 1 data points acquired for the regions referred to as the SCL and NCL are shown in Figure (2.1), and will be omitted from contour plots of these regions in subsequent chapters. Positional offsets are in arcminutes.

Some CS J=5 \rightarrow 4 data were also acquired at the 12 m in April 1986 and February 1987. Detections were made in the vicinity of four energetic outflows in Mon OB1 (C and D in the SCL; O and H in the NCL). No detections were made around any of the IRAS sources unassociated with outflow activity.

The remainder of the CS J=5→4 and the CS J=7→6 data were acquired at the 10.4 m Caltech Submillimeter Observatory on Mauna Kea, Hawaii in April, September and October 1991 with the 200 to 270 GHz and 300 to 360 GHz SIS receivers. Two acousto-optical spectrometers (AOSs) were used for the receiver backend. The AOS bandwidths were 500 and 50 MHz. Each AOS was divided up into 1000 channels. The 500 MHz AOS allows for simultaneous reception of both the CS J=7→6 line at 343 GHz and the CO J=3→2 line at 345 GHz.

The antenna temperature scales used at the NRAO 12 m and CSO 10.4 m are T_R^* and T_A^* , respectively, where $T_R^* = T_A^*/\eta_{fss}$. η_{fss} is the correction for losses due to forward spillover and scattering. All of the temperature and integrated intensity maps we present of our data in this work have been corrected for the different beam parameters at these telescopes.

The molecular line observations are used to probe conditions in the outflow and ambient gas components. Both components are seen, and may to some extent be disentangled, in the CS J=2→1 data. As will be discussed in the next chapter, there is some evidence that outflow is detected even in the CS J=5→4 data. In the remaining sections of this chapter, I will discuss the LTE analysis used to probe the dense components of the outflows as well as the dense core components in Mon OB1.

TABLE 2.1. COMPARISON OF BEAM PARAMETERS

Work	Telescope	Transition(s)	Beam
Blitz (1978)	Columbia 1.2 m	CO(1-0)	8.7'
Crutcher et al. (1978)	AC 4.6 m	CO, ¹³ CO(1-0)	2.6'
Schwartz et al. (1985)	NRAO 11 m KAO	CS(3-2) 170 μ m continuum	50" 72"
Kr�gel et al. (1987)	IRAM 30 m NRAO 12 m Bonn 100 m	CO, ¹³ CO,C ¹⁸ O(1-0) CO(2-1) NH ₃ (1,1),(2,2)	21" 30" 40"
Margulis (1987,1988)	NRAO 12 m FCRAO 14 m	CO(1-0) CO(1-0)	55" 45"
Walker et al. (1990)	NRAO 12 m	1.3 mm continuum	30"
Wolf (1992)	NRAO 12 m CSO 10.4 m	CS,C ³⁴ S(2-1) CS(5-4) CS(5-4) CS(7-6),CO(3-2)	64" 26" 29" 21"

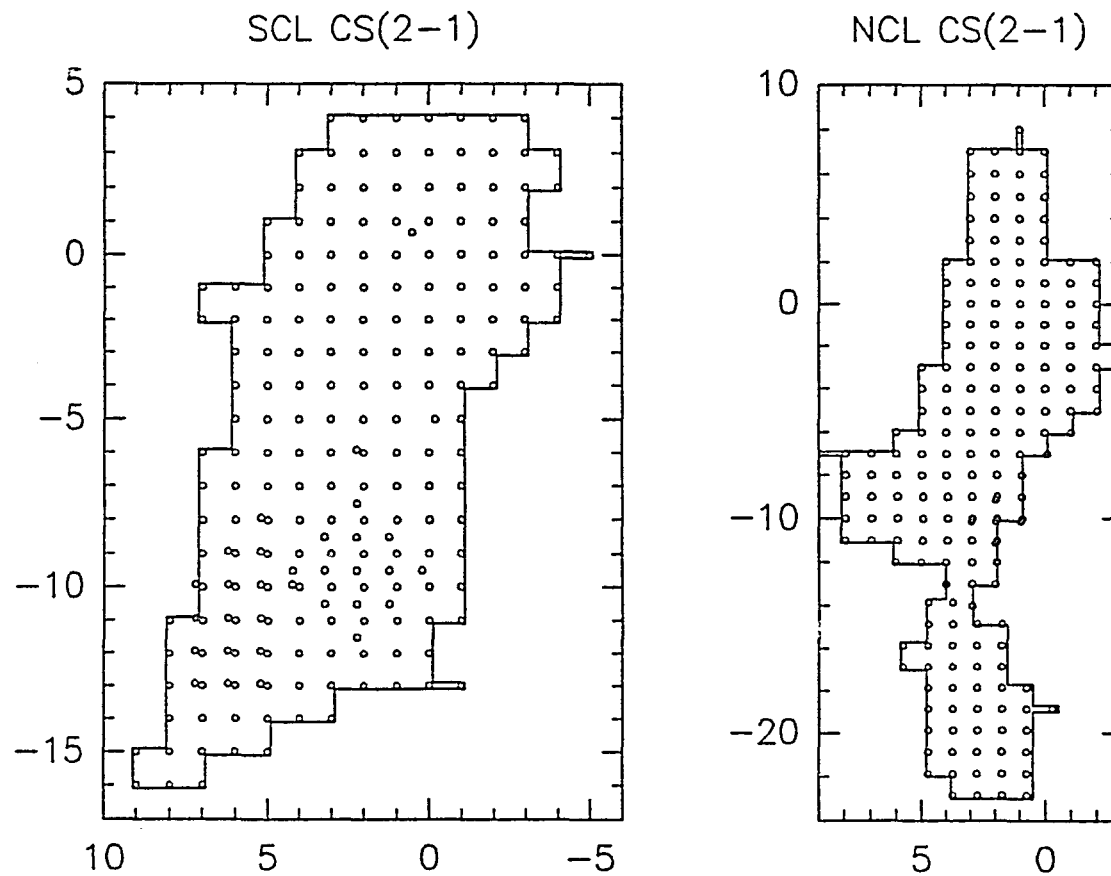


Fig. 2.1. CS 2 \rightarrow 1 data points obtained in the SCL and NCL. The units of the horizontal and vertical axes are RA and Dec offsets in arcminutes, respectively. The (0,0) position for the SCL is at $\alpha_{1950} = 6^h 38^m 16^s$ and $\delta_{1950} = 9^\circ 38' 23''$, and for the NCL, $\alpha_{1950} = 6^h 38^m 10^s$ and $\delta_{1950} = 10^\circ 39' 30''$. Positional offsets are in arcminutes.

2.4. LTE Analysis: C³²S, C³⁴S

The LTE approximation assumes an equal excitation temperature among different transitions equal to the gas kinetic temperature. C³⁴S J=2→1 data were obtained at the positions of several IRAS sources and outflow centers where bright CS J=2→1 lines were observed. From these data, gas optical depths, excitation temperatures, and column densities were estimated. The total gas mass in the regions where CS gas was observed was then calculated over velocity ranges corresponding to outflow and “ambient” cloud emission. We will discuss some of the problems with the LTE assumption, particularly for the higher transitions, in Chapter 3, where we present the results of this analysis.

2.4.1. CS Cloud Cores

We calculated the masses of the SCL and NCL by assuming equal excitation temperatures and line broadening for the C³²S and C³⁴S J=2→1 transitions, and a solar abundance ratio ³²S/³⁴S = 22.6. The optical depth of the observed CS transition was determined from the ratio of C³²S and C³⁴S integrated intensities:

$$\frac{\int T_R^*(C^{32}S)dv}{\int T_R^*(C^{34}S)dv} = \frac{1 - \exp(-22.6\tau_{2-1}^{34})}{1 - \exp(-\tau_{2-1}^{34})}. \quad (2.1)$$

The excitation temperature was determined from the line intensity:

$$J(T_B^{34}) = f[J(T_{ex}) - J(2.7)][1 - \exp(-\tau_{2-1}^{34})], \quad (2.2)$$

where T_B is the source brightness temperature and $J(T_B^{34}) = T_R^{34}$, the effective source radiation temperature. $T_R^{34} = T_R^{*34}/\eta_c$ where η_c is the beam coupling efficiency of the telescope, and f is the beam filling factor. When f is taken to be unity, the above equation yields a lower limit for T_{ex} .

For an optically thin transition, the general expression for the column density is:

$$N_\nu = \frac{8\pi\nu_{ul}^2}{c^2} \frac{\tau_{ul}}{A_{ul}} \frac{g_l}{g_u} \frac{2k(l+1)(T_{ex} + \Delta)}{h\nu_{ul}(2l+1)} \left[1 - \exp\left(\frac{-h\nu_{ul}}{kT_{ex}}\right) \right]^{-1} \exp\left[\frac{h\nu_{ul}}{kT_{ex}} \frac{l}{2}\right]$$

Here, u and l designate the upper and lower states of the transition, respectively, g_u and g_l are the statistical weights, and ν_{ul} and τ_{ul} are the frequency and optical depth of the transition, respectively. The optical depth here is the mean optical depth, not the optical depth over the entire line. To obtain the contribution to column density at all velocities in the line, we need to integrate the optical depth over the line profile. This amounts to multiplying both sides of the above equation by $\Delta\nu$, $N_{tot} = N_\nu \Delta\nu$. This expression may be put in terms of velocity rather than frequency: $\Delta\nu = \frac{\nu_{ul}\Delta v}{c}$, where Δv is the velocity full-width of the line at half-maximum.

For the $C^{34}S$ $J=2 \rightarrow 1$ transition, the expression for the column density becomes:

$$N_v^{34} = 2.80 \times 10^6 \tau_{2-1}^{34} (T_{ex} + \Delta) \left[1 - \exp\left(\frac{-4.63}{T_{ex}}\right) \right]^{-1} \exp\left[\frac{2.31}{T_{ex}}\right] \nu_{2-1} \frac{\Delta v}{c},$$

where Δ is a correction factor for a finite number of states. The correction factor arises because the partition function is summed over an infinite

number of states. When the term hB/kT_{ex} is small, the summation may be approximated by an integral. (B is the rotational constant of the transition in Hertz). More accurate determinations of the partition function can be formed by summing the terms for an assumed T_{ex} until higher rotational levels no longer contribute significantly and the resulting partition function may be expressed as a deviation from T_{ex} . For the $C^{34}S(2-1)$ transition, the difference between the two estimates of the partition function is small and amounts to a correction factor of $\Delta \approx 0.35$ for $T_{ex} \approx 30$ K. This equation applies if T_{ex} is constant for all levels or the system is in LTE and $T_{ex} = T_k$. To convert N_v^{34} to the total hydrogen column density, we used the abundance factor given by Graedel, Langer, and Frerking (1982): $CS/H_2 = 1.6 \times 10^{-9}$ and the terrestrial $C^{32}S/C^{34}S$ abundance ratio of 22.6.

$C^{34}S$ data were obtained only for a limited number of positions. Therefore, to calculate the mass of the gas in the SCL and NCL, the assumption was made that the gas column density at a given position scales with the observed $C^{32}S$ integrated intensities. The mass of a given cloud is then given by $M = fA_w m_{H_2} N_{H_2}$, where A_w is the emission weighted area and f is the filling factor.

2.4.2. CS Outflows

The integrals in Equation (2.1) are performed over the line wings to calculate an average optical depth for the gas participating in outflow. Where the $C^{34}S$ line wings were undetectable at the 50 mK level, the CS emission was assumed to be optically thin and the ratios of the line

intensities to be equal to the ratios of the optical depths, so lower limits for the column densities and masses could be obtained. The column densities have been calculated over the velocity range of the wing emission. The masses obtained were used to calculate outflow energetic parameters following the conventions used in Bally and Lada (1983).

The dynamical timescale for an outflow, τ_d , is computed from the outflow radius R , taken to be $(R_{max}R_{min})^{1/2}$, where R_{max} and R_{min} are the major and minor flow axes, and a characteristic velocity V_{ch} , taken to be close to the largest observed flow velocity. Other energetic parameters determined include the momentum $P (= MV_{ch})$, the momentum supply rate $\dot{P} (= MV_{ch}/\tau_d)$, the kinetic energy of the outflow, $E (= MV_{ch}^2/2)$, and the energy supply rate or mechanical luminosity $L (= E/\tau_d)$.

If the driving source of an outflow has turned off at some point in the past, the outflow is momentum driven. It will continue to sweep up mass as it slows down, conserving momentum. If energy is being pumped into an outflow, it is energy driven and slows down while conserving energy.

2.5. LTE Analysis: CS 2→1, 5→4, 7→6

It is possible to do the same kind of analysis on the CS J=5→4 and 7→6 data as was done in the previous section with the CS J=2→1 data. Unfortunately, no C³⁴S isotope data were obtained for these transitions. However, we can place a lower limit on the C³²S column densities by assuming the CS is optically thin. In the next chapter, I present tables of the results of this analysis.

It is also possible to compare the CS $J=2 \rightarrow 1$, $J=5 \rightarrow 4$, and $J=7 \rightarrow 6$ data directly if we make the assumption that all of these transitions are characterized by a single excitation temperature. However, since these transitions probe different density regimes and hence different parts of the cloud cores, this assumption is probably invalid.

Since the multitransitional data were taken at different telescopes and frequencies, the data must be properly calibrated for different beam parameters. Also, a direct comparison of line parameters is only possible where data are observed with similar beam sizes. Therefore, I have convolved my CS $J=5 \rightarrow 4$ and $J=7 \rightarrow 6$ data to the $J=2 \rightarrow 1$ beam size to compare line temperatures and integrated intensities.

Referring back to Equation (2.2) for the intensity of a millimeter line, the ratio of line intensities for two transitions whose lower states are given by i and j is:

$$\frac{T_b^{j+1,j}}{T_b^{i+1,i}} = \frac{[J_{j+1,j}(T_{ex}) - J_{j+1,j}(2.7)][1 - \exp(-\tau_{j+1,j})]}{[J_{i+1,i}(T_{ex}) - J_{i+1,i}(2.7)][1 - \exp(-\tau_{i+1,i})]}. \quad (2.3)$$

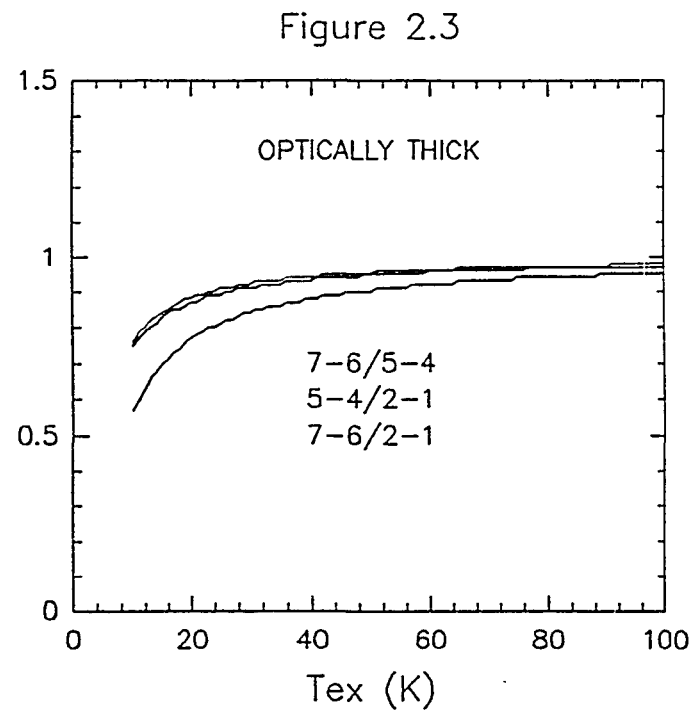
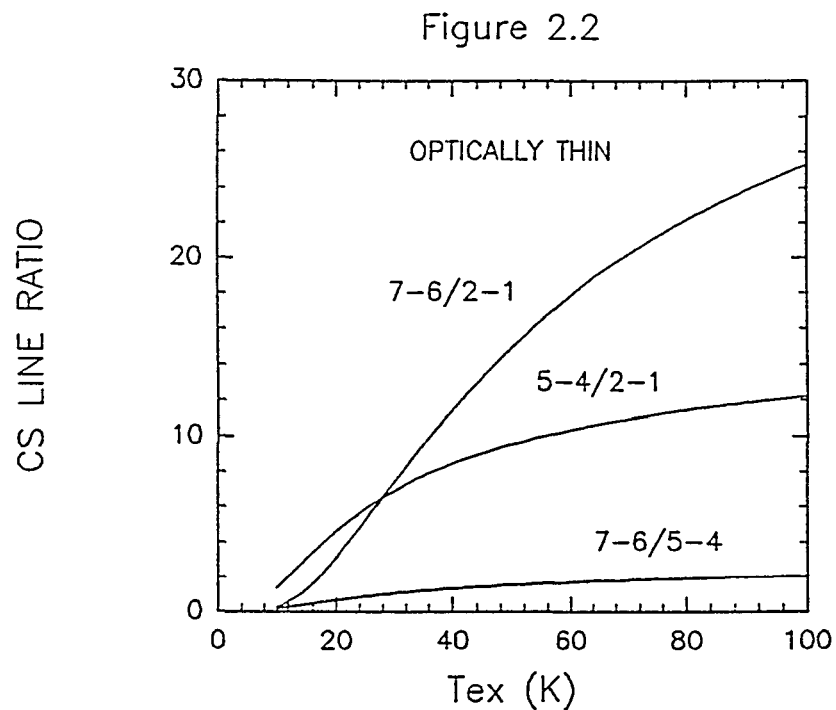
This assumes that filling factors are the same for both transitions. In the optically thick limit, where $\tau \gg 1$ for both transitions, the exponential term drops out of the above equation. In the optically thin limit, where $\tau \ll 1$ for both transitions, the above equation simplifies to:

$$\frac{T_b^{j+1,j}}{T_b^{i+1,i}} = \frac{[J_{j+1,j}(T_{ex}) - J_{j+1,j}(2.7)]\tau_{j+1,j}}{[J_{i+1,i}(T_{ex}) - J_{i+1,i}(2.7)]\tau_{i+1,i}}.$$

The ratio of the optical depths of two transitions simplifies to:

$$\frac{\tau_{j+1,j}}{\tau_{i+1,i}} = \frac{\nu_{j+1,j}^2}{\nu_{i+1,i}^2} \left[\frac{1 - \exp(-h\nu_{j+1,j}/kT_{ex})}{1 - \exp(-h\nu_{i+1,i}/kT_{ex})} \right] \frac{\exp(-jh\nu_{j+1,j}/2kT_{ex})}{\exp(-ih\nu_{i+1,i}/2kT_{ex})}.$$

Figures 2.2 and 2.3 show the line intensity ratios for the optically thin and thick cases as functions of excitation temperature for the CS $2 \rightarrow 1$, $5 \rightarrow 4$, and $7 \rightarrow 6$ transitions. The observed line ratios may be used to estimate the excitation temperature. Figure 2.2 is identical to plotting the optical depth ratio vs. excitation temperature, since in the optically thin limit the line intensities scale as the optical depths. Since CS $2 \rightarrow 1$ optical depths were calculated using the available isotope data, it is possible to estimate the optical depths for the higher transitions in these regions. Observed and theoretical line intensity ratios will be compared.



Figs. 2.2. - 2.3. Line intensity ratio as a function of excitation temperature for the optically thin and thick cases. Curves are drawn for CS $7 \rightarrow 6/2 \rightarrow 1$, $7 \rightarrow 6/5 \rightarrow 4$, and $5 \rightarrow 4/2 \rightarrow 1$ ratios.

2.6. Summary

We have conducted a survey for dense gas in Mon OB1 using the CS $2\rightarrow 1$, $5\rightarrow 4$, and $7\rightarrow 6$ transitions to probe different regions of the cloud. We have performed an LTE analysis to estimate the mass and energetics of the outflows observed in the $2\rightarrow 1$ transition and to probe conditions in the densest regions of the SCL cores using the $5\rightarrow 4$ and $7\rightarrow 6$ transitions. In Chapter 3, we present the results of this analysis.

CHAPTER 3

RELATIONSHIP OF DENSE GAS TO OUTFLOWS

3.1. Introduction

As discussed in Chapter 1, dense gas in molecular clouds is often associated with YSOs which have formed in these cores. It is reasonable to question whether this gas always traces the ambient core regions in molecular clouds, or whether this component may often trace the dense, swept-up shells of material that are formed as molecular clouds evolve. Little is known of the outflow gas component which is masked by ambient gas in the core region of spectral lines. In this chapter, we will attempt to determine what percent of outflow gas lies in this region. We will attempt to sort out the amount of this gas participating in outflow from the amount of dense gas which can truly be termed “ambient” gas. Through mapping the densest regions of this cloud in the higher rotational transitions of CS, we hope to determine at what level we may find evidence of the original structures which collimated the outflows.

In this chapter, we will investigate the morphology and dynamics of the dense gas in Mon OB1, and its relationship to the CO outflows in this cloud. The analytical techniques described in the previous chapter are used to determine the contribution of the dense gas component to the outflows and to probe conditions in the densest core regions. The LTE results are compared with a dynamical analysis of the cores. Where possible, we

compare our results with results from the literature. A method is discussed for sorting out the effects of outflow and core dynamics.

3.2. CS Morphology

In the following sections, I will discuss the spatial and velocity distributions of the CS cores and outflows found in the SCL and NCL. To minimize confusion, we follow the same IRAS source and outflow designations as Margulis (1987). Outflows B, C, and D are located in the SCL and have been associated with IRAS sources 6, 9, and 12, respectively. Outflow H and an outflow we have designated as “O” are located in the NCL and are associated with IRAS sources 27 and 25, respectively. One other source, IRAS 26, is located near the center of the NCL in a region nearly devoid of CS emission and has no associated outflow. These outflows and IRAS sources will be referred to repeatedly throughout this work.

3.2.1. CS Spectra

Figures (3.1) to (3.4) are CS $J=2\rightarrow 1$ spectra maps of the regions around IRAS 6, 9, and 12 in the SCL and IRAS 27 in the NCL. These IRAS sources are associated with outflows B, C, D, and H, respectively. The CS spectra in these regions are extremely non-gaussian and exhibit the broad line wings indicative of outflows. The very broad, strongly self-absorbed line in the spectra map of the outflow D region marks the approximate center of the outflow. Much of the gas to the redshifted side

of the self-absorption dip has been swept-up and entrained in the outflow. The spectra map of the outflow H region is especially interesting. The self-absorption dip in the CS spectra flips from the red- to blueshifted side of the spectra across RA offsets 2 and 1, indicative of rotation about a N - S axis. This will be discussed in detail in Section (3.3).

Figures (3.5) to (3.7) are CS and $C^{34}S$ $2 \rightarrow 1$ spectra at all positions where $C^{34}S$ data were obtained. Figure (3.5) shows the spectra which were used in the LTE core and outflow mass computations for the SCL. Figure (3.6) shows the spectra obtained at the positions of two IRAS sources which lie near the southern end of the SCL. Figure (3.7) shows the spectra which were used in the LTE mass computations for the NCL. Asymmetric line wings are present in most of the $C^{34}S$ spectra as well as the $C^{32}S$ spectra.

The spectra displayed in Figure (3.5) were used to help identify the contribution of the dense, low-velocity outflow gas in the SCL. Redshifted outflow gas is present at the position of IRAS 9 and is associated with outflow C. Red- and blueshifted outflow gas is present in the vicinity of outflow B, which is probably associated with IRAS 6. The spectra labelled "OUTFLOW D" were taken at a positional offset of $(1', -1')$ from the position we adopted for IRAS 12. The difference in the appearance of the spectra over a distance corresponding to just a little over a beamwidth is striking! At outflow D, the $C^{34}S$ spectrum shows two components. One is at approximately the same velocity as the single line component at IRAS 12 (although perhaps slightly redshifted, indicating the presence of a velocity gradient, possibly due to rotation of the ambient cloud). The other corresponds to the velocity of the self-absorption feature in the $C^{32}S$

spectrum, *not* to the velocity of the other component seen in the C^{32}S spectrum at this position. The considerable asymmetric red wing seen in the C^{34}S spectrum suggests a considerable amount of the ambient gas has been entrained in the outflow.

The spectra displayed in Figure (3.6) were obtained at the positions of two weak IRAS sources located in the southern extension of the SCL, which will be discussed along with the general morphology of the SCL in Section (3.2.3). The spectra at the southern boundary of this region exhibit a complex, multi-velocity component structure.

The spectra displayed in Figure (3.7) were obtained at the centers of outflows H and O. Blueshifted outflow gas is evident in the C^{32}S spectrum in the vicinity of outflow H, but most of the CS emission in this region comes from the structure described in the first paragraph of this section. Redshifted outflow gas is evident in the C^{32}S spectrum in the vicinity of outflow O, but the CS emission in this region is very confined (Figure 3.12).

Fig. 3.1. CS 2→1 spectra map of the region surrounding IRAS 6 and associated with outflow B. Offsets are in arcminutes from the position $\alpha_{1950} = 6^h 38^m 16^s$ and $\delta_{1950} = 9^\circ 38' 23''$. The velocity scale for each spectrum is -6 to 20 km s⁻¹; the temperature scale for each spectrum is -1 to 5 K.

Fig. 3.2. CS 2→1 spectra map of the region surrounding IRAS 9 and associated with outflow C. Offsets are in arcminutes from the position $\alpha_{1950} = 6^h 38^m 16^s$ and $\delta_{1950} = 9^\circ 38' 23''$. The velocity scale for each spectrum is -6 to 20 km s⁻¹; the temperature scale for each spectrum is -2 to 7 K.

Fig. 3.3. CS 2→1 spectra map of the region surrounding IRAS 12 and associated with outflow D. Offsets are in arcminutes from the position $\alpha_{1950} = 6^h 38^m 16^s$ and $\delta_{1950} = 9^\circ 38' 23''$. The velocity scale for each spectrum is -6 to 20 km s⁻¹; the temperature scale for each spectrum is -1 to 5 K.

Fig. 3.4. CS 2→1 spectra map of the region surrounding IRAS 27 and associated with outflow H. Offsets are in arcminutes from the position $\alpha_{1950} = 6^h 38^m 10^s$ and $\delta_{1950} = 10^\circ 39' 30''$. The velocity scale for each spectrum is -6 to 20 km s⁻¹; the temperature scale for each spectrum is -0.5 to 2.5 K.

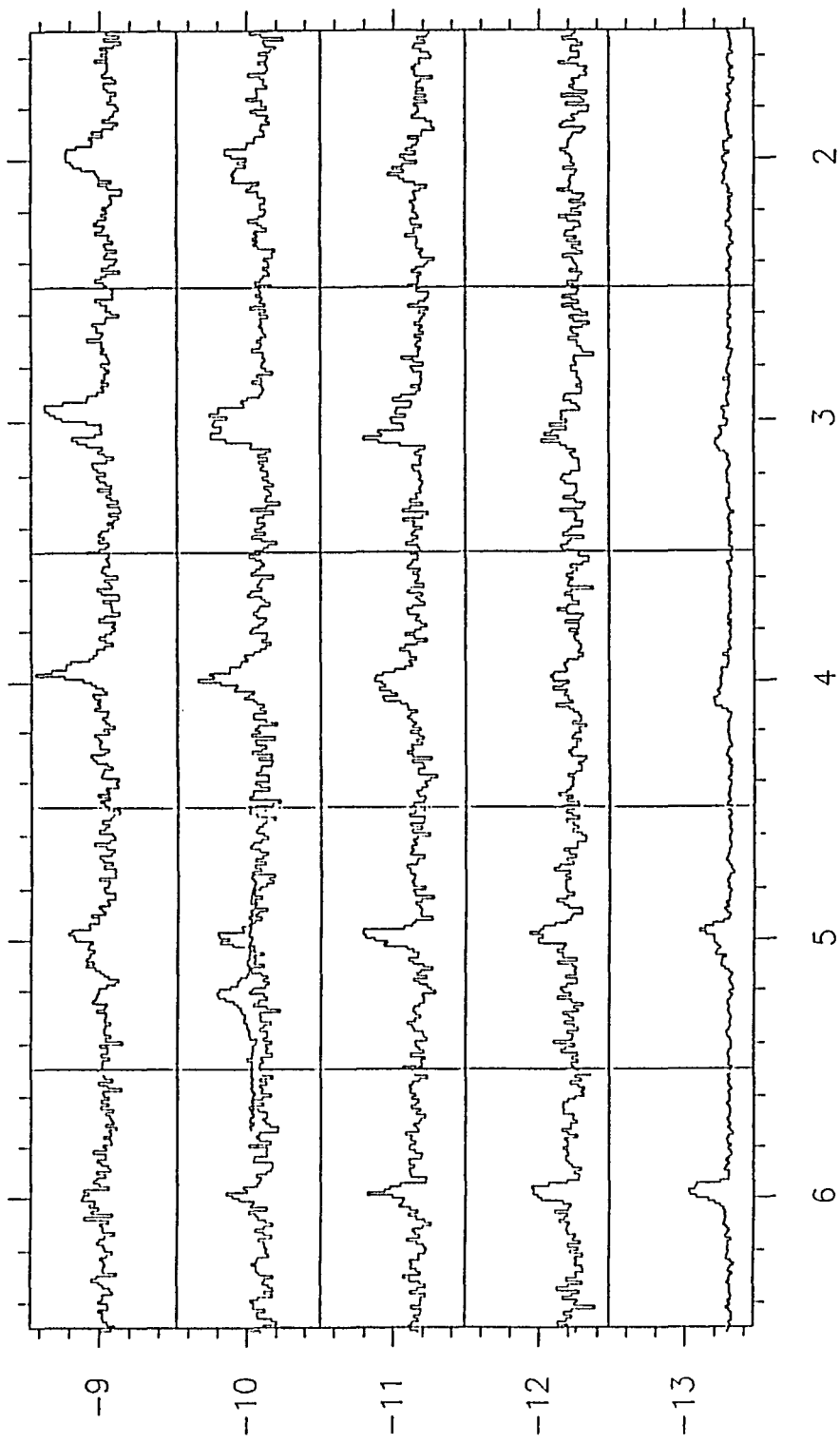


Figure 3.1

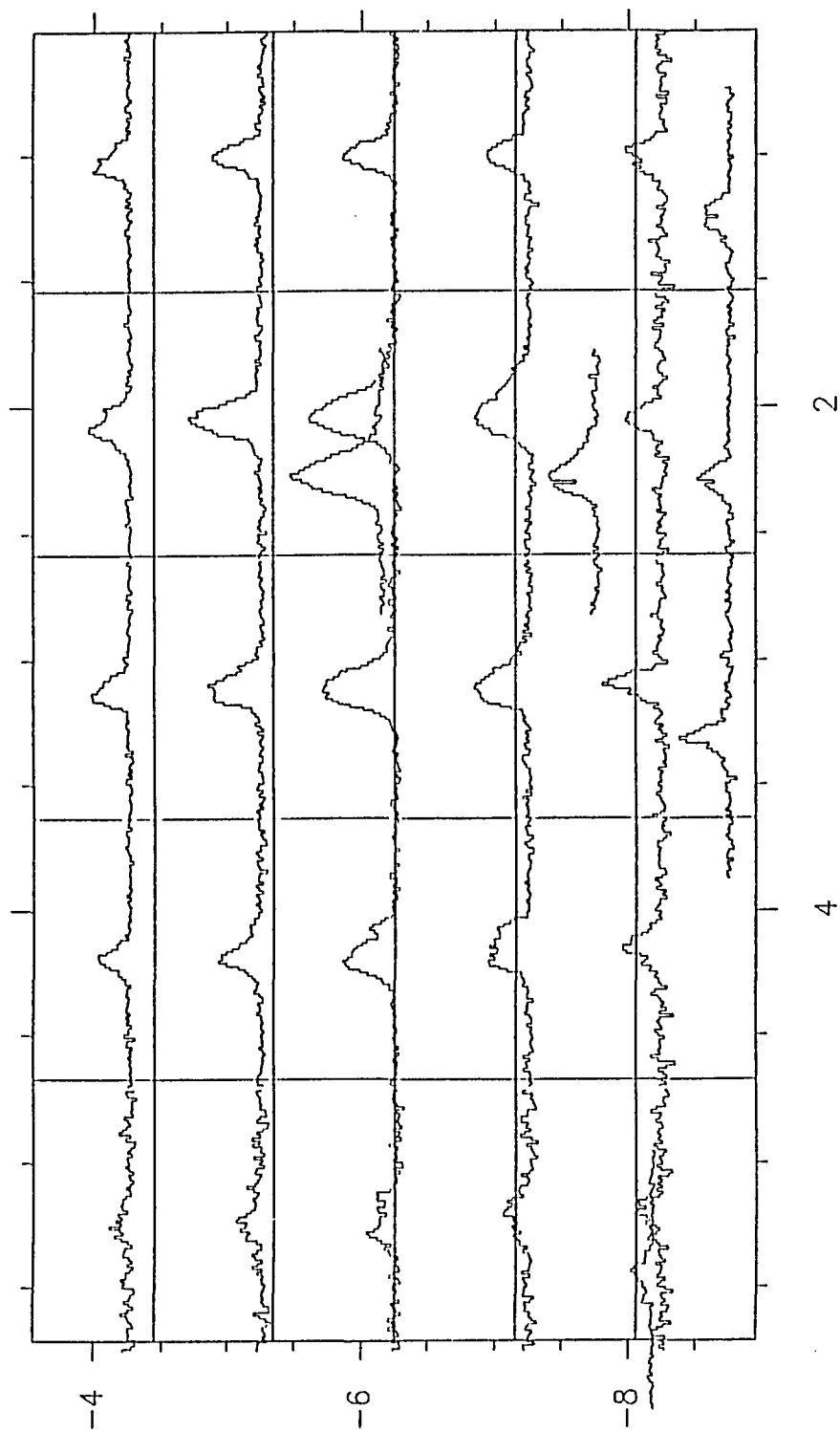


Figure 3.2

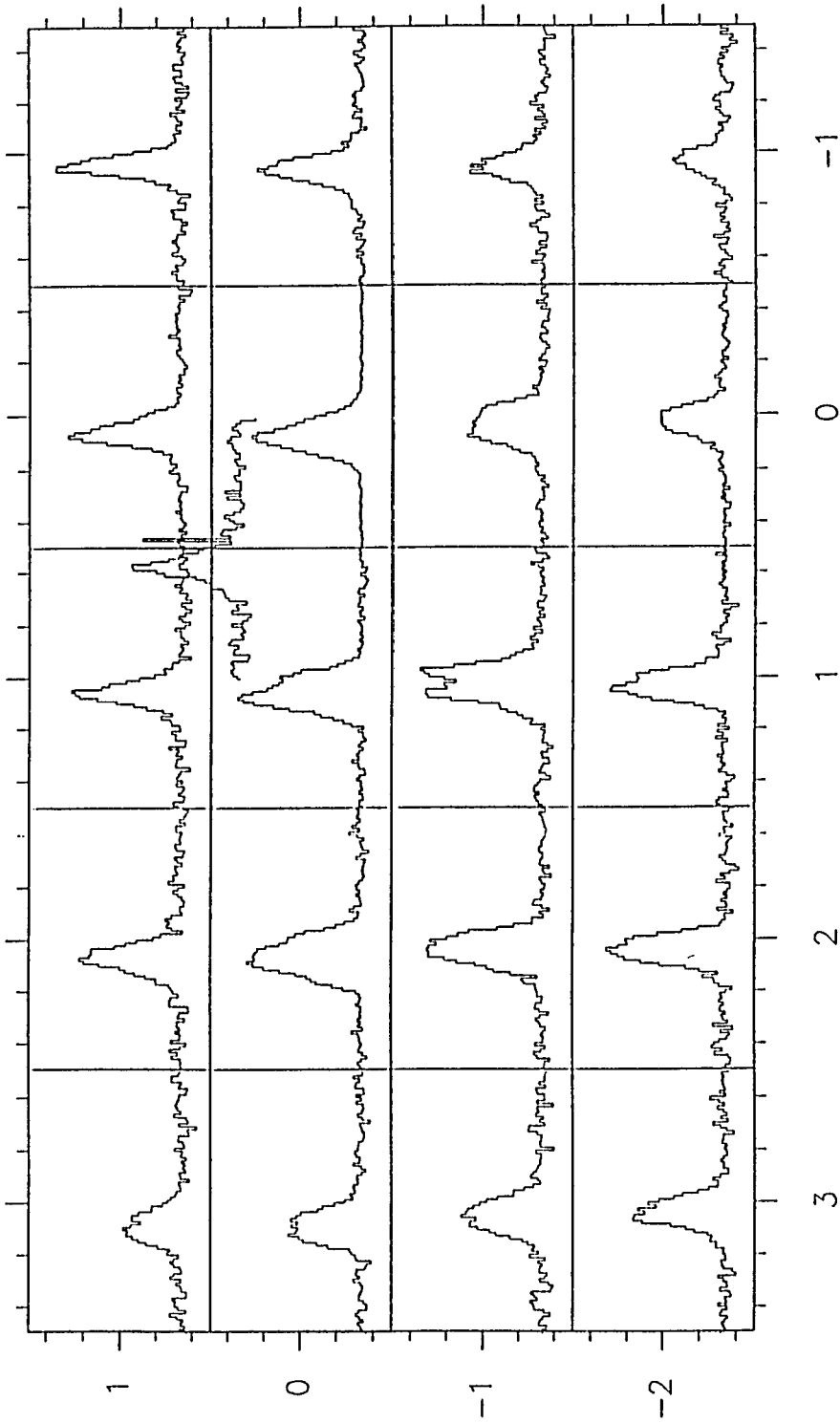


Figure 3.3

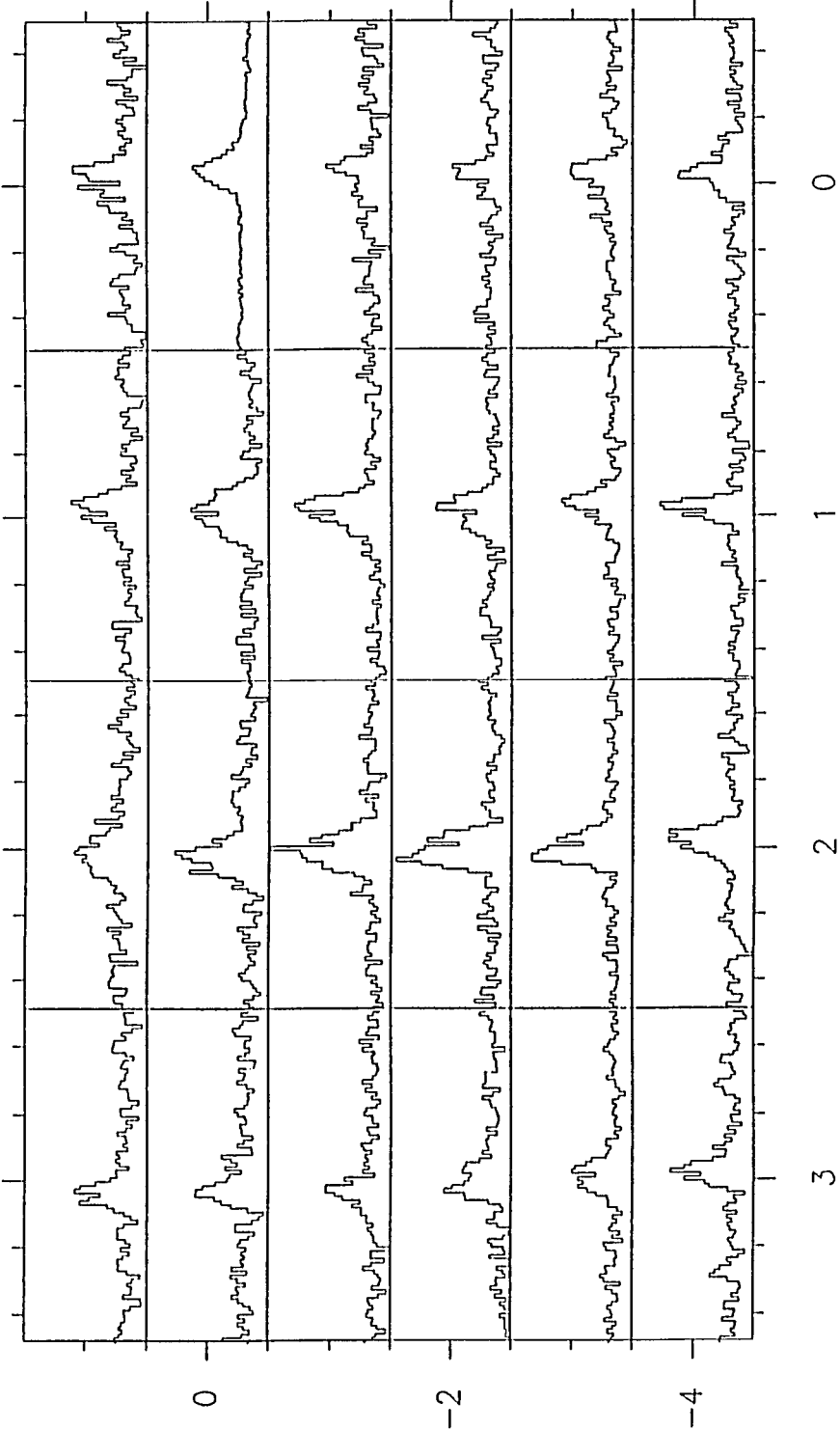


Figure 3.4

Fig. 3.5. C^{34}S $2\rightarrow 1$ spectra (solid) obtained in the SCL are compared with the C^{32}S $2\rightarrow 1$ spectra (dashed) at these positions. Outflow C spectra were obtained at $\alpha_{1950} = 6^{\text{h}}38^{\text{m}}25^{\text{s}}$ and $\delta_{1950} = 9^{\circ}32'29''$. Outflow B spectra were obtained at $\alpha_{1950} = 6^{\text{h}}38^{\text{m}}37^{\text{s}}$ and $\delta_{1950} = 9^{\circ}28'28''$. IRAS 12 spectra were obtained at $\alpha_{1950} = 6^{\text{h}}38^{\text{m}}16^{\text{s}}$ and $\delta_{1950} = 9^{\circ}38'23''$. Outflow D spectra were obtained at an offset of $(1', -1')$ from IRAS 12.

Fig. 3.6. C^{34}S $2\rightarrow 1$ spectra (solid) obtained at the position $1'$ north of IRAS 4 and at the position of IRAS 5 are compared with the C^{32}S $2\rightarrow 1$ spectra (dashed) at these positions. The position of IRAS 4 is $\alpha_{1950} = 6^{\text{h}}38^{\text{m}}38^{\text{s}}$ and $\delta_{1950} = 9^{\circ}24'15''$. The position of IRAS 5 is $\alpha_{1950} = 6^{\text{h}}38^{\text{m}}25^{\text{s}}$ and $\delta_{1950} = 9^{\circ}27'30''$.

Fig. 3.7. C^{34}S $2\rightarrow 1$ spectra (solid) obtained in the NCL are compared with the C^{32}S $2\rightarrow 1$ spectra (dashed) at these positions. Outflow H spectra were obtained at the position $\alpha_{1950} = 6^{\text{h}}38^{\text{m}}14^{\text{s}}$ and $\delta_{1950} = 10^{\circ}38'30''$. Outflow O spectra were obtained at the position $\alpha_{1950} = 6^{\text{h}}38^{\text{m}}21^{\text{s}}$ and $\delta_{1950} = 10^{\circ}18'38''$.

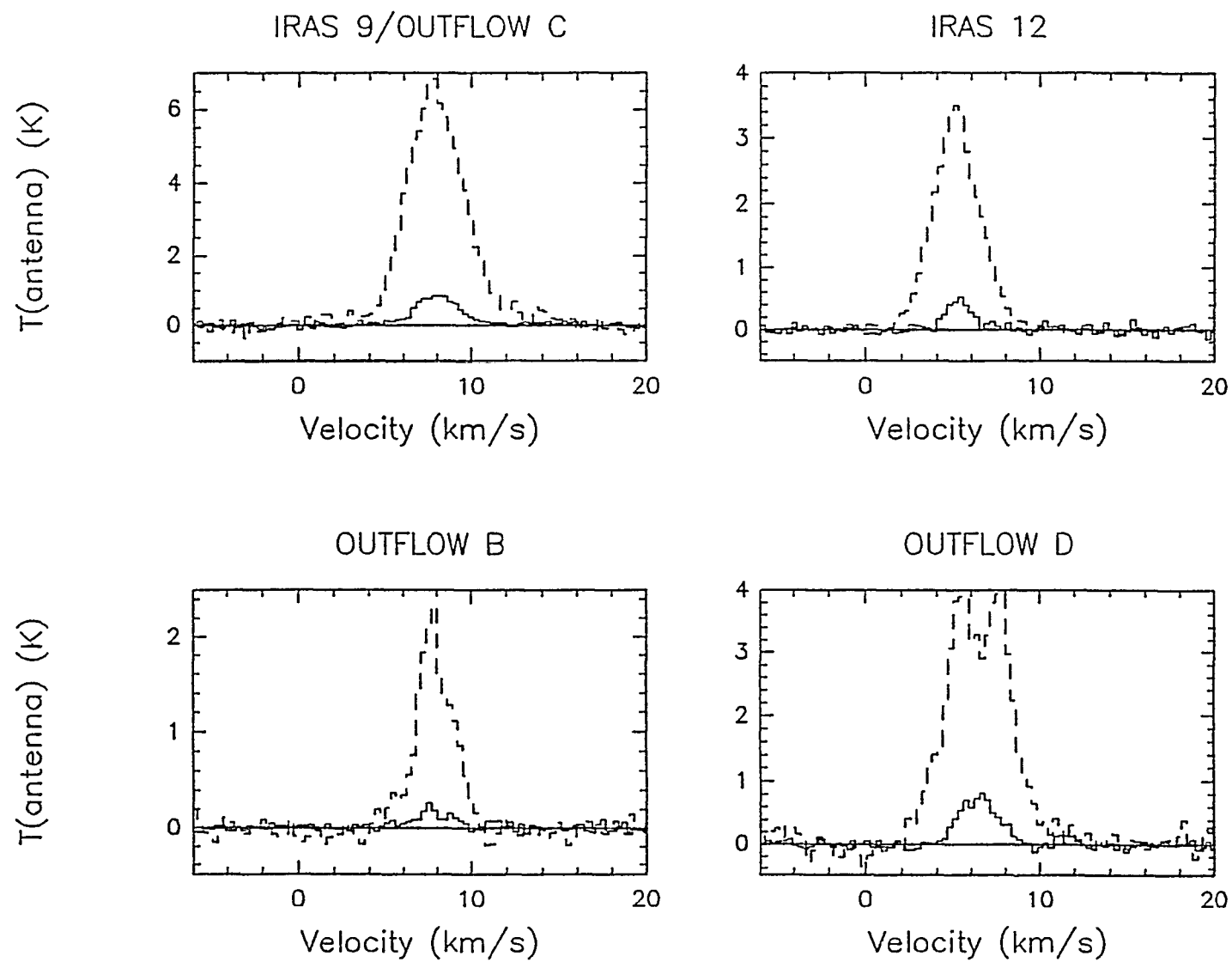


Figure 3.5

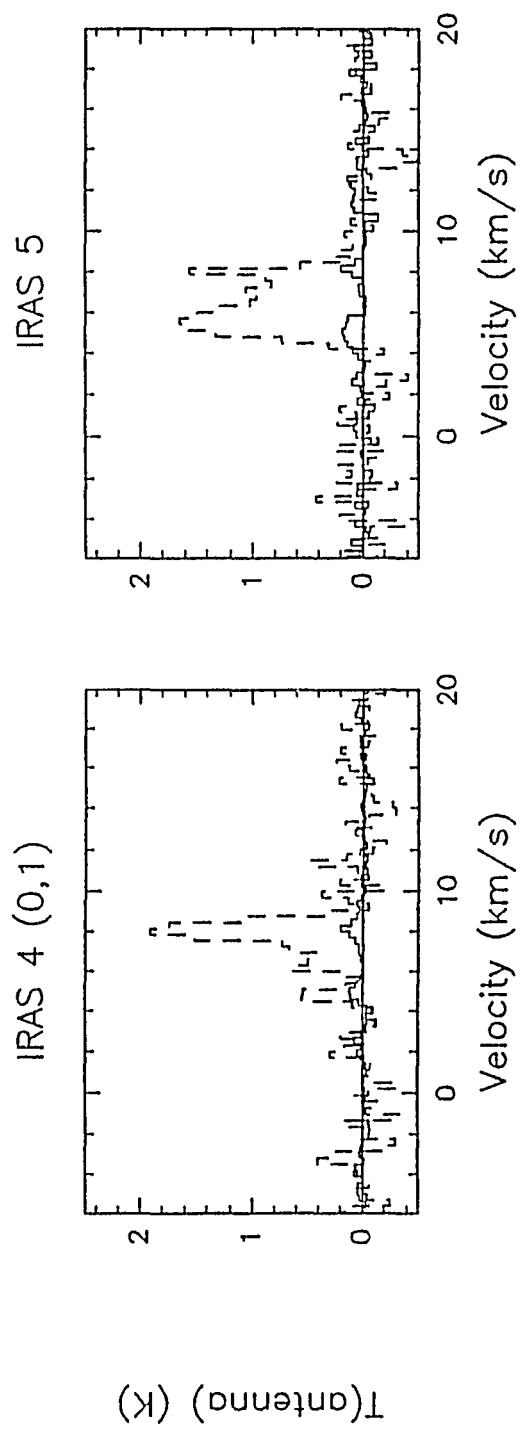


Figure 3.6

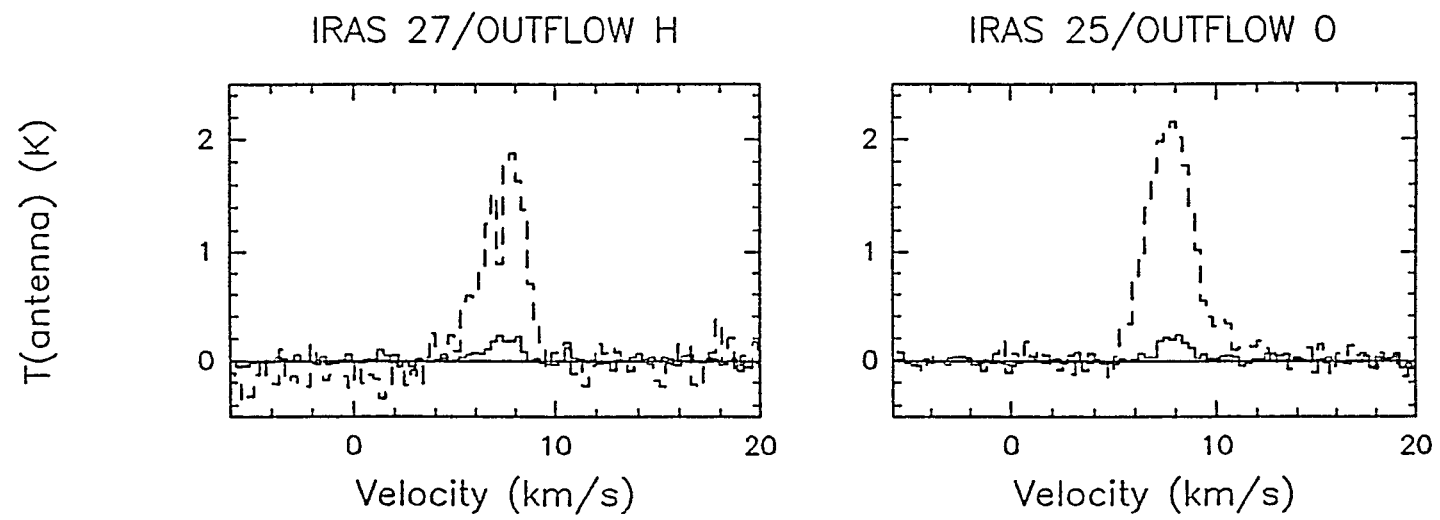


Figure 3.7

3.2.2. Comparison of CS and CO Spectra

The CS and CO observations were made with comparable angular resolutions. Therefore, the CS and CO spectra may be directly compared. In Figures (3.8) to (3.11), we compare CO $1\rightarrow 0$ and CS $2\rightarrow 1$ spectra at positions of peak red and blue wing intensities for CO outflows B, C, D, and H. In addition, Figures (3.8) and (3.9) show blue wing emission in CS for the two outflows (B and C) in which only red wing emission was detected in CO. The CO spectra in these figures were taken from Margulis et al. (1988). Krügel et al. (1987) found evidence for three velocity components in their NH_3 data in the vicinity of Allen's infrared source (Allen 1972). These components are at 6.5, 8.0, and 10.0 km s^{-1} . The CS spectrum for outflow C shows evidence of these three components as well. The CS spectrum for outflow B also gives evidence for three or four components. We will show that much of the the multi-component appearance of the spectra can be accounted for by outflow activity, particularly at the edges of the SCL, where most of the emission is produced by material entrained in the outflow. Enhanced line wing temperatures are consistent with older flows which have swept up a large amount of ambient material.

There are many similarities in the shapes of the CS and CO spectra, despite the fact that CO and CS probe quite different regimes in molecular clouds. The CS spectrum at the position of peak CO red wing integrated intensity in outflow B shows evidence of both red- and blueshifted outflow material. The CO spectrum shows evidence for a blue wing only at relatively low velocities, with an intensity about half of the

line peak. This was not considered to be outflow by Margulis. The CO and CS spectra at Allen's infrared source (IRS) associated with outflow C also appear similar. The CO and CS blue and red wing spectra for outflow D are remarkably similar. In particular, the red wing is seen as a plateau feature in both, with evidence for blueshifted outflow gas present even in the spectra taken at the red wing peak integrated intensity. A striking similarity is also seen in the CO and CS low intensity, high velocity red wing emission in outflow H. The CS line temperatures are fairly low at the positions of the CO outflow B red wing maximum and outflow D red wing maximum since these positions are located at edges of the CS SCL. The velocity of the ambient cloud in the CO spectrum for outflow B is approximately 6 km s^{-1} , however, the peak velocity for the CS spectrum is approximately 8 km s^{-1} . This may indicate that the CS transition is almost exclusively tracing the redshifted outflow gas at this position.

The similarities between the CS and CO spectra imply the CS $2 \rightarrow 1$ transition is probing both the ambient cloud and the outflows. Particularly, we see evidence for outflow at velocities that lie within the line cores of the CO spectra.

Fig. 3.8. Comparison of the CO and CS spectra in the vicinity of outflow B. The red wing spectra were taken at $\alpha_{1950} = 6^h38^m37^s$ and $\delta_{1950} = 9^\circ27'27''$, the position of maximum CO red wing integrated intensity. The CS blue wing spectrum was taken at $\alpha_{1950} = 6^h38^m28^s$ and $\delta_{1950} = 9^\circ27'23''$, the position of maximum CS blue wing integrated intensity.

Fig. 3.9. Comparison of the CO and CS spectra in the vicinity of outflow C. The red wing spectra were taken at $\alpha_{1950} = 6^h38^m25^s$ and $\delta_{1950} = 9^\circ32'27''$, the position of Allen's IRS. The CS blue wing spectrum was taken at $\alpha_{1950} = 6^h38^m32^s$ and $\delta_{1950} = 9^\circ32'23''$, the position of maximum CS blue wing integrated intensity.

Fig. 3.10. Comparison of the CO and CS spectra in the vicinity of outflow D. (a) Spectra taken at $\alpha_{1950} = 6^h38^m25^s$ and $\delta_{1950} = 9^\circ37'27''$, the position of maximum CO blue wing integrated intensity. (b) Spectra taken at $\alpha_{1950} = 6^h38^m05^s$ and $\delta_{1950} = 9^\circ35'27''$, the position of maximum CO red wing integrated intensity.

Fig. 3.11. Comparison of the CO and CS spectra in the vicinity of outflow H. (a) Spectra taken at $\alpha_{1950} = 6^h38^m17^s$ and $\delta_{1950} = 10^\circ40'27''$, the position of maximum CO blue wing integrated intensity. (b) Spectra taken at $\alpha_{1950} = 6^h38^m17^s$ and $\delta_{1950} = 10^\circ39'26''$, the position of maximum CO red wing integrated intensity.

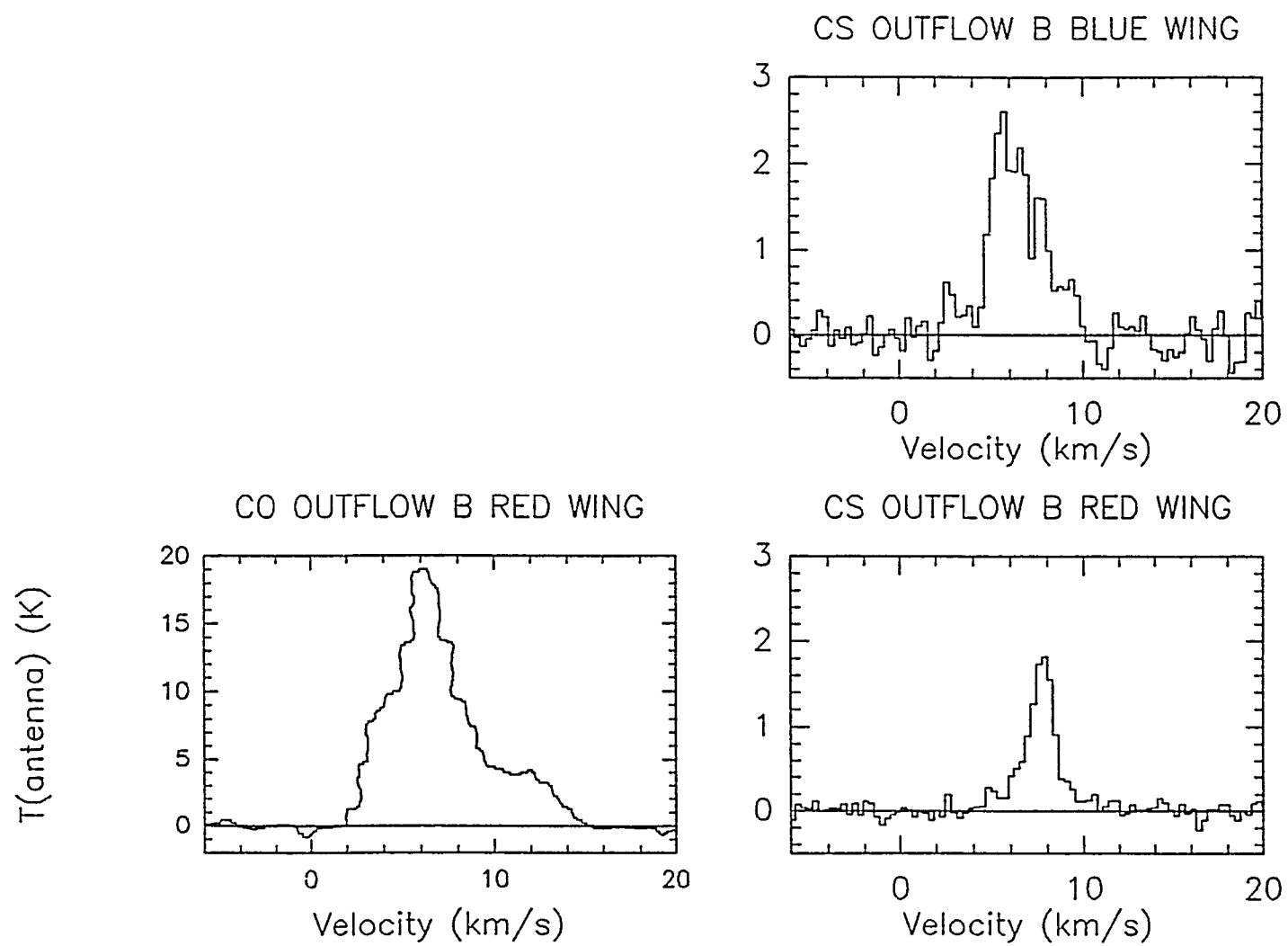


Figure 3.8

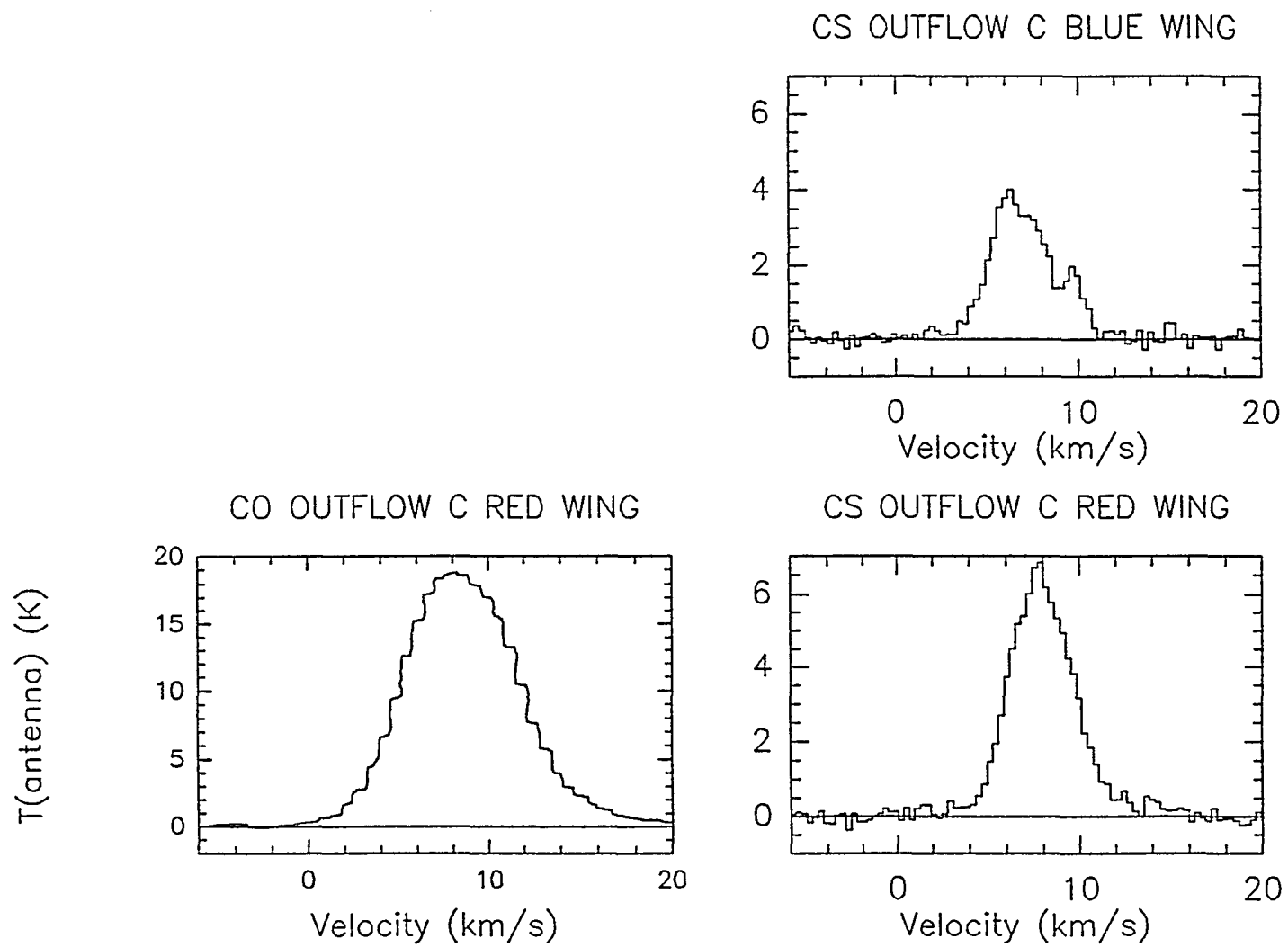


Figure 3.9

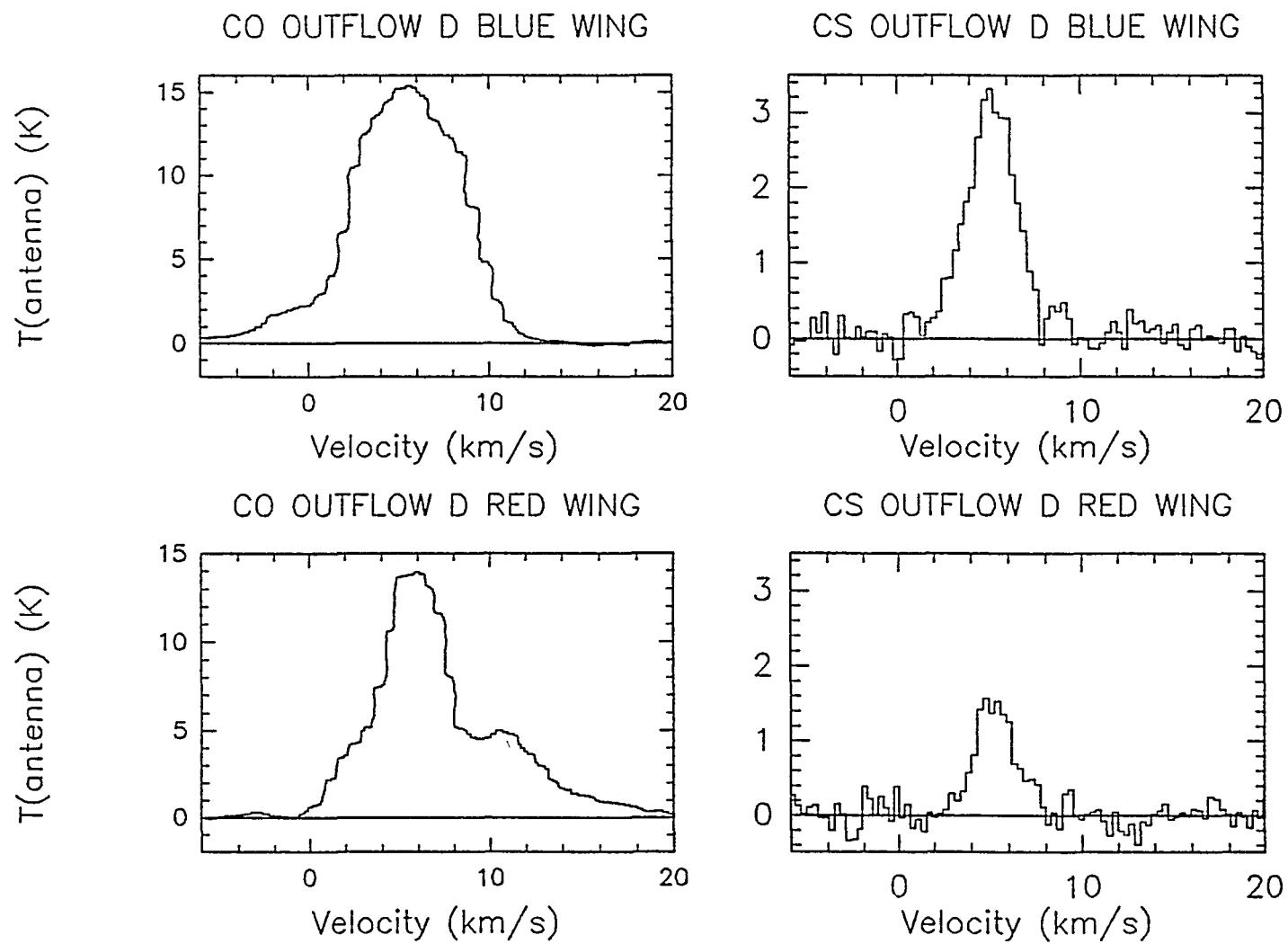


Figure 3.10

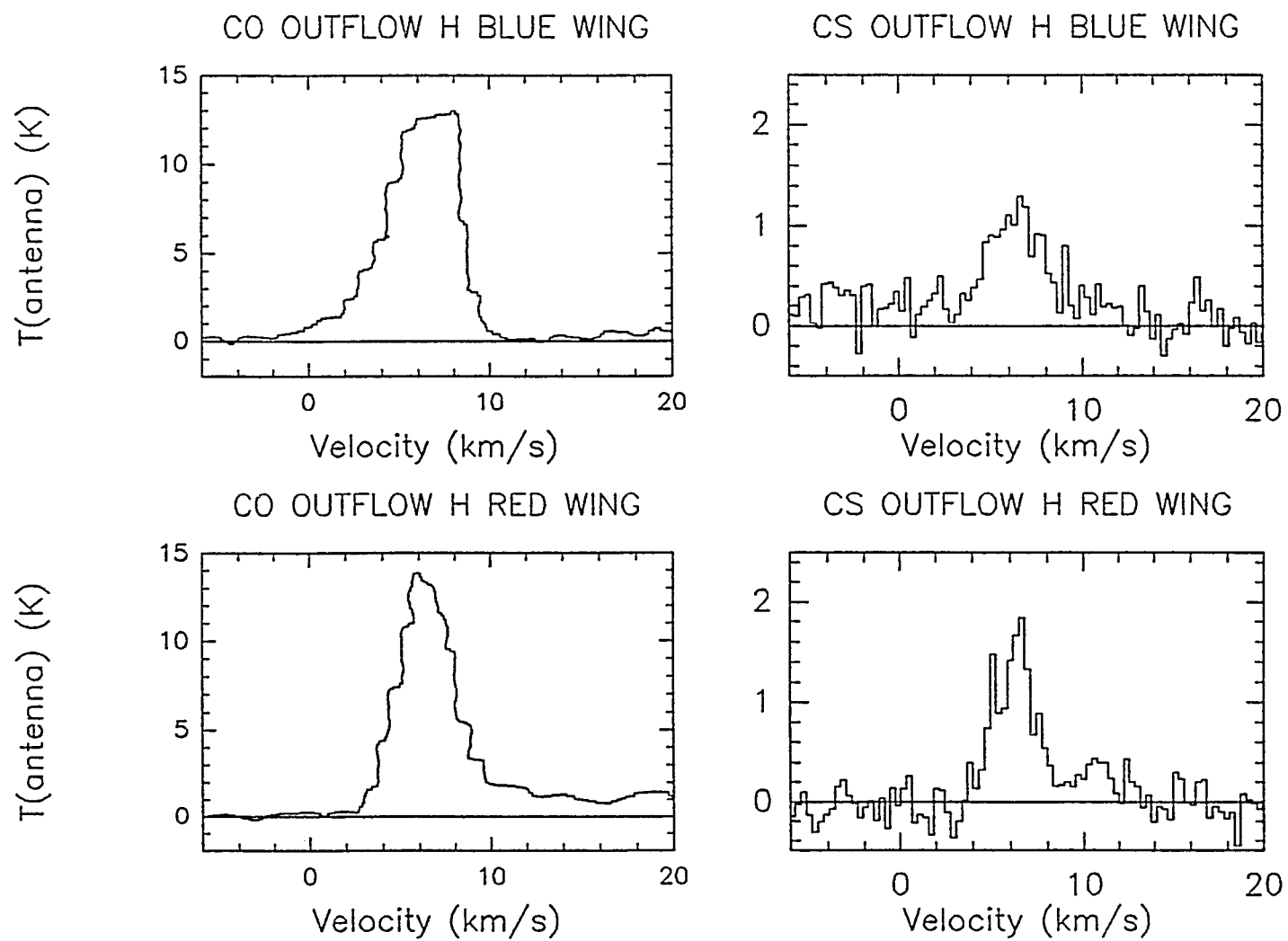


Figure 3.11

3.2.3. CS Distribution

The CS gas is distributed in two major condensations which encompass 60% of the outflows discovered in this cloud. Integrated intensity maps of these two condensations, referred to as the South Cloud (SCL) and North Cloud (NCL) are presented in Figure (3.12). These two condensations encompass 5 CO outflows (B, C, D, O, and H). Discounting O, which was not mapped in CO, the remaining four outflows are the most massive flows in Mon OB1. The CS $J=5\rightarrow4$ transition was also detected in the vicinity of outflows C, D, O, and H, although the latter two were single detections. There are four possible reasons for the detection of the higher CS transition in these regions:

- (1) We are seeing the dense cores in which the IRAS sources associated with these outflows have formed.
- (2) Gas temperatures are enhanced in these regions due to collisions with warm dust, so we are seeing what is at least partially a temperature effect.
- (3) Densities are enhanced because gas has been swept up into dense shells by the outflows.
- (4) CS is enhanced in these regions due to the enhanced production of sulfur containing molecules in shocked regions (Thronson and Lada, 1984).
- (5) Temperatures are enhanced due to interaction of the outflows with the ambient gas.

As there were null CS detections at the 150 mK level at a number of equally bright IRAS sources unassociated with CO outflow, explanations (3), (4), and (5) seem to be more reasonable explanations than (1) and

(2). In other words, the observed intensity of the CS gas seems to have more to do with effects produced by outflows than with the luminosities of the IRAS sources or the dust temperatures in the vicinity of these sources. These possibilities will be discussed in detail in Chapter 4.

Figure (3.13) compares the CS $J=2\rightarrow1$, $J=5\rightarrow4$, and $J=7\rightarrow6$ integrated intensity distributions in the SCL. Figure (3.14) compares the 1.3 mm continuum map of Walker et al. (1990), and the CS $J=5\rightarrow4$ and CS $J=7\rightarrow6$ peak temperature distributions in the SCL. The CS $5\rightarrow4$ emission is concentrated in two regions approximately $2'$ in diameter near IRAS 9 and IRAS 12, while the CS $7\rightarrow6$ emission is detectable only in the immediate vicinity of IRAS 9, and was not detected to the 230 mK level about IRAS 12. There is a striking difference in the morphology of the $5\rightarrow4$ integrated intensity and peak temperature distributions about the NW component. The elongated appearance of the integrated intensity contours to the W and NE reflects the line broadening by outflow D. The inner contours of the 1.3 mm continuum map reflect the structure of the $7\rightarrow6$ emission about IRAS 9 well.

Fig. 3.12. (a) CS 2→1 integrated intensity map for the SCL. The (0,0) position is $\alpha_{1950} = 6^h38^m16^s$ and $\delta_{1950} = 9^\circ38'23''$. Contour levels start at 2 K km s⁻¹ and increase in steps of 2 K km s⁻¹ to 28 K km s⁻¹. (b) CS 2→1 integrated intensity map for the NCL. The (0,0) position is $\alpha_{1950} = 6^h38^m10^s$ and $\delta_{1950} = 10^\circ39'30''$. Contour levels start at 0.5 K km s⁻¹ and increase in steps of 0.5 K km s⁻¹ to 5.5 K km s⁻¹. IRAS sources (+) are indicated. Axes units are arcminute offsets.

Fig. 3.13. The distribution of CS 2→1, CS 5→4, and CS 7→6 gas in the SCL. (a) CS 2→1 integrated intensity maps for the vicinities of IRAS 12 (upper) and IRAS 9 (lower). The peak contours for these maps are 16 K km s⁻¹ (upper) and 26 K km s⁻¹ (lower) and decrease in steps of 2 K km s⁻¹. (b) CS 5→4 integrated intensity in the vicinity of the NW component, about IRAS 12. Contours start at 0.5 K km s⁻¹ and increase in steps of 0.5 K km s⁻¹ to 6 K km s⁻¹. (c) CS 5→4 integrated intensity in the vicinity of Allen's star, IRAS 9. Contours start at 2 K km s⁻¹ and increase in steps of 2 K km s⁻¹ to 24 K km s⁻¹. (d) CS 7→6 integrated intensity in the vicinity of IRAS 9. Contours start at 2 K km s⁻¹ and increase in steps of 2 K km s⁻¹ to 18 K km s⁻¹. The beamwidths are 64'', 29'', 26'', and 21'', respectively. IRAS sources (+) are indicated. Axes units are arcminute offsets.

Fig. 3.14. Comparison of dust distribution and peak temperature distribution of CS cores. (a) 1.3 mm continuum map reproduced from Walker et al. (1990). Contours begin at 0.8 Jansky and increase in steps of 0.4 Jansky to 2.8 Janskys. (b) Peak temperature distribution of CS 5→4 about IRAS 12. Contours begin at 0.5 K and increase in steps of 0.5 K to 2.0 K. (c) Peak temperature distribution of CS 5→4 about IRAS 9. Contours begin at 1 K and increase in steps of 1 K to 6 K. (d) Peak temperature distribution of CS 7→6 about IRAS 9. Contours begin at 1 K and increase in steps of 1 K to 6 K. IRAS sources (+) are indicated. Axes units are arcminute offsets. Beamwidths are 30'', 29'', 26'', and 21'', respectively.

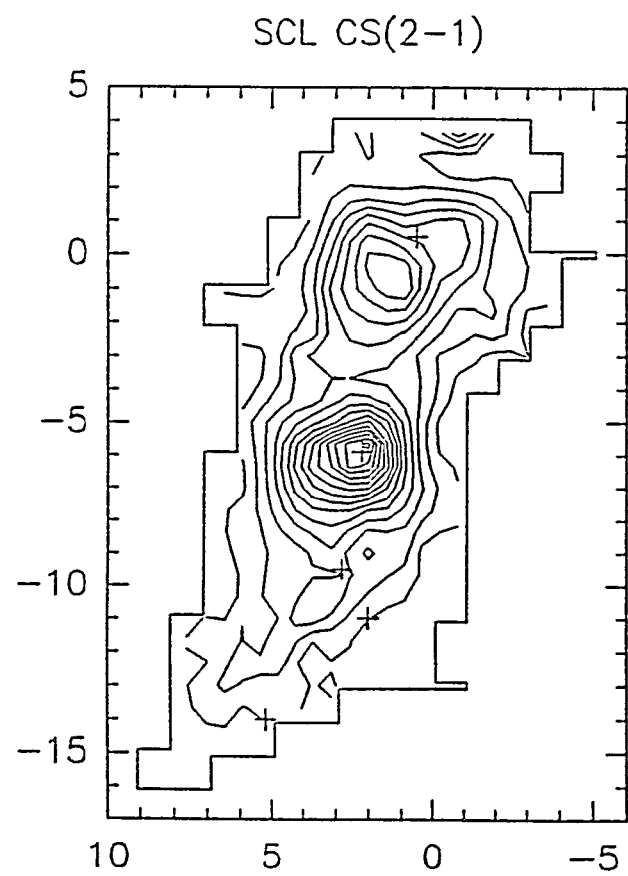


Figure 3.12a

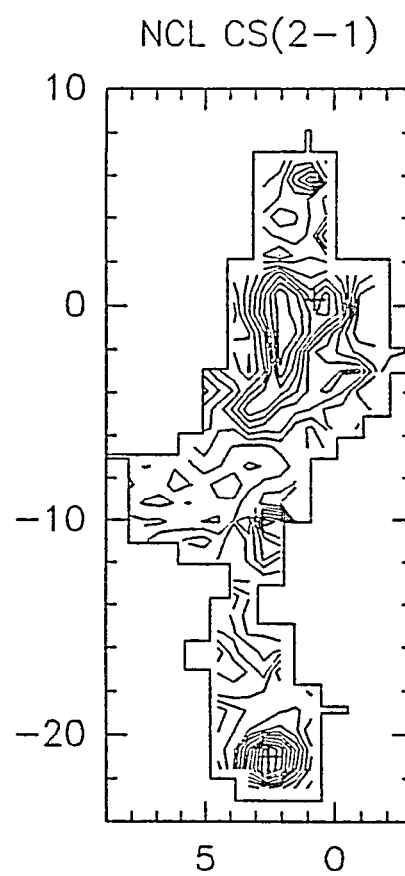


Figure 3.12b

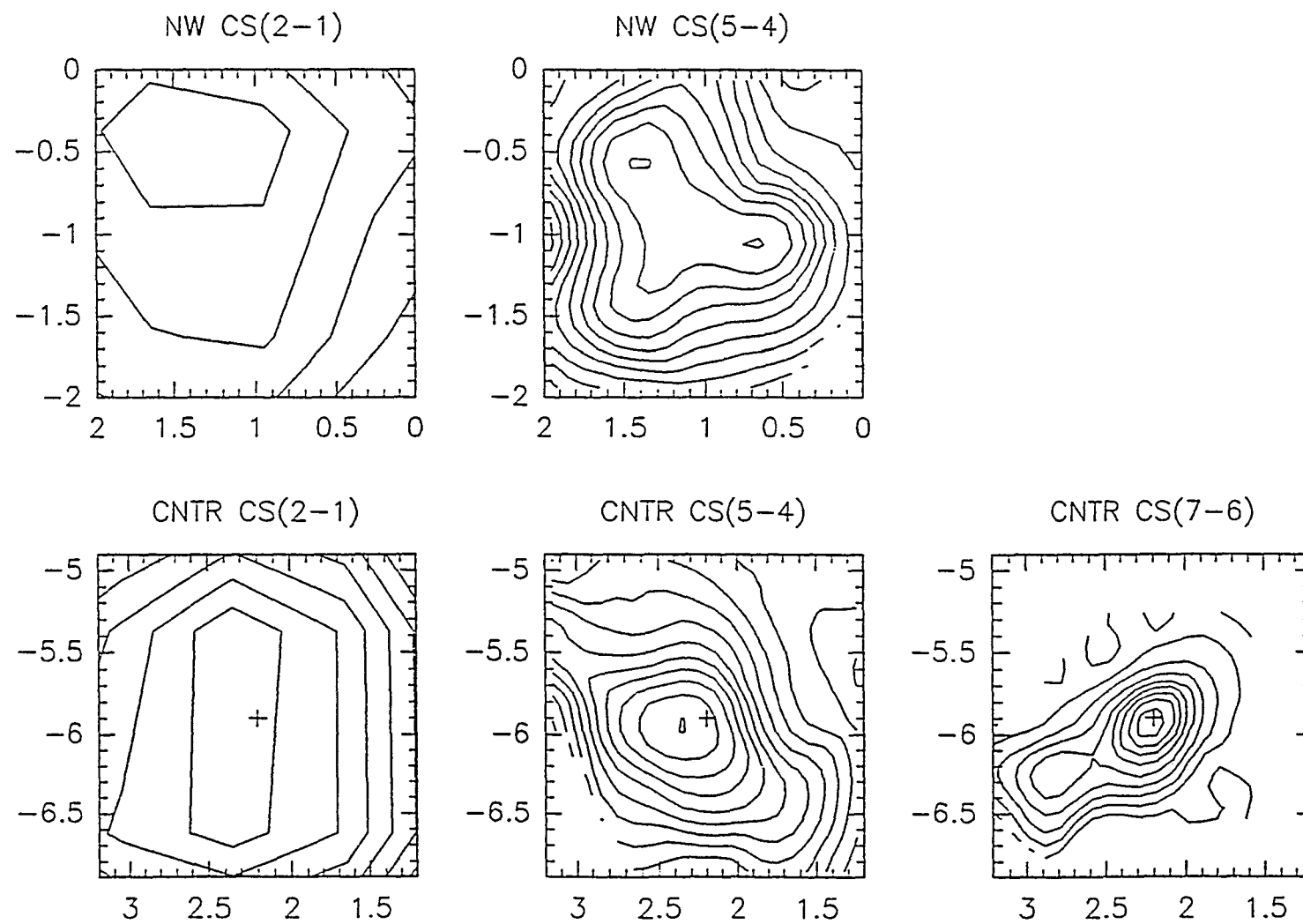


Figure 3.13

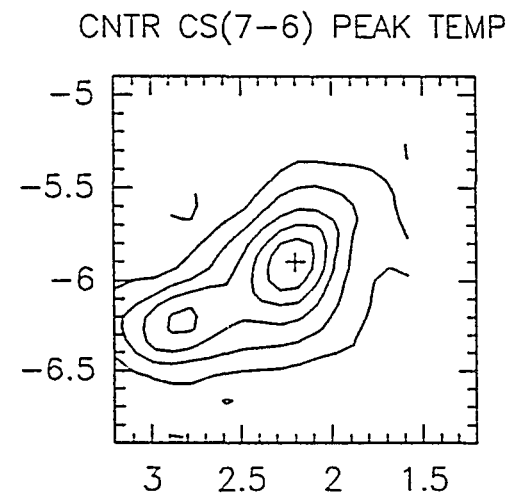
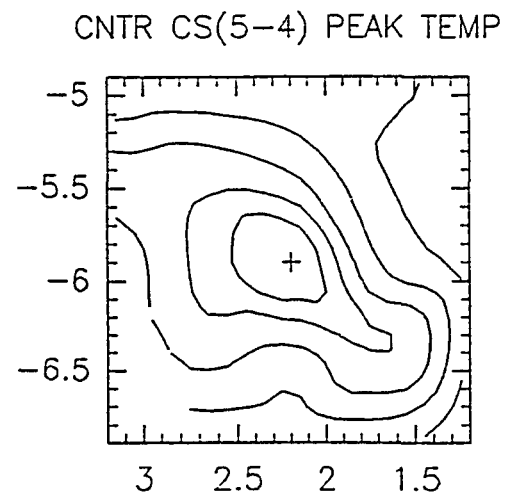
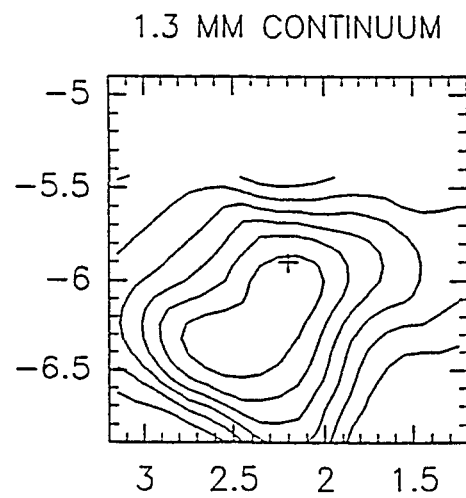
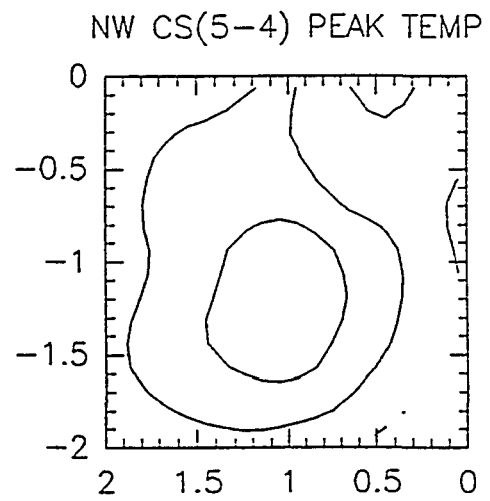


Figure 3.14

3.2.4. Comparison of CS, CO, and NH₃ Distribution

The two major peaks in the large-scale CO distribution lie in the regions of the extended CS emission SCL and NCL.

The distribution of CS in the SCL is very similar in morphology and extent to the NH₃ distribution (Krügel *et al.* 1987), although the CS 2→1 emission is more extended to the southeast. There are two peaks in the CS distribution. The southeastern peak coincides with the position of IRAS 9 (Allen's IRS), while the northwestern peak lies approximately 1 arcminute south and 1 arcminute east of IRAS 12. This northwest peak, in fact, coincides with the center of the outflow associated with the northwest IRS. Assuming IRAS 12 is, in fact, the driving source of this outflow, the discrepancy cannot be explained by positional inaccuracies alone. Although the size of IRAS 12 at 25 μ is 0.9 arcminute (Margulis 1987), and the beamwidth of the 12 m telescope is about 1 arcminute at the frequencies of the CS J=2→1 and CO J=1→0 transitions, it should be noted that *all* of the molecular transitions peak southward of IRAS 12. However, the 170 μ m peak (Schwartz *et al.* 1985) *does* coincide with the IRAS position (Figure 3.15). This suggests the dust and gas components have a different distribution. In Section (3.2.3) we suggested that the observed intensity of the CS gas was more directly related to the presence of outflow than the presence of a luminous YSO. If the line temperature enhancements are *not* directly due to gas-dust collisions, we must question whether densities, temperatures or abundances are more affected by the outflows. Although it has been shown that the production of sulfur containing molecules

is enhanced in shocked regions, this alone cannot explain the fact that apparently all of the molecular transitions peak southward of the dust peak. IRAS 12 is apparently located at the northern end of this cloud core and is driving a very large, massive outflow. The major axis of the CO outflow is approximately $10'$, or 2.3 pc, in extent. This outflow is sweeping up more molecular gas to the south than to the north, and may in fact be creating a molecular “ridge” towards the southeast where densities and temperatures are greater, accounting for the increased molecular emission in this region. Walker (1988) noted a similar effect in the outflow region around 1629a, where the gas temperature peaks up on the outflow lobes rather than the IRS. Since the dust distribution traces both temperature and column density, and the CS and NH_3 transitions more effectively trace column density and density enhancements, it is reasonable that the outflow may have swept up a denser ridge of material towards the SE, especially since the spatial distribution of the CO flow indicates it is breaking out of the CS core in the north.

Krügel found the mass of the two NH_3 components to be approximately $1000 M_\odot$; the masses of the condensations about IRAS 9 and IRAS 12 are about $500 M_\odot$ each. This agrees to about a factor of 2 with the mass calculated for the CS using the LTE approach. For a T_{ex} of between 10 and 25, and a filling factor between 0.3 and 1.0, the CS mass of the SCL is roughly $1800 - 2500 M_\odot$. We note, however, that the region we mapped in CS is extended several arcminutes to the southeast of the region detected and mapped by Krügel in NH_3 .

Comparing Krügel’s NH_3 integrated intensity map of the region to

the total integrated intensity map of the CS gas in the SCL, and to the channel maps of this region, the E - W and N - S extensions of the NH_3 map in the vicinity of IRAS 12 may be clearly identified with CS peaks or extensions at the ambient cloud velocity, $\sim 5.5 \text{ km s}^{-1}$. This provides a good indication that the two molecules are indeed tracing the same ambient gas in this region.

There are also striking similarities between my CS $J=2 \rightarrow 1$ map, Krügel's $\text{NH}_3(1,1)$ map, and the CS $J=3 \rightarrow 2$ of Schwartz et al. (1985) (Figure 3.15). It is interesting to note that the NE - SW elongation of the component which includes Allen's IRS is seen in both the CS $3 \rightarrow 2$ integrated intensity map (Figure 3.15b) and the CS $5 \rightarrow 4$ integrated intensity and peak temperature maps (Figures 3.13c and 3.14c). It is possible this extension is due to interaction of outflow C with the core gas in this region. Its absence in our CS $2 \rightarrow 1$ map may be due to beam dilution. The CS $5 \rightarrow 4$ map about Allen's IRS also shows a slight NW - SE elongation. The CS $7 \rightarrow 6$ integrated intensity and peak temperature maps (Figures 3.13d and 3.14d) are elongated in a NW - SE direction with an axis ratio of about 3:1. At this resolution and density, we are seeing the true ambient density structure, and possibly the collimating structure for the outflow. The CS $7 \rightarrow 6$ flattened structure is aligned approximately perpendicular to the direction of the CS outflow. I will later investigate the possibility that this structure is indeed responsible for collimating the outflow. It should be noted that the diameter of this structure is approximately 0.3 pc, and so is over an order of magnitude larger than a true circumstellar disk.

The CS $5 \rightarrow 4$ gas about IRAS 12 also shows evidence of tracing

both ambient gas and material participating in the outflow. The integrated intensity and peak temperature maps (Figures 3.13b and 3.14b). show considerably different structure. The integrated intensity map shows an extension towards the SE which follows the general extension of the SCL, while the extensions to the west and to the northeast follow the general morphology of the outflow. The peak temperature distribution is much more isotropic and peaks to the SE of the (0,0) position adopted for IRAS 12. Since integrated intensities reflect the broad lines associated with outflow, the morphology of the $5 \rightarrow 4$ gas in this region reflects that of outflow D.

The distribution of the CS in the NCL is more complex (Figure 3.12b), and as we will show in Section (3.3), changes dramatically over 1 km s^{-1} velocity intervals. There are four peaks in the overall distribution. One peak is offset approximately 1 arcminute to the southeast of IRAS 27, the source associated with outflow H. This offset in position might be due to pointing error, however Margulis also noted that the center of the CO outflow was offset to the east of the position of IRAS 27. The outflow axis is elongated N - S, roughly parallel to the N - S elongation of the NCL clump. There is a secondary CS emission peak that lies less than one arcminute west of IRAS 27. The southern peak in the NCL is associated with IRAS 25 and is well-localized. The peak is offset about 1 arcminute northeast of IRAS 25. However, in this case the offset is most likely the result of pointing error. There is a CO outflow associated with IRAS 25. This outflow is observed in broad, asymmetric line wings in the CS data, but only over the well-localized region of emission. A fourth peak several arcminutes north of IRAS 27 is not coincident with any known IRAS

source. The mass of the NCL is significantly less than that of the SCL. For T_{ex} between 10 and 25, and a filling factor between 0.2 and 1.0, the mass derived from the CS 2→1 data is found to range from about 500 - 900 M_{\odot} . The mass of the clump associated with the two peaks near IRAS 27 is approximately 200 M_{\odot} . This clump is roughly cylindrical in shape and encompasses the region displayed in the spectra map about outflow H (Figure 3.4).

Fig. 3.15. Comparison of the distribution of CS 2→1, CS 3→2, 170 μm continuum, and $\text{NH}_3(1,1)$ emission in the SCL. (a) CS 2→1 integrated intensity. Contours start at 2 K km s^{-1} and increase in steps of 2 K km s^{-1} to 28 K km s^{-1} . (b) CS 3→2 integrated intensity in the SCL (solid contours). Contours start at 2 K km s^{-1} and increase in steps of 2 K km s^{-1} to 10 K km s^{-1} . Dust (170 μm) map (dashed contours). Contours are 0.025, 0.05, 0.1, 0.2, 0.4×1600 Jy. This figure was taken from Schwartz et al. (1985). (c) $\text{NH}_3(1,1)$ integrated intensity of the main group of hyperfine components in the SCL. Contours start at 2 K km s^{-1} and increase in steps of 2 K km s^{-1} to 14 K km s^{-1} . This figure was taken from Krügel et al. (1987). IRAS sources (+) are indicated. Axes units are arcminute offsets.

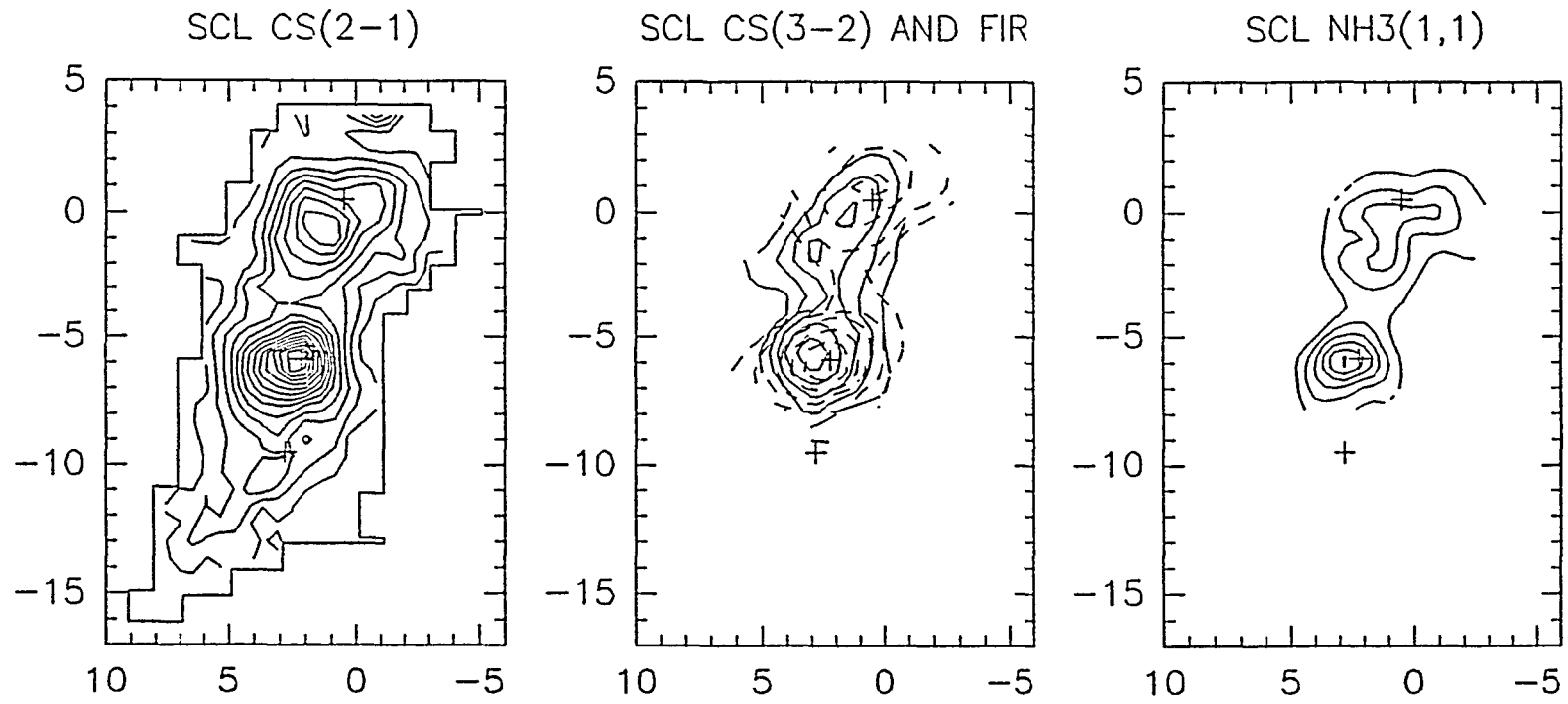


Figure 3.15

3.2.5. Comparison of CS and CO Wing Maps

In this section, I will examine the relationship of the dense gas traced by the CS observations to the CO outflows. CS was detected in the vicinity of 5 of Margulis' 9 outflows, as well as around the CO outflow associated with IRAS 25, which has recently been associated with two groups of Herbig-Haro objects (Walsh *et al.* 1992). A CS outflow is identifiable in the 3 CO outflows found in the SCL. Figure (3.16) shows our CS $J=2\rightarrow 1$ wing maps and the CO $J=1\rightarrow 0$ wing maps of Margulis for the SCL outflows. Again, the CO and CS wing maps may be directly compared due to the comparable beam sizes. The major axes of the CS outflows in the SCL are perpendicular to the general extension of the SCL and Mon OB1 cloud. This is consistent with a model in which the driving sources are embedded in circumstellar disks which have collapsed along the same orientation.

The area of detected CS emission in the SCL encompasses the outflows B, C, and D identified in CO by Margulis. The outflow D is spatially somewhat larger than the detected CS component in the northern condensation. Shell structure is evident in the CS outflow associated with the CO outflow D. The CS wing emission brackets the edges of the CO outflow. This CO/CS morphology is consistent with the idea that the CS emission arises from a dense, swept-up shell of gas located at the outer boundary of the outflow. This is precisely where you would expect to find the lowest-velocity gas associated with the outflow. The CO outflow extends beyond the CS condensation, so there is no dense gas to be swept up to

the northeast side of the CO blue lobe of outflow D, nor to the southwest of the red lobe. The shell structure is evident in both the blueshifted and redshifted CS gas. In fact, inspection of the CS channel maps in the Section (3.3.2) will show that little, if any, “ambient” component remains and most of the molecular gas in this condensation has been entrained in the outflow.

Two of the CO outflows in the southern condensation of the SCL were found to have red wings only. However, in CS both redshifted and blueshifted gas is identifiable for outflow C, in the region around IRAS 9, and a blue wing and faint red wing is identified for outflow B. This red wing defines the southeastern boundary of the CO red wing, at the very edge of the region of CS emission. The redshifted CS gas associated with IRAS 9 has approximately the same orientation and size as the CO outflow, and extends a couple of arcminutes southwest of the IRS. The blueshifted CS gas extends nearly due east of IRAS 9 so the two lobes display a bent structure similar to that observed in various other outflows such as Mon R2 (Wolf *et al.* 1990).

The blueshifted CS gas associated with CO outflow B lies slightly southwest and also northeast of IRAS 6. The redshifted gas lies a few arcminutes southeast of IRAS 6. It is possible that the reason the center of the outflow is offset to the south of the position of IRAS 6 is that southward of IRAS 6 the CS gas is tracing outflow only, but to the north, where densities are greater, the outflow is moving at velocities slow enough to be masked by the CS line cores as well as the CO line cores. The CS and C³⁴ 2→1 spectra presented for outflow B in Figure (3.5) indicate that

we are seeing a bipolar outflow in this region. The fact that the redshifted gas lies further from IRAS 6 than the blueshifted gas is consistent with the density decreasing towards the southeast edge of the CS cloud. The southwestern blueshifted peak is also near IRAS 5, so it is possible that line temperatures are enhanced due to the presence of this IRS. It is also possible that IRAS 5, rather than IRAS 6, is the driving source of outflow B. However, the luminosities of IRAS 5 and 6 are $2 L_{\odot}$ and $12 L_{\odot}$, respectively. If IRAS 5 is the driving source, this implies that the mechanical luminosity of the outflow (Tables 3.6 and 5.1) is comparable in magnitude to the luminosity of the driving source, contrary to the trend found by Bally and Lada (1983) for 14 mapped outflow sources which, in general, tend to have mechanical luminosities between 0.2 % and 20 % of the luminosities of the central driving sources. The blueshifted CS gas lies at the boundary of a region of weak, extended high-velocity CO emission. This extended high-velocity CO emission may be the remnants of an old outflow. Since the blueshifted CS emission is so well-localized, it is unlikely that the CS emission is associated with the fossil outflow.

The CS wing maps in the NCL appear to be quite different from those in the SCL. Inclusion of these maps is postponed to Chapter 5 where we discuss the interaction of outflows with the CS cores in more detail. Although outflow H can be identified in CS, the velocity field in this region is quite complicated, and appears at least in part, to be due to the large-scale rotation of an elongated cylindrical structure. This structure will be discussed in the next few sections.

Fig. 3.16. (a) CS 2→1 wing integrated intensity maps for outflows B, C, and D in the SCL. Dotted lines denote blue wing emission and solid lines denote red wing emission. For outflow B, blue wing contours start at 0.5 K km s^{-1} and increase in steps of 0.5 K km s^{-1} to 2.5 K km s^{-1} and red wing contours start at 0.5 K km s^{-1} and increase in steps of 0.5 K km s^{-1} to 1.0 K km s^{-1} . The integrated intensities were calculated over a range of 4.0 to 6.0 km s^{-1} for the blue wing emission, and from 10.0 to 15.0 km s^{-1} for the red wing emission. For outflow C, blue wing contours start at 0.5 K km s^{-1} and increase in steps of 0.5 K km s^{-1} to 4.5 K km s^{-1} . The integrated intensities were calculated over a range from 3.0 to 6.0 km s^{-1} for the blue wing emission, and from 10.5 to 15.0 km s^{-1} for the red wing emission. For outflow D, blue wing contours start at 0.5 K km s^{-1} and increase in steps of 0.5 K km s^{-1} to 4.5 K km s^{-1} and red wing contours start at 1 K km s^{-1} and increase in steps of 1 K km s^{-1} to 8 K km s^{-1} . The integrated intensities were calculated over a range from 2.0 to 4.5 km s^{-1} for the blue wing emission, and from 6.5 to 10.0 km s^{-1} for the red wing emission. (b) CO 1→0 wing integrated intensity maps for outflows B, C, and D in the SCL. For outflow B, contour levels start at 2.0 K km s^{-1} and increase in steps of 1.0 K km s^{-1} . The integrated intensities were calculated over a range from 10 to 16 km s^{-1} . For outflow C, contour levels start at 2.0 K km s^{-1} and increase in steps of 2.0 K km s^{-1} . The integrated intensities were calculated over a range from 12 to 22 km s^{-1} . For outflow D, contour levels start at 2.0 K km s^{-1} and increase in steps of 1.0 K km s^{-1} for blue and red wing emission. The integrated intensities were calculated over a range from -10 to 2 km s^{-1} for the blue wing emission, and from 11 to 21 km s^{-1} for the red wing emission. IRAS sources (+) are indicated and outflows are labelled. Axes units are arcminute offsets.

SCL CS OUTFLOWS B, C, AND D

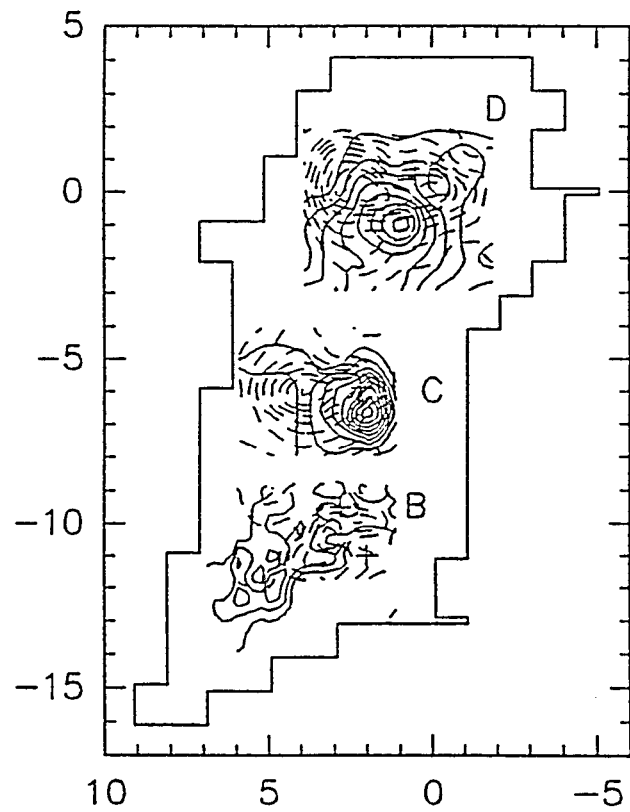


Figure 3.16a

SCL CO OUTFLOWS B, C, AND D

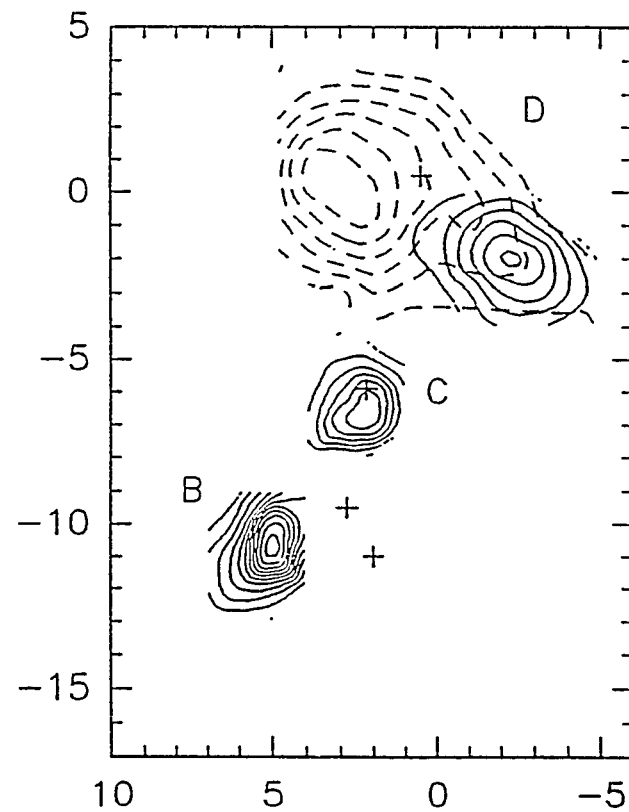


Figure 3.16b

3.3. CS Velocity Structure

As will be seen in the following sections, the velocity structure of the CS emission in the SCL indicates a large quantity of the dense gas in this region is participating in outflow activity.

The CS velocity structure in the NCL presents a somewhat different picture. Although there is some evidence for CS outflow in the vicinity of CO outflow H and the CO outflow associated with IRAS 25, the situation is far from clear. We have included the CO map of outflow H in Chapter 5 where we discuss the interaction of outflow with the ambient cloud. The reader is referred to Figure (5.3) for the discussion of the CS velocity structure in the NCL during the next couple of sections. There are several different velocity components in the region of H. There is, however, a noticeable overall velocity shift from east to west as evidenced by the shift in the asymmetric double-peaked CS line profiles (Figure 3.4). The most distinctive feature of this apparent east-to-west rotation is its elongation from north-to-south. As will be seen in the channel and velocity centroid maps of this region, there seems to be a fairly smooth velocity gradient on the blueshifted side towards the east. This velocity gradient could indicate the presence of rotation. However, several spatial components on the redshifted side make the actual sense of rotation, if this is what we are actually seeing, difficult to disentangle from other effects. Nevertheless, a comparison of the spectra with the position-velocity, channel, and velocity centroid maps discussed in Sections (3.3.1), (3.3.2), and (3.5.1) indicates that we are seeing a rotating cylindrical structure which encompasses the

region of CO outflow H. In the region of IRAS 25, the CS emission is well-peaked, with no strong evidence for bipolarity.

3.3.1. LV Maps

In this section, I will discuss what can be inferred about the CS velocity structure from position-velocity maps made through RA and Dec in the SCL and NCL. Figures (3.17) to (3.20) are position-velocity maps in RA and Dec for the SCL and NCL, respectively. The SCL strip maps in RA with positional offsets in Dec of $-7'$ and $-6'$ show the extended, redshifted, high-velocity CS gas of outflow C. There is also indication of blueshifted gas extended eastward in RA, though to lower velocities. This blueshifted gas is seen as well in the SCL Dec strip maps at RA offsets $2'$ to $4'$ (note the blueward shift in velocity of the peak emission from $2'$ to $4'$). Faint blueshifted emission associated with outflow B is seen at about Dec = $-11'$ in the maps at RA offsets $1'$ to $5'$ to a velocity of about 5 km s^{-1} . The peak which appears at a velocity of $7.5 - 8 \text{ km s}^{-1}$ at RA $4'$ and $5'$ is associated with IRAS 6. At RA $5'$, the contours extending southward to redder velocities is probably part of the faint red wing emission associated with outflow B. IRAS 6 and the blueshifted outflow gas to the southeast are also evident in the SCL RA strip map through Dec offset $-10'$. Here, IRAS 6 and the blueshifted gas show up as separate peaks at RA = $4'$ and $3'$, respectively.

To the north, outflow D is seen quite well in these maps. The center of this outflow is roughly at offsets $(1', -1')$, and the blue- and

redshifted gas are apparent in the RA strip map at Dec = $-1'$, and the Dec strip map at RA = $1'$. The blueshifted gas is evident in the Dec maps at RA = $1'$, $2'$, and $3'$.

The overall picture is a bit confused in the SCL due to the presence of multiple velocity components within the clump associated with IRAS 9 (Krügel *et al.* 1987), and, possibly, a large-scale velocity gradient reaching from the southern clump containing IRAS 9 to the northern clump containing IRAS 12 (Schwartz *et al.* 1985). There does appear to be a fairly smooth transition in velocity from IRAS 9 to 12, indicative of rotation of the two IRSs about a common center of mass (note the gradual shift in the peak core emission in the SCL RA maps from Dec = $-6'$ to Dec = $0'$). This is not implausible as the virial mass of the SCL for an average linewidth of 2.5 km s^{-1} , a rotational velocity of 1.25 km s^{-1} , and an r^{-2} density law, is approximately $3,500 M_{\odot}$. This is within a factor of two of the LTE mass which we calculate for the SCL in Section (3.4.1). However, there is only a faint bridge of emission which connects the two cloud clumps, so rotation of this structure is very questionable. Also, since a significant fraction of this cloud is participating in outflow activity, the virial theorem is probably invalid here. Another possibility is that the two clumps are simply at different velocities, but each of these clumps is *individually* rotating. In Section (3.5.1), where we discuss using velocity centroid plots to sort out the relative effects of outflow and rotation in line cores, we will show that a gradient is seen in the CS 5 \rightarrow 4 structure associated with the IRAS 12 clump that could be interpreted as rotation.

The velocity structure in the NCL is even more confused. It is

readily apparent that the strong, relatively young, outflow near IRAS 27 is churning up a good bit of the ambient cloud mass. Inspection of the NCL Dec strip maps from $RA = 0'$ to $RA = 3'$ (Figure 3.20) reveals an overall west to east shift in the velocity of the CS gas from about 8 km s^{-1} to about 6 km s^{-1} . A separate clump at 8 km s^{-1} appears prominently at $(3', -5')$ in the $RA = 3'$ map, and is apparently fairly extended in RA (judging from the NCL RA map at Dec = $-5'$). Here, the ambient gas appears relatively unaffected by the outflow. Although the CS line is strongly peaked here, it is not nearly as broad as the CS lines in the cylindrical region encompassing outflow H, it is singly peaked, and the integrated intensity is lower. At Dec = $-4'$ in the RA map, the double-component velocity structure from $RA = 0'$ to $3'$ becomes readily apparent. The NCL RA maps from Dec = 1 to -1 (Figure 3.19) indicate the rotation axis of the cylinder is located approximately at $RA = 1$.

Fig. 3.17. Position-velocity maps in RA at Dec offsets -10, -9, -8, -7, -6, -4, -3, -2, -1, 0 and 1 for the SCL. Contour levels start at 0.4 K and increase in steps of 0.4 K for the maps at offsets -10, -9, 4, 3, and 2, and start at 0.5 K and increase in steps of 0.5 K for the maps at offsets -8, -7, -6, -1, 0, and 1.

Fig. 3.18. Position-velocity maps in Dec at RA offsets 5, 4, 3, 2, and 1 for the SCL. Contour levels start at 0.4 K and increase in steps of 0.4 K for RA offsets 5 and 1, and start at 0.5 K, increasing in steps of 0.5 K for RA offsets 4, 3, and 2.

Fig. 3.19. Position-velocity maps in RA at Dec offsets 1, 0 -1, -2, -3, -4, and -5 for the NCL. Contour levels start at 0.4 K and increase in steps of 0.4 K.

Fig. 3.20. Position-velocity maps in Dec at RA offsets 3, 2, 1, and 0 for the NCL. Contour levels start at 0.4 K and increase in steps of 0.4 K.

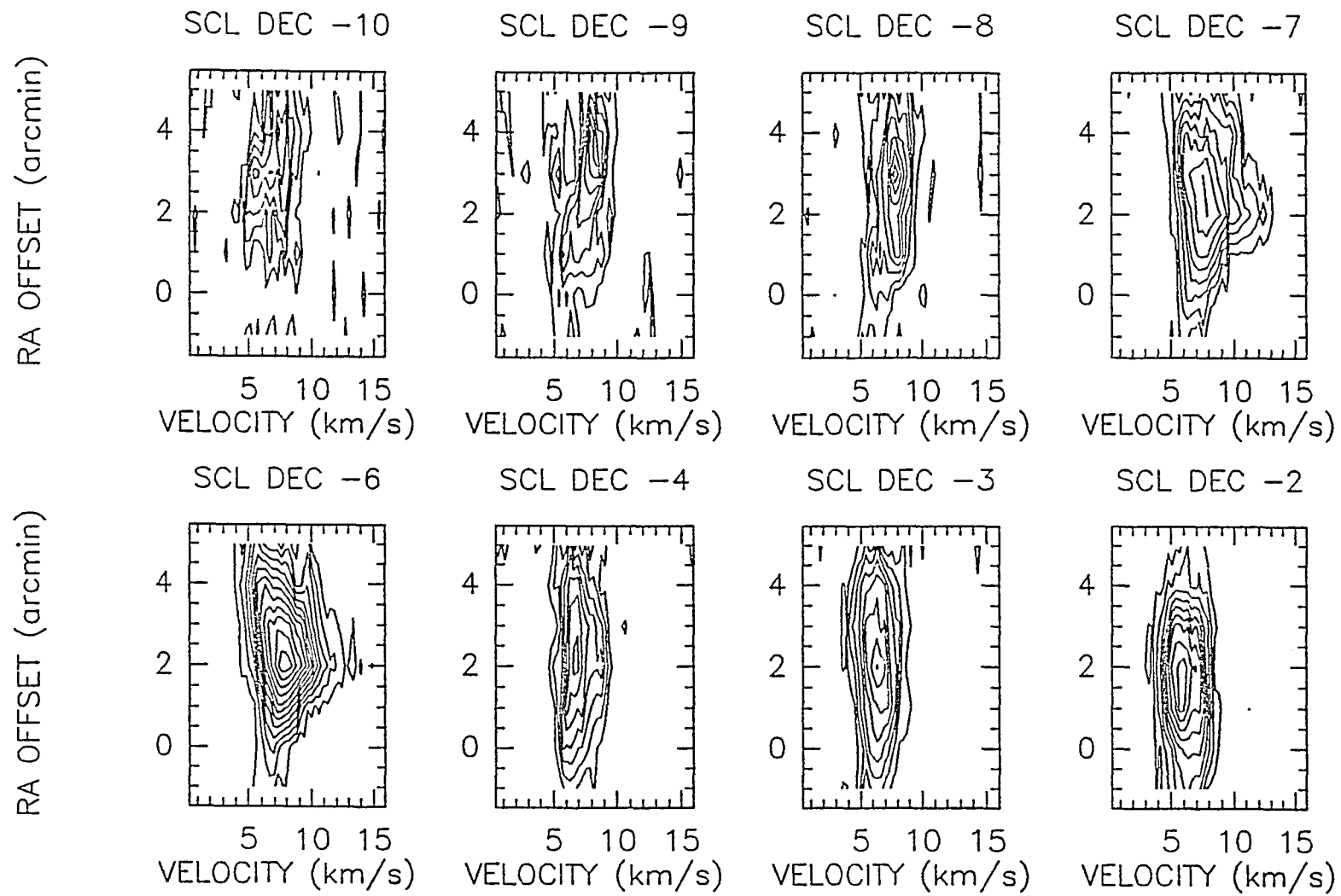


Figure 3.17

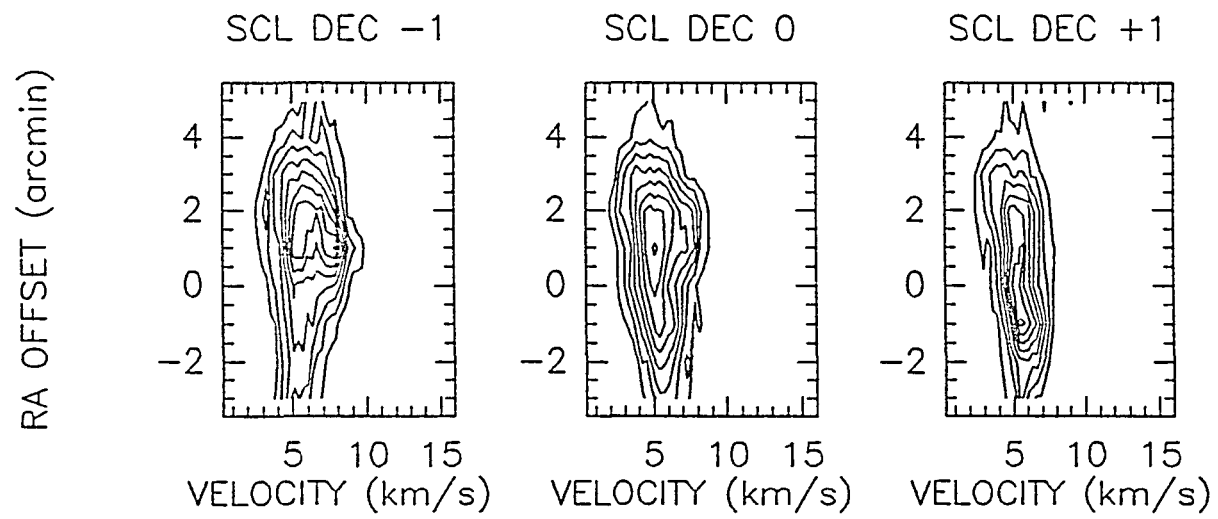


Figure 3.17

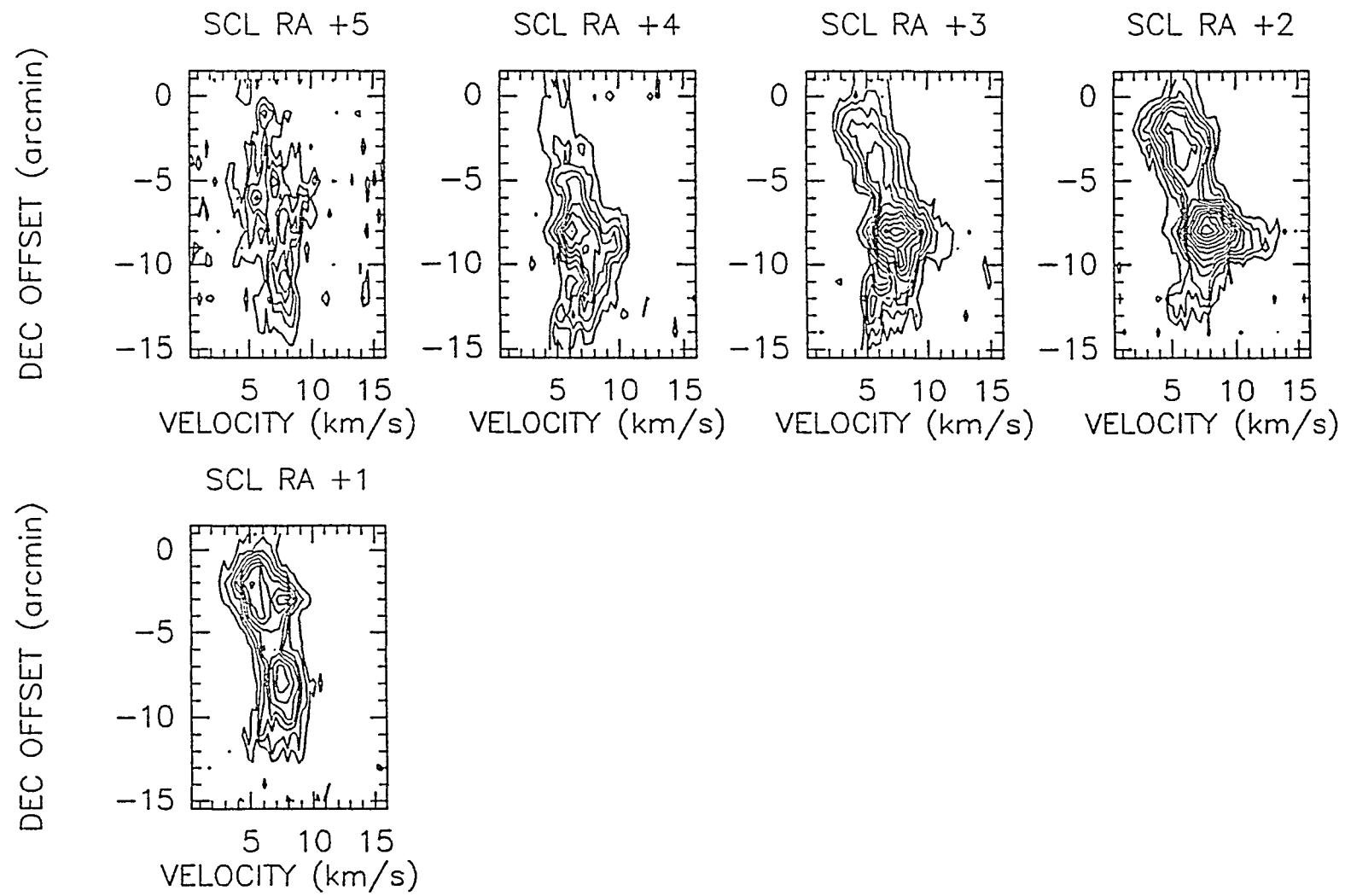


Figure 3.18

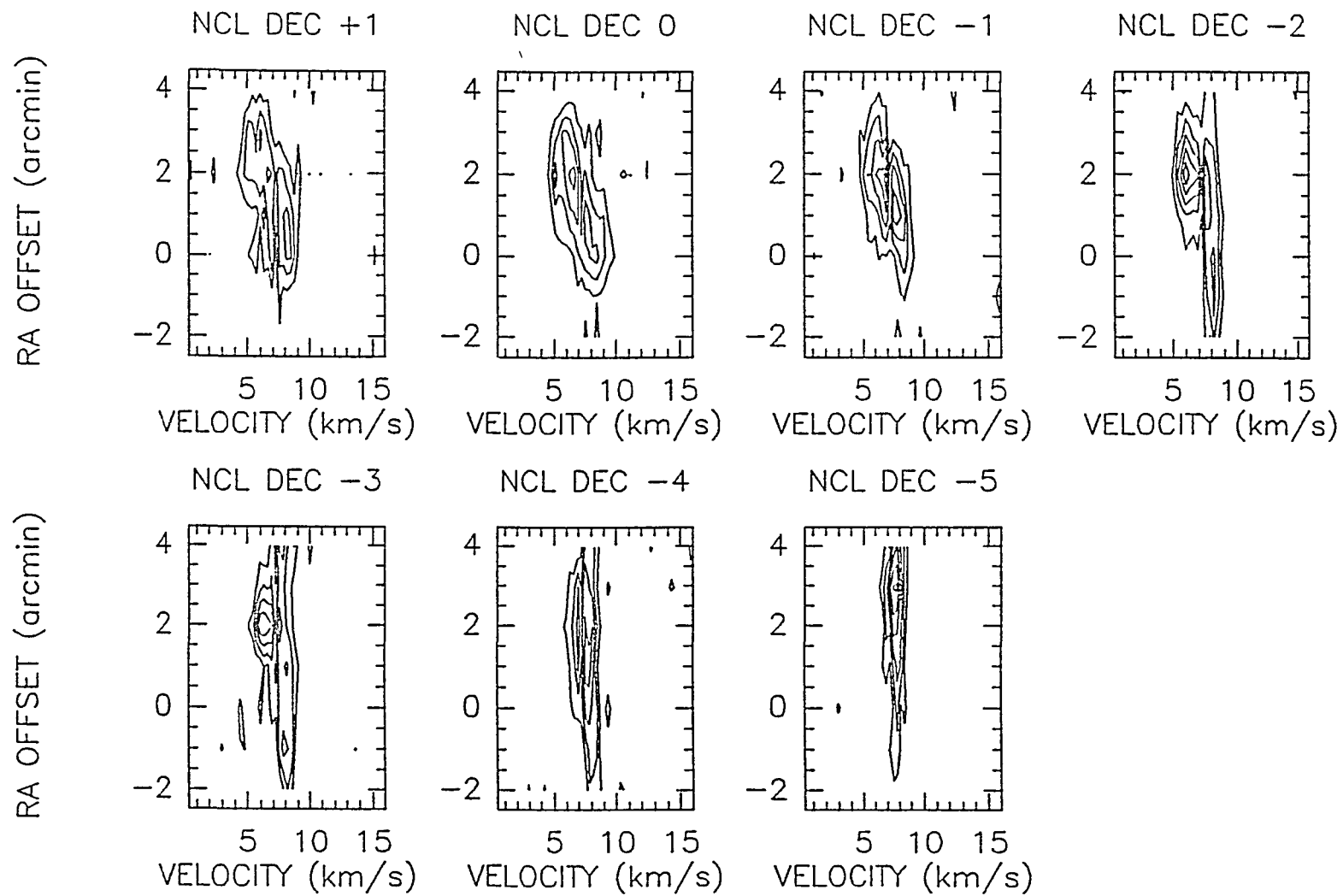


Figure 3.19

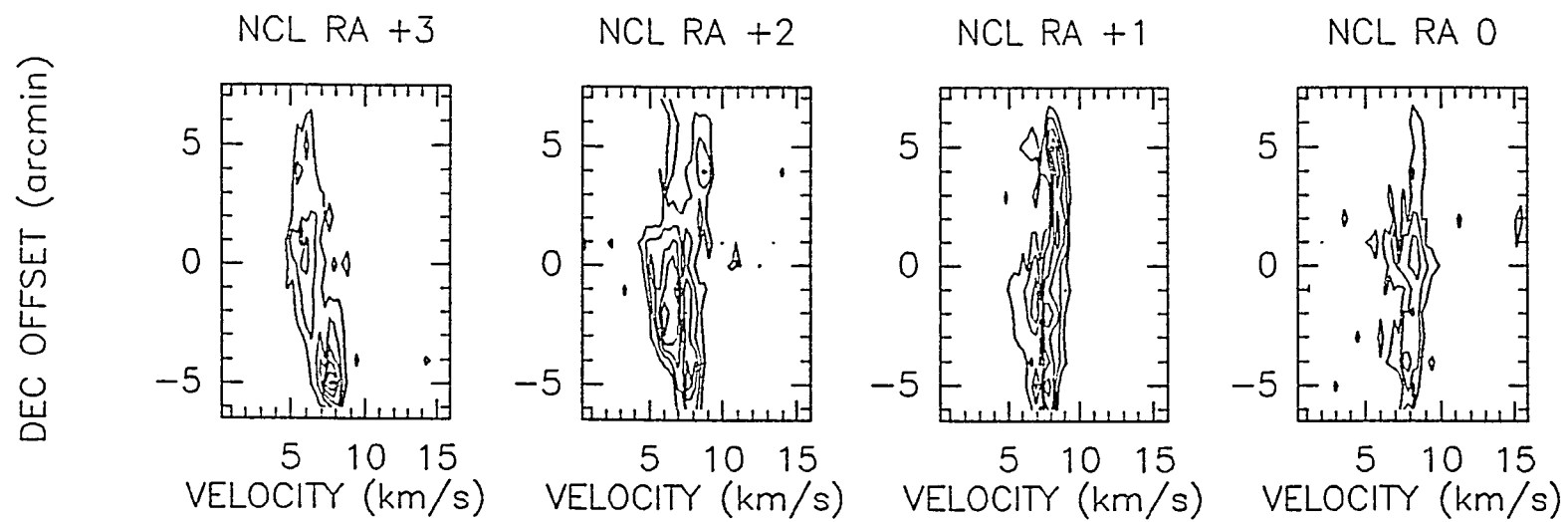


Figure 3.20

3.3.2. Channel Maps

In this section, I will further investigate the velocity structure of the CS gas by inspection of channel maps. Figures (3.21) and (3.22) are maps of the temperature in each channel over the line widths of the CS gas in the SCL and NCL, respectively. The blueshifted CS gas associated with outflow D shows up very clearly in the channel maps from about 2.5 km s⁻¹ to 4.6 km s⁻¹. The maps at 3.4 and 3.7 km s⁻¹, in particular, show a double-peaked structure consistent with emission from a swept-up shell, as do the maps of the redshifted CS gas from 5.6 to 7.4 km s⁻¹. The NW cloud component lies at $v_{LSR} \approx 5.5$ km s⁻¹. At 4.6 or 4.9 km s⁻¹ we start to see some of the blueshifted gas associated with outflow C and core emission from the NW cloud component, which peaks close to the center of the red and blue CO lobes of outflow D. At 5.2 km s⁻¹, we start to see emission in the vicinity of IRAS 6. At 5.6 km s⁻¹, the CS emission splits into two peaks located to the NW and SE of IRAS 12, which bracket the red CO lobe of outflow D. The NW peak has completely disappeared at 8 km s⁻¹, where the peak emission in the NW cloud component is centered approximately one arcminute to the southeast of IRAS 12. As we discussed in Section 3.2.5, the emission may be strongest at this position due to a “molecular ridge” swept up by the outflow. We see an emission peak at this position over the velocity range from about 5.6 - 8.9 km s⁻¹. This is consistent with a picture where the NW and SE peaks about IRAS 12 define the near- and farside lobes of the redshifted outflow emission. The peak emission centered on IRAS 9 occurs at about 8.0 km s⁻¹. At 8.3 km

s^{-1} , we see weak emission in the far SE, at the position of the redshifted CO outflow B. From 9.8 to 10.4 km s^{-1} , the emission about IRAS 9 is extended to the SE. This emission occurs just south of the blue CS lobe, and is likely the same cloud component reported by Krügel et al. (1987) at 10 km s^{-1} . The red CS wing associated with outflow C is apparent from about 10.8 to 13.5 km s^{-1} .

For the NCL, the CS emission about IRAS 25 is very confined and well-peaked on the infrared source. There is little indication of spatial distinction at different velocities.

The velocity structure in the component about IRAS 27 is quite complex. In addition to the detection of outflow H in CS, there are several separate and relatively confined clumps within the region extending from about 5' north of IRAS 27 to 7' south. The blueshifted outflow gas appears in the map at 4.6 - 4.9 km s^{-1} , although at 4.9 km s^{-1} there are also traces of the blueshifted gas associated with the cylindrical region encompassing the outflow. At velocities closer to the line core, the peak of the cylinder emission shifts southward through about 6.5 km s^{-1} , after which it splits into two components: the southern peak at (2',-2'), and a peak at (2',0'). It is likely that the southern enhancement is due to interaction of the very energetic outflow with the ambient gas. A separate CS emission peak splits off from the main cloud at (3',-4') between 7.4 and 8.3 km s^{-1} . The emission associated with this clump shifts westward at redder velocities. This emission may be due to a ridge of molecular material swept up by the high velocity outflow. A shift northward in the main cloud emission occurs at 8.6 km s^{-1} . The weak emission at Dec = 0' from 8.9 - 10.1 km s^{-1} .

s^{-1} may be associated with outflow H.

Fig. 3.21. Channel maps over the CS line width for the SCL. Contours start at 0.4 K and increase in steps of 0.4 K for the velocity ranges from 2.5 to 4.9 km s⁻¹ and from 9.8 to 13.5 km s⁻¹. Contours start at 0.5 K and increase in steps of 0.5 K for the velocity ranges from 4.9 to 9.8 km s⁻¹.

Fig. 3.22. Channel maps over the CS line width for the NCL. Contours start at 0.4 K and increase in steps of 0.4 K for all maps.

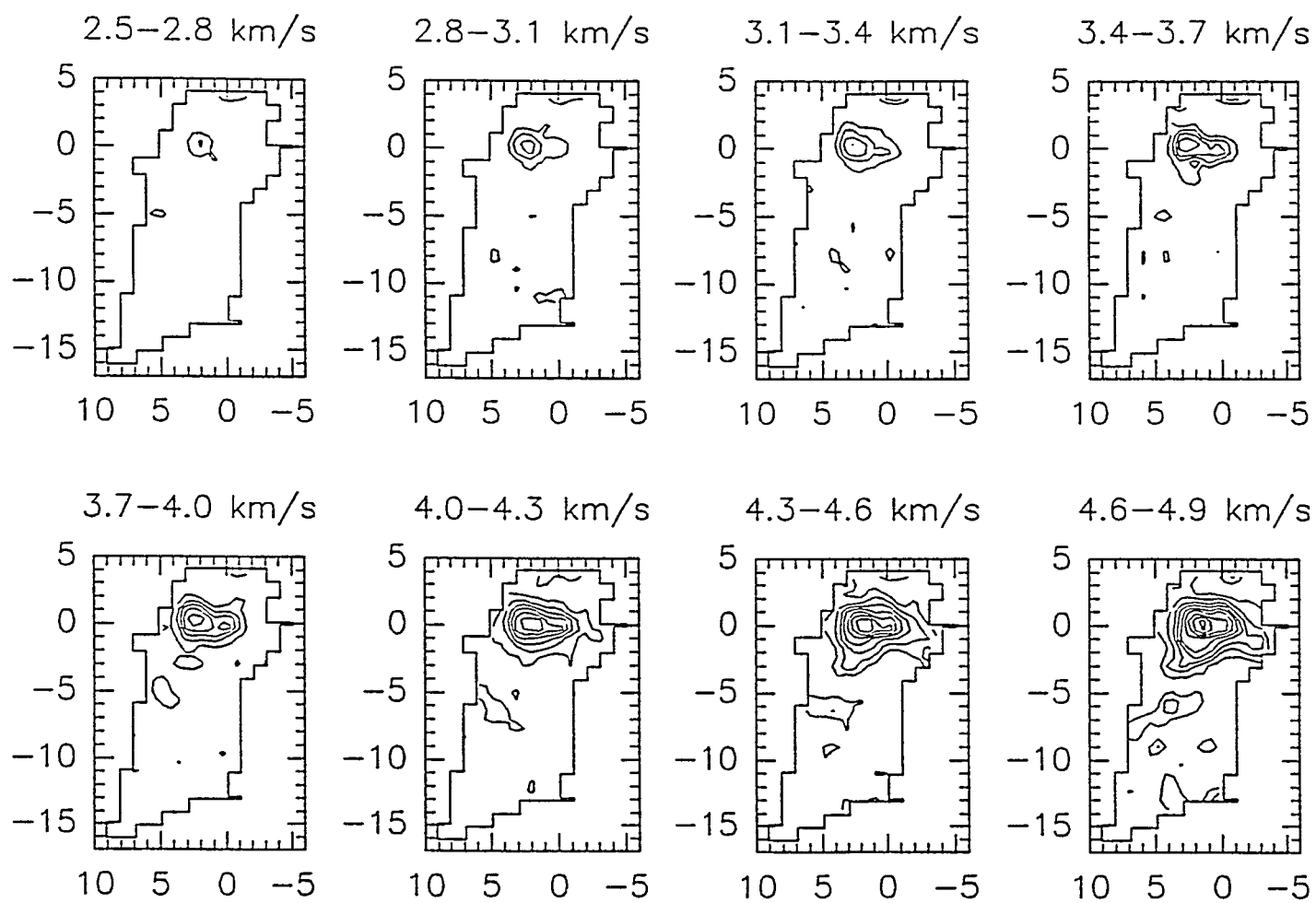


Figure 3.21

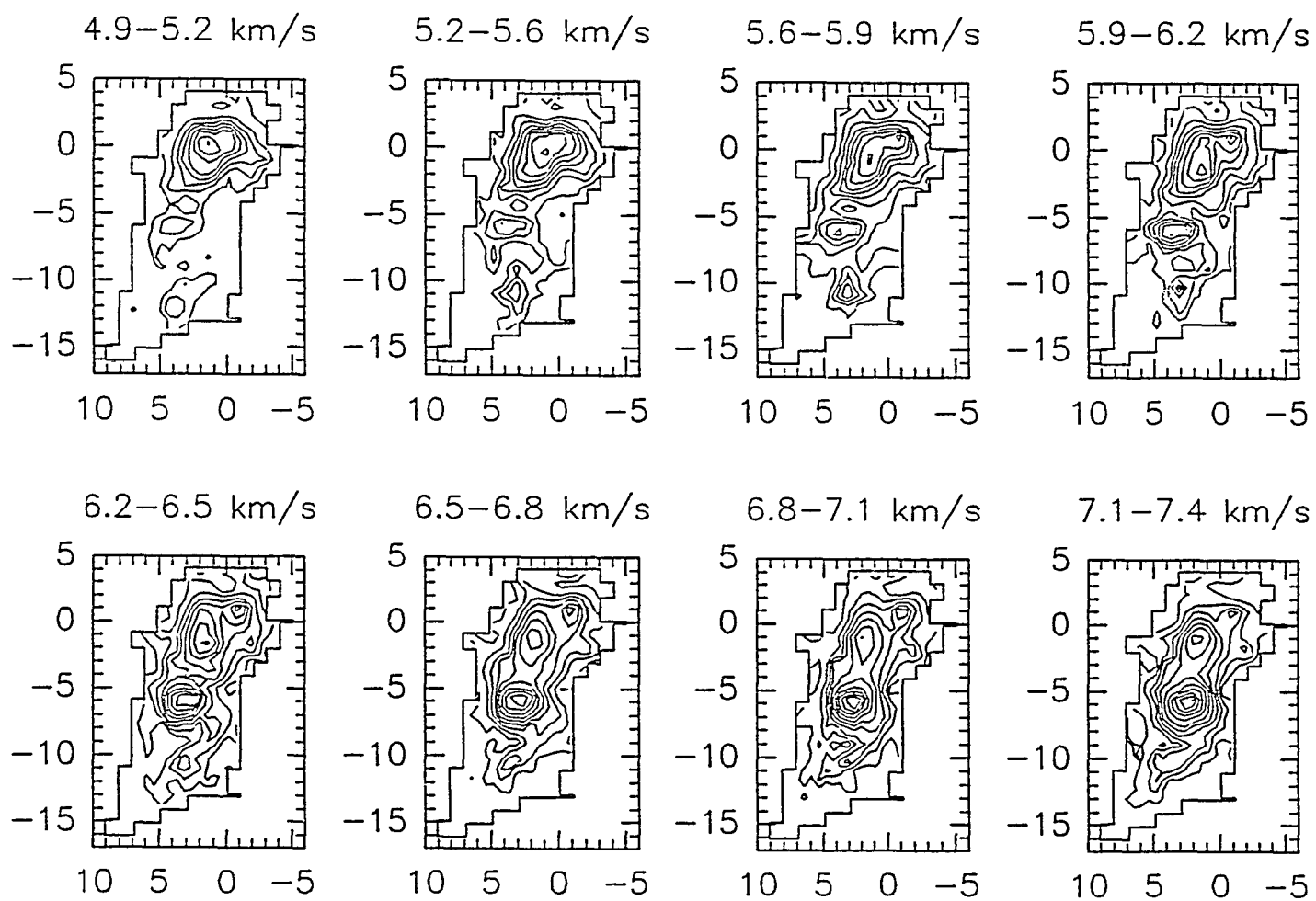


Figure 3.21

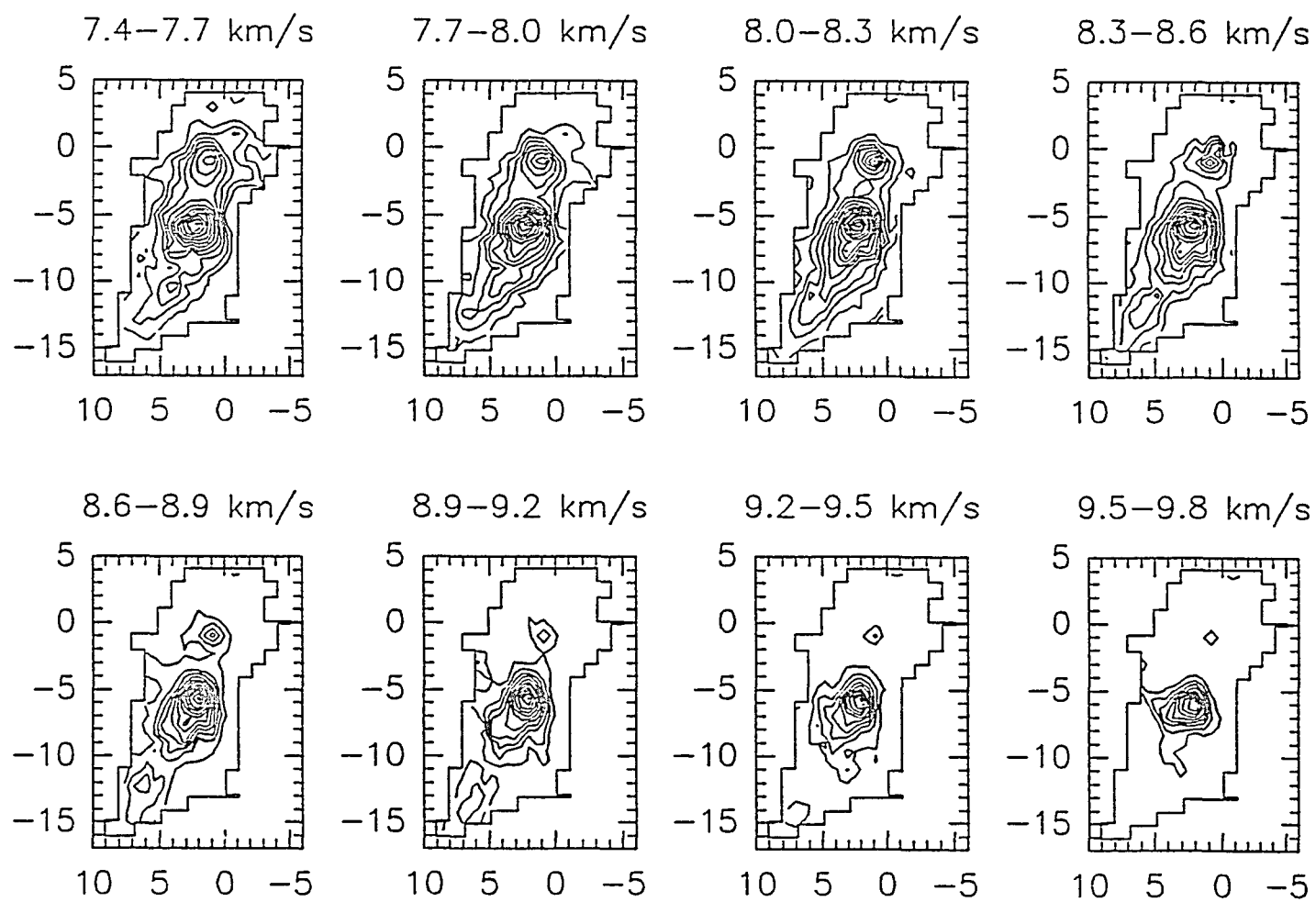


Figure 3.21

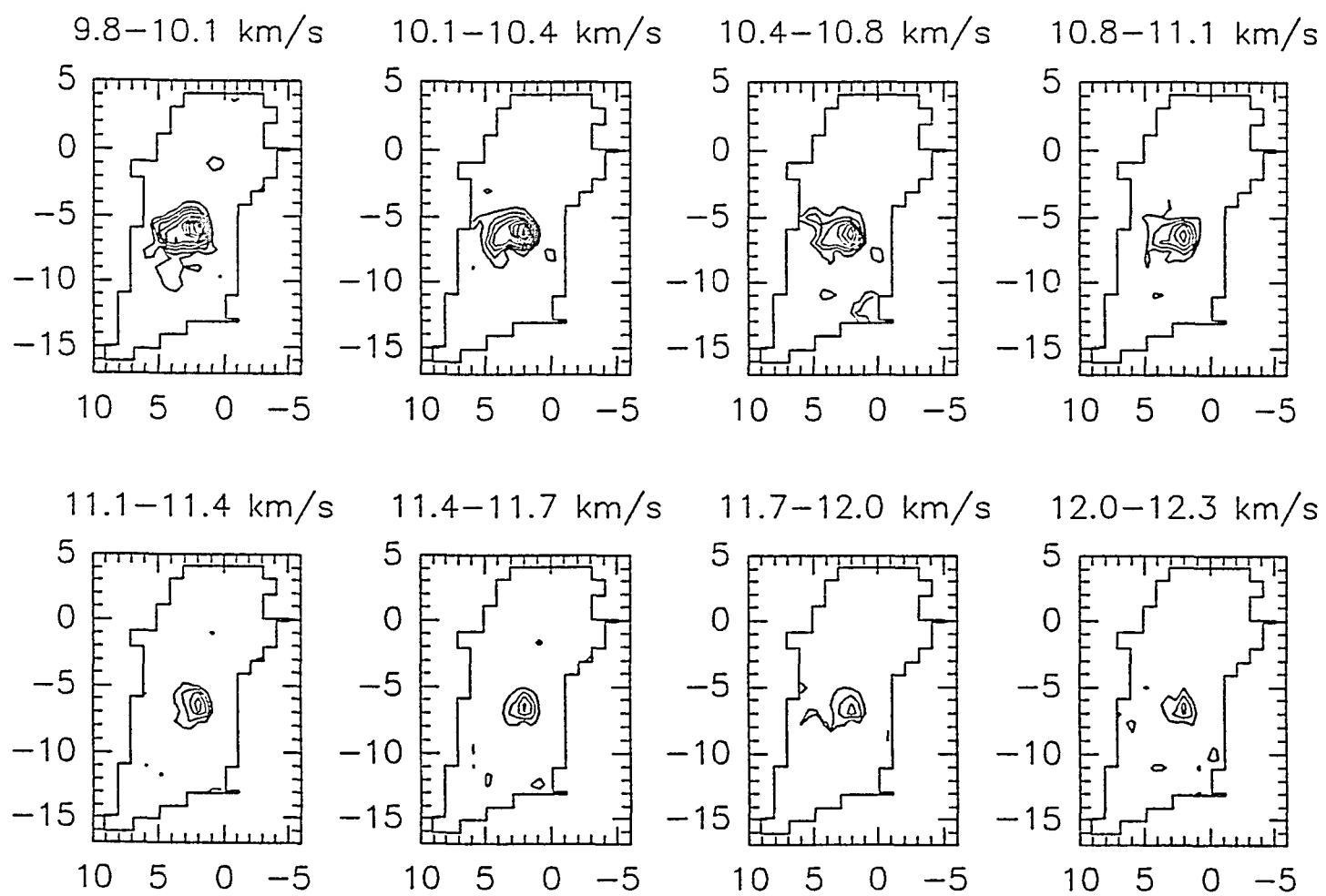


Figure 3.21

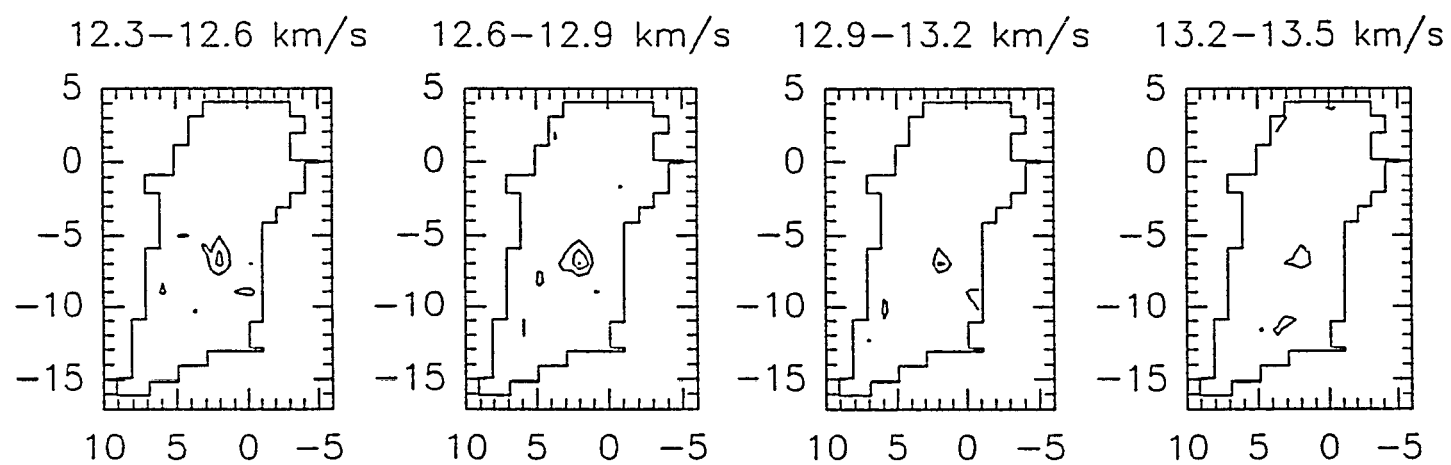


Figure 3.21

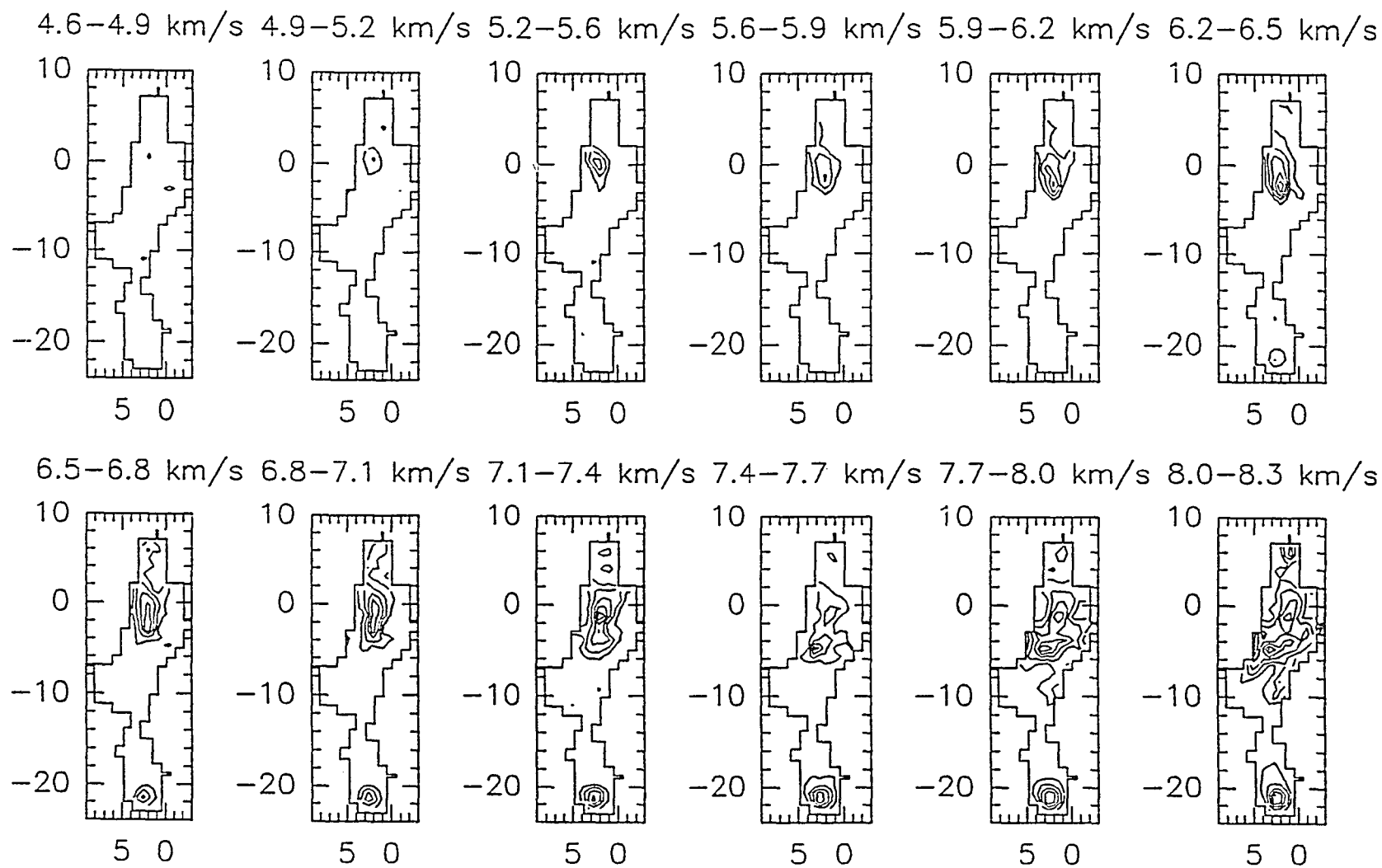


Figure 3.22

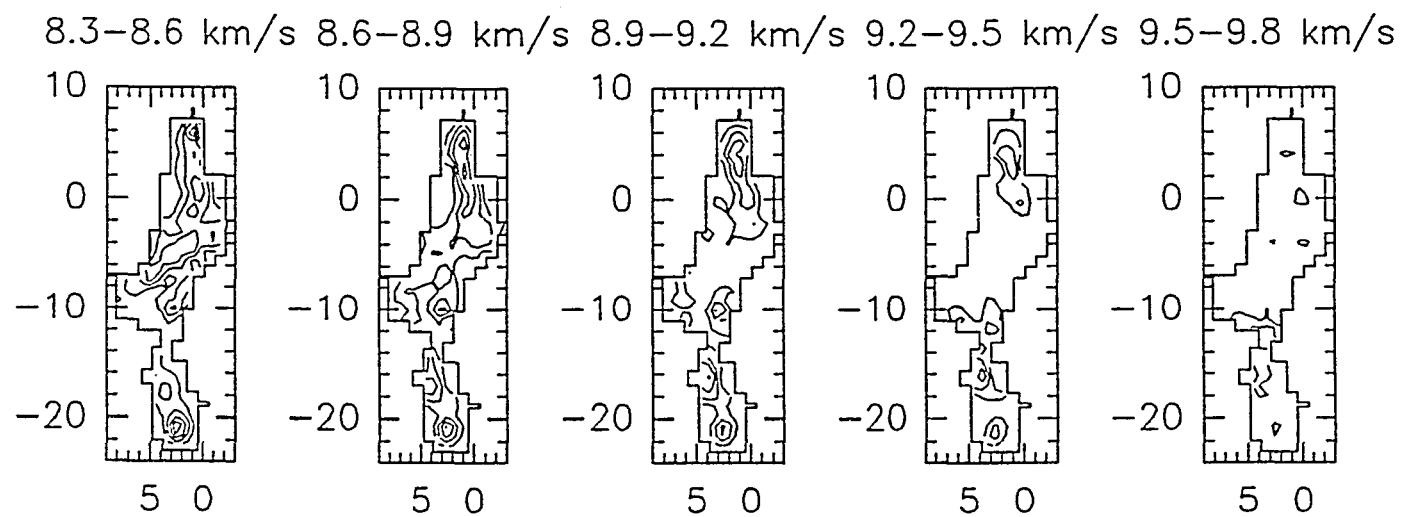


Figure 3.22

3.4. CS LTE Analysis

Tables (3.1) and (3.2) give the results of the column density and mass calculations based on the CS $J=2\rightarrow 1$ and $C^{34}S$ $J=2\rightarrow 1$ data for the SCL and NCL, respectively. Optical depths for the $C^{34}S$ $2\rightarrow 1$ transition were calculated at each position for which the isotope data were available, two positions for each of the two CS clumps that make up the SCL, and two positions in the NCL. The optical depths at each of these positions are used with a weighted area to calculate the mass of the CS clouds, so there are two sets of calculations for each of the two clumps in the SCL, two sets of calculations for the NCL, and a separate calculation of the mass for the cylinder region in the NCL. The $C^{34}S$ optical depths imply the $C^{32}S$ transition is marginally optically thick in these regions, ranging from about 1.3 - 3.0.

The gas kinetic temperature derived from CO and NH_3 observations in the vicinity of Allen's star is approximately 28 K (Black *et al.* 1990, Krügel *et al.* 1987, Schwartz *et al.* 1985). Our calculated CS excitation temperatures tend to be less than one half of the kinetic temperature for an assumed filling factor of one. However, Krügel found the NH_3 gas to be clumpy, with a filling factor of about 0.25. We have run several sets of calculations for different assumed excitation temperatures, using the observed kinetic temperature toward Allen's star as an upper limit to the excitation temperatures for the SCL and NCL. Our results are presented in Tables (3.1) and (3.2). The values we obtained for the hydrogen column density toward Allen's star are in good agreement with values found by others. Krügel et

al. derived values of $8 \times 10^{22} \text{ cm}^{-2}$ and $5 \times 10^{22} \text{ cm}^{-2}$ from C^{18}O and NH_3 data, respectively. Chini et al. (1986) derived a value of 10^{23} cm^{-2} from $350 \mu\text{m}$ dust continuum emission. Walker et al. (1990) derived a value of $2.2 \times 10^{22} \text{ cm}^{-2}$ based on 1.3 mm continuum observations. A direct upper limit of $1.1 \times 10^{23} \text{ cm}^{-2}$ is given by Black et al. (1990) to the hydrogen column density in the foreground of Allen's star. This upper limit is based on lack of detection of absorption lines of the (1,0) vibration-rotation band of H_2 .

3.4.1. Cloud Core Masses

Table (3.3) gives the result of the column density and mass calculations for the CS $J=5 \rightarrow 4$ and CS $J=7 \rightarrow 6$ cores in the SCL.

Figure (2.2) indicates optical depths should be greater in the $5 \rightarrow 4$ and $7 \rightarrow 6$ transitions than the $2 \rightarrow 1$ transition for excitation temperatures greater than about 15 K, so these transitions should be at least marginally optically thick. This implies that the mass estimates based on the assumption that these transitions are optically thin are conservative. We can estimate what the optical depths in the $5 \rightarrow 4$ and $7 \rightarrow 6$ transitions should be in the vicinities of IRAS 9 and 12 based on the previously calculated $2 \rightarrow 1$ optical depths. Table (3.4.a) lists the expected optical depths in these regions for an appropriate range of excitation temperatures. These optical depths are determined from the calculated $2 \rightarrow 1$ optical depths at the positions of IRAS 9, IRAS 12, and the center of outflow D. Table (3.4.b) lists the theoretical line intensity ratios for the optically thin and

thick cases, and the observed line intensity ratios at IRAS 9, IRAS 12, and the center of outflow D.

Although the observed line intensity ratios better fit the optically thick ratios, the fit is very poor. There are several explanations for this. These transitions likely arise from different regions and cannot be well characterized by a single excitation temperature. Also, since the CS 2→1 data exhibit broad line wings in these regions which are indicative of outflow activity, the integrated intensities in these lines relative to the upper level transitions ought to be anomalously high. This is consistent with these transitions probing different regions in the cloud. As will be seen in the next chapter, the CS peak temperatures are also enhanced in these regions. As previously discussed, much of the CS 2→1 emission is likely produced in the region where the outflow impacts the ambient molecular cloud (this will be further explored in the next chapter), but the 5→4 and 7→6 emission is expected to be associated with the densest core regions.

3.4.2. Outflow Masses and Energetics

Table (3.5) gives the results of the column density and mass calculations for the CS outflows in the SCL. Table (3.6) gives the results of the energetics calculations for the CS outflows in the SCL. Δv_{fwi} is the full-width of the CS line at zero intensity.

TABLE 3.1. SCL CS 2→1 COLUMN DENSITIES AND MASSES

τ	T_{ex} (K)	ff	NH ₂ (cm ⁻²)	Mass (M _☉)
ALLEN'S COMPONENT (IRAS 9)				
.100	13.8	1 (set)	8.3×10^{22}	1388.
	15 (set)	.826	9.8×10^{22}	1320.
	20	.595	1.6×10^{23}	1568.
	25	.464	2.4×10^{23}	1830.
	30	.381	3.3×10^{23}	2100.
.140	4.7	1 (set)	2.5×10^{22}	2408.
	5 (set)	.565	2.7×10^{22}	1470.
	10	.218	7.0×10^{22}	1470.
	15	.134	1.4×10^{23}	1748.
	20	.097	2.3×10^{23}	2070.
	25	.075	3.3×10^{23}	2415.
	30	.062	4.7×10^{23}	2768.
NW COMPONENT (IRAS 12)				
.060	10.8	1 (set)	2.3×10^{22}	552.
	10 (set)	.966	2.0×10^{22}	476.
	15	.593	3.8×10^{22}	566.
	20	.427	6.4×10^{22}	672.
	25	.334	9.8×10^{22}	784.
	30	.274	1.4×10^{23}	898.
.116	9.6	1 (set)	5.4×10^{22}	842.
	10 (set)	.815	5.8×10^{22}	735.
	15	.500	1.1×10^{23}	878.
	20	.360	1.9×10^{23}	1043.
	25	.281	2.8×10^{23}	1215.
	30	.231	3.8×10^{23}	1388.

TABLE 3.2. NCL CS 2→1 COLUMN DENSITIES AND MASSES

τ	T_{ex} (K)	ff	NH ₂ (cm ⁻²)	Mass (M _⊙)
NCL				
.136	5.0	1 (set)	1.7×10^{22}	871.
	5 (set)	.678	1.7×10^{22}	585.
	10	.262	4.5×10^{22}	584.
	15	.161	9.0×10^{22}	695.
	20	.116	1.4×10^{23}	826.
	25	.091	2.2×10^{23}	963.
.067	7.1	1 (set)	1.4×10^{22}	467.
	10 (set)	.511	2.3×10^{22}	395.
	15	.314	4.3×10^{22}	470.
	20	.226	7.1×10^{22}	558.
	25	.177	1.1×10^{23}	650.
	30	.145	1.5×10^{23}	746.
CYLINDER COMPONENT				
.136	5.0	1 (set)	1.7×10^{22}	240.
	5 (set)	.678	1.7×10^{22}	161.
	10	.262	4.5×10^{22}	161.
	15	.161	9.0×10^{22}	192.
	20	.116	1.4×10^{23}	228.
	25	.091	2.2×10^{23}	266.

TABLE 3.3. CS 5→4 AND 7→6 COLUMN DENSITIES AND MASSES

τ	T_{ex} (K)	ff	NH ₂ (cm ⁻²)	Mass (M _⊙)
ALLEN'S CS 7→6 COMPONENT				
.013	16.4	1 (set)	2.9×10^{22}	50.5
	20	.739	2.3×10^{22}	30.3
	25	.540	2.1×10^{22}	19.8
	30	.424	2.1×10^{22}	15.4
ALLEN'S CS 5→4 COMPONENT				
.013	25.2	1 (set)	1.5×10^{22}	29.5
	30	.802	1.8×10^{22}	28.0
NW CS 5→4 COMPONENT				
.013	12.2	1 (set)	1.0×10^{22}	23.0
	20	.486	1.1×10^{22}	12.2
	30	.179	1.5×10^{22}	10.3

TABLE 3.4.a. CS 7→6 and 5→4 OPTICAL DEPTHS

T_{ex}	τ_{7-6} (9)	τ_{5-4} (9)	τ_{5-4} (12)	τ_{5-4} (D)
10	0.5	3.1	1.9	3.6
15	3.0	7.0	4.2	8.1
20	7.1	10.4	6.3	12.
25	12.	13.	8.0	15.

TABLE 3.4.b. CS LINE INTENSITY RATIOS

T_{ex}	PREDICTED		
	7-6/5-4 (thin, thick)	7-6/2-1 (thin, thick)	5-4/2-1 (thin, thick)
10	0.13, 0.76	0.14, 0.57	1.03, 0.75
15	0.36, 0.84	0.92, 0.70	2.54, 0.83
20	0.60, 0.88	2.40, 0.77	4.00, 0.87
25	0.81, 0.91	4.26, 0.81	5.24, 0.89
Source	OBSERVED		
	7-6/5-4	7-6/2-1	5-4/2-1
Brightness Temperature Ratios			
IRAS 9	1.3	0.89	0.67
IRAS 12			0.32
Outflow D			0.63
Integrated Intensity Ratios			
IRAS 9	0.87	0.47	0.54
IRAS 12			0.19
Outflow D			0.27

TABLE 3.5. CS OUTFLOW COLUMN DENSITIES AND MASSES

Outflow	τ	T_{ex} (K)	ff	NH ₂ (cm ⁻²)	Mass (M _⊙)
B (blue)	.013	3.5	1 (set)	1.5×10^{21}	94.5
		10 (set)	.104	4.5×10^{21}	29.3
C (blue)	.054	4.4	1 (set)	9.0×10^{21}	111.
		10 (set)	.192	2.7×10^{22}	62.3
C (red)	.100	3.5	1 (set)	2.0×10^{22}	124.5
		10 (set)	.083	7.5×10^{22}	38.3
D (blue)	.013	8.6	1 (set)	4.2×10^{21}	50.3
		10 (set)	.695	5.3×10^{21}	44.3
D (red)	.113	5.6	1 (set)	2.8×10^{22}	269.
		10 (set)	.326	6.5×10^{22}	200.

TABLE 3.6. CS OUTFLOW ENERGETICS

Outflow	Δv_{fuzi} (km s ⁻¹)	τ_d (yrs)	MV (M _⊙ km s ⁻¹)	L (L _⊙)
B	11.0	1.0×10^5	161. - 520.	.68 - 2.3
C	12.0	9.5×10^4	604. - 1410.	3.1 - 7.2
D	10.0	1.7×10^5	975. - 1283.	35. - 40.

3.5. CS Dynamical Analysis

In the following three sections, we discuss the implications of centroid velocity plots, and derive dynamical masses for the NCL cylinder region and SCL cores.

3.5.1. Observed Centroid Velocity Plots

Figures (3.23) a) and b) are maps of the CS $2\rightarrow 1$ and CS $5\rightarrow 4$ velocity centroid in the region of outflow D in the SCL, and the CS $2\rightarrow 1$ velocity centroid in the region of outflow H (the cylinder region) in the NCL, respectively. These are maps of the velocity centroid calculated over the *line core only*. The CS $2\rightarrow 1$ contours in the map about outflow D indicate both the presence of outflow (the velocity gradient from the NE to the SW) and *possibly* rotation (the velocity gradient from the NW to the SE). It is unclear whether there is rotation of a disk-like structure about IRAS 12, or whether the velocity gradient from the NW to the SE reflects the velocity difference between the CS clump about IRAS 12 and the clump about IRAS 9. It is not entirely clear whether this velocity difference reflects rotation of these two clumps about each other, or simply indicates the two clumps have different velocities. In either case, the outflow is dramatically seen in the gradient from the NE to the SW, indicating that a large percentage of the gas in the core has been entrained in the outflow. The CS $5\rightarrow 4$ contours primarily reveal the NW to SE gradient, and indicate this clump may be rotating. The NE to SW gradient, indicative of the

outflow, is nearly absent in this map, indicating the absence of outflow gas in this transition. However, the two contours at the NE and SW corners may be due to the effect of the outflow. This would be consistent with the extensions observed in the $5 \rightarrow 4$ integrated intensity map (Figure 3.13b). The morphology of the $5 \rightarrow 4$ integrated intensity map suggests that the outflow has broadened the spectral lines along the direction of outflow. We do not include velocity centroid maps of the core about Allen's IRS (outflow C) because the velocity structure is very chaotic. In Section (3.5.3) we will discuss the implications of this.

The almost-vertical contours in the outflow H velocity centroid map indicate rotation of an elongated structure about a N - S axis. This is the "rotating cylinder" we referred to in Section (3.3). In Section (3.5.1), we will explore the implications of such a structure.

Fig. 3.23. Velocity centroid maps for the regions of outflows D and H. Positional offsets are in arcminutes. (a) CS 2→1 contours (solid lines) increase from 5.2 to 6.0 km s⁻¹ from the NE to the SW. The contour in the NW corner is at 5.6 km s⁻¹. CS 5→4 contours (dashed lines) increase from 5.2 to 6.0 km s⁻¹ from the NW to the SE. The contour in the NE corner is at 5.4 km s⁻¹, and in the SW corner is at 6.0 km s⁻¹. (b) CS 2→1 contours increase from 6.8 to 8.8 km s⁻¹ from E to W. The contours north of about 2' are due to the cloud component at the northern end of the NCL.

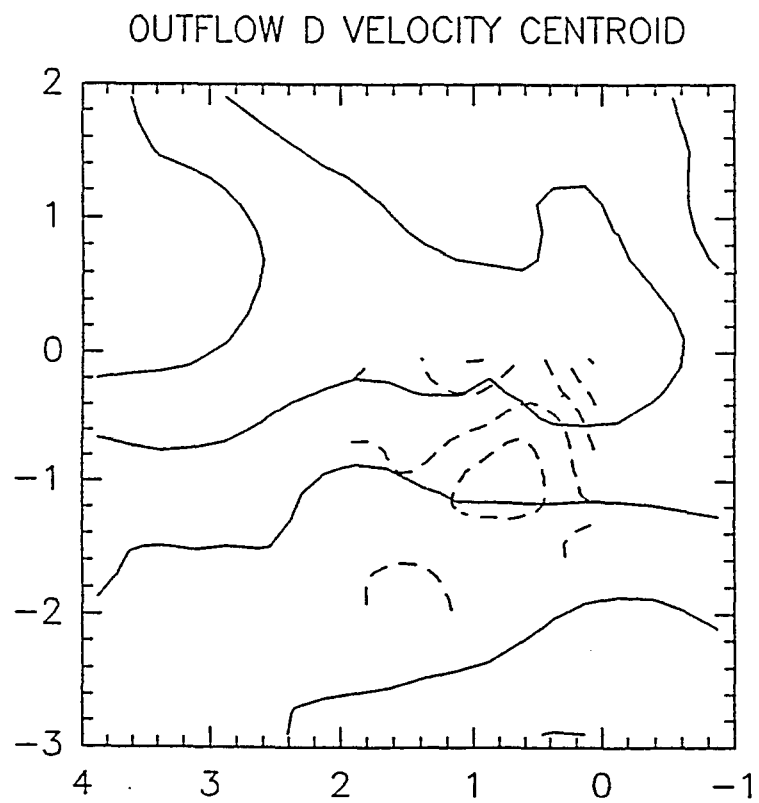


Figure 3.23a

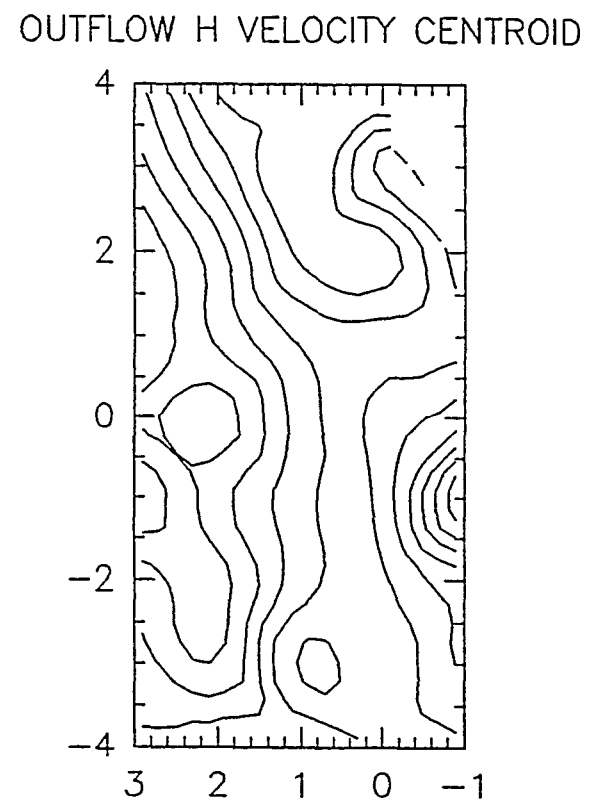


Figure 3.23b

3.5.2. The NCL Cylindrical Structure

In this analysis we will investigate the dynamics of the cylindrical structure in the NCL. We use two extremes of the virial theorem; one which describes a spherical distribution of mass, and one which describes an elongated cylinder, or filament, where the radius of the cylinder is small compared to the length. We will include the effects of rotation and explore the possible effects of a magnetic field.

In steady state, the scalar virial theorem for an ideal gas reduces to:

$$2(T + U) + M + \Omega = 0,$$

where T is the total kinetic energy, U the total internal energy, M the total magnetic energy, and Ω the total gravitational potential energy. I will neglect the effects of magnetic fields for the present. The general expression for the gravitational potential energy of a distribution of mass is:

$$-\Omega = \int \rho \mathbf{r} \cdot \nabla \Phi dV.$$

For a spherical distribution of mass, this expression reduces to:

$$-\Omega = G \int_0^R \frac{M(r) dM(r)}{r}$$

$$\Omega = -c_1 \frac{GM^2}{R}.$$

The constant c_1 depends upon the mass distribution.

The internal energy:

$$U = \frac{1}{2} M \sigma_{3D}^2,$$

may be calculated from the observed three dimensional velocity dispersion:

$$\sigma_{3D} = \left(\frac{8}{3} \ln 2\right)^{-\frac{1}{2}} \Delta v_{FWHP}.$$

Δv_{FWHP} is the full-width of the observed spectral line at half power.

The rotational kinetic energy may be expressed as:

$$T_{rot} = \frac{1}{2} \int \rho v_{rot}^2 dV$$

$$T_{rot} = c_2 M v_{rot}^2.$$

The constant c_2 depends upon the velocity curve.

The mass distribution and velocity curve are related; a flat velocity curve, that is $v(r)$ constant, implies $\rho \sim r^{-2}$. For a constant density sphere, $v(r) \sim r$ (solid body rotation).

Many molecular clouds are composed of elongated filamentary or cylindrical structures which are not adequately described by a spherical form. For an elongated cylinder ($L \gg R$), the general expression for gravitational potential energy may be integrated to yield:

$$\Omega = -c_3 \frac{GM^2}{L},$$

where again, the constant c_3 depends upon the mass distribution.

For the geometry of the cylindrical structure, the two expressions for Ω differ by only about 6%. Neglecting magnetic fields, the Virial mass this region is between about 450 and 800 M_{\odot} , depending upon whether an inverse square or constant density law is used.

If the magnetic field strength is known, the total magnetic energy may be calculated:

$$M = \frac{1}{8\pi} \int B^2 dV.$$

Myers and Goodman (1988) found that measurements of the magnetic field strength, velocity dispersion, and size of 14 sample molecular clouds agreed, to within a factor of ~ 2 , with the predictions of a simple model in which the magnetic, kinetic, and gravitational energies are all equal. In such a model,

$$B_{eq} \approx \frac{3}{8 \ln 2} \left(\frac{5}{G} \right)^{1/2} \frac{\Delta v_{FWHP}^2}{R}. \quad (3.1)$$

This expression is valid for a uniform, spherical cloud.

A major difficulty in putting together a coherent picture of how the structure of the NCL may be affected by the magnetic field is that neither the direction nor field strength are well-known in this region. In a large-scale CO survey of molecular clouds in Monoceros and Orion covering 850 deg^2 of sky, Maddalena et al. (1986) noted that while the main molecular clouds, Orion A, Orion B, and Mon R2 are elongated in a generally north-south orientation, two long filaments more than 10° in length are elongated in a generally east-west direction. The Mon OB1 cloud is not

incorporated in their map, but was studied previously by Blitz (1978) and although is smaller, spanning roughly $2^\circ \times 0.5^\circ$, has the same general elongation as the Orion and Mon R2 clouds. Since collapse should proceed along the magnetic field, resulting in a flattened structure perpendicular to the direction of the magnetic field, Vrba (1977) proposed that filamentary structures *parallel* to the magnetic field, such as those observed in ρ Oph, might be formed by material streaming either into or away from the main cloud. Maddalena et al. noted that this scenario fit the observed structure of the Orion/Monoceros clouds well.

If the magnetic field has a generally east-west orientation in the vicinity of Mon OB1, this would be in agreement with the north-south elongation of the cloud. This picture fits well with the morphology of the outflows and cores in the SCL, but does not fit with rotation of an elongated structure in the NCL along a north-south axis, or with the north-south orientation of the axis of outflow H, which would be better fit if the magnetic field had a north-south orientation.

One possibility is that we are not just seeing rotation about a north-south axis, but a combination of effects from possible rotation, outflow, and separate velocity components. This model is consistent with the complex appearance of the channel maps. However, the geometry of outflow H suggests that the collimating structure of this outflow should be orthogonal to the general elongation of Mon OB1.

It is interesting to investigate the possibility of the rotation of a long cylinder. Assuming its rotation axis is parallel to its elongation (N-S), under what conditions could such a structure be confined? If the magnetic

field is aligned in a N-S direction in this portion of the cloud, we can estimate the magnetic field strength required to balance the gas pressure in this region with the magnetic field pressure:

$$\rho \Delta v_{FWHP}^2 \approx \frac{B^2}{8\pi}.$$

In this expression the effects of rotation are neglected, therefore a value of B derived from this expression should be considered an upper limit. The gas density may be estimated from the LTE mass calculated for the cylindrical region and an assumed cylindrical geometry. Taking $M \sim 200 M_{\odot}$, the radius and length of the cylinder to be approximately 0.23 pc and 1.63 pc, respectively, we estimate a value of ρ for the cylinder of $5.0 \times 10^{-20} \text{ gm cm}^{-3}$. Given the line width in this region is about 2.5 km s^{-1} , substitution into equation (3.1) yields a value of $B \approx 280 \mu\text{G}$. It should be noted here that the effects of rotation will be fairly insignificant, since v_{rot} is approximately 1 km s^{-1} and:

$$\frac{E_{rot}}{V} = \frac{\rho v_{rot}^2}{2} \ll \rho \Delta v_{FWHP}^2$$

A magnetic field strength of 280 μG is comparable to the strength measured for Orion A.

Since the virial mass of this structure is roughly three to four times the LTE mass, this structure is probably not gravitationally bound. The most likely explanation for the unusual geometry of this structure, which does not require any mechanism of confinement, is that this structure is the remnants of a rotating cloud which has been disrupted by the

outflow. In this picture, the outflow is expanding a hollowed-out, swept-up cylindrical shell. The close association between the outflow and CS morphology supports this picture. It is interesting to note that the average density of this region, based on the LTE mass and an assumed cylindrical volume for the region, is a little over an order of magnitude lower than the critical excitation density for the $2 \rightarrow 1$ transition at an excitation temperature of 10 K. Assuming the gas is thermalized, this implies an area filling factor of about 0.2. Therefore, the CS emission probably arises in a thin, swept-up shell which forms the “wall” of the cylinder. Figure (3.24) is a cartoon that illustrates this picture. At high opacities with low escape probabilities, and at higher temperatures, the critical excitation densities may be considerably lowered, however the LTE analysis indicates the CS $J=2 \rightarrow 1$ optical depths are only moderately optically thick. However, the CS lines are self-absorbed in this region.

It is interesting to consider whether this cylinder could be the remnant of the original circumstellar nebula of IRAS 27 that has been dispersed by the outflow. Conservation of angular momentum requires that $R_{init}v_{init} = R_{fin}v_{fin}$. For an observed rotational velocity of 1.0 km s^{-1} , and radius of 0.46 pc, at a radius of about 0.01 pc (circumstellar-size), the rotational velocity would have to be about 46 km s^{-1} at a radius of about 0.01 pc (circumstellar size). A rotational velocity of 46 km s^{-1} is roughly a factor of 5 too high for such a structure to be gravitationally bound. Therefore, it is likely this structure is part of a larger region encompassing the original circumstellar nebula.

Depiction of outflow H and the CS structure

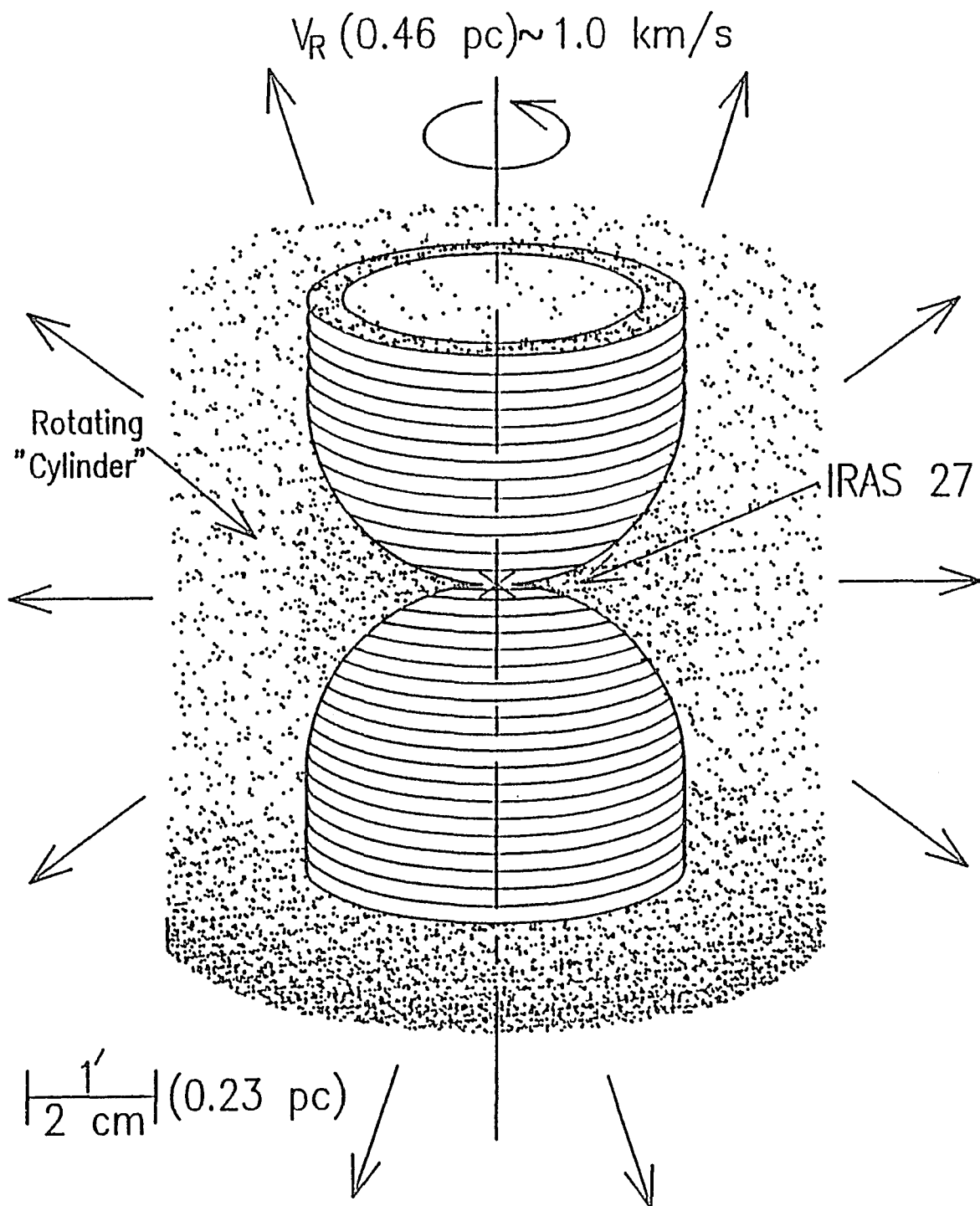


Fig. 3.24. Illustration depicting the swept-up cylinder in the NCL.

Depiction of the SCL outflows

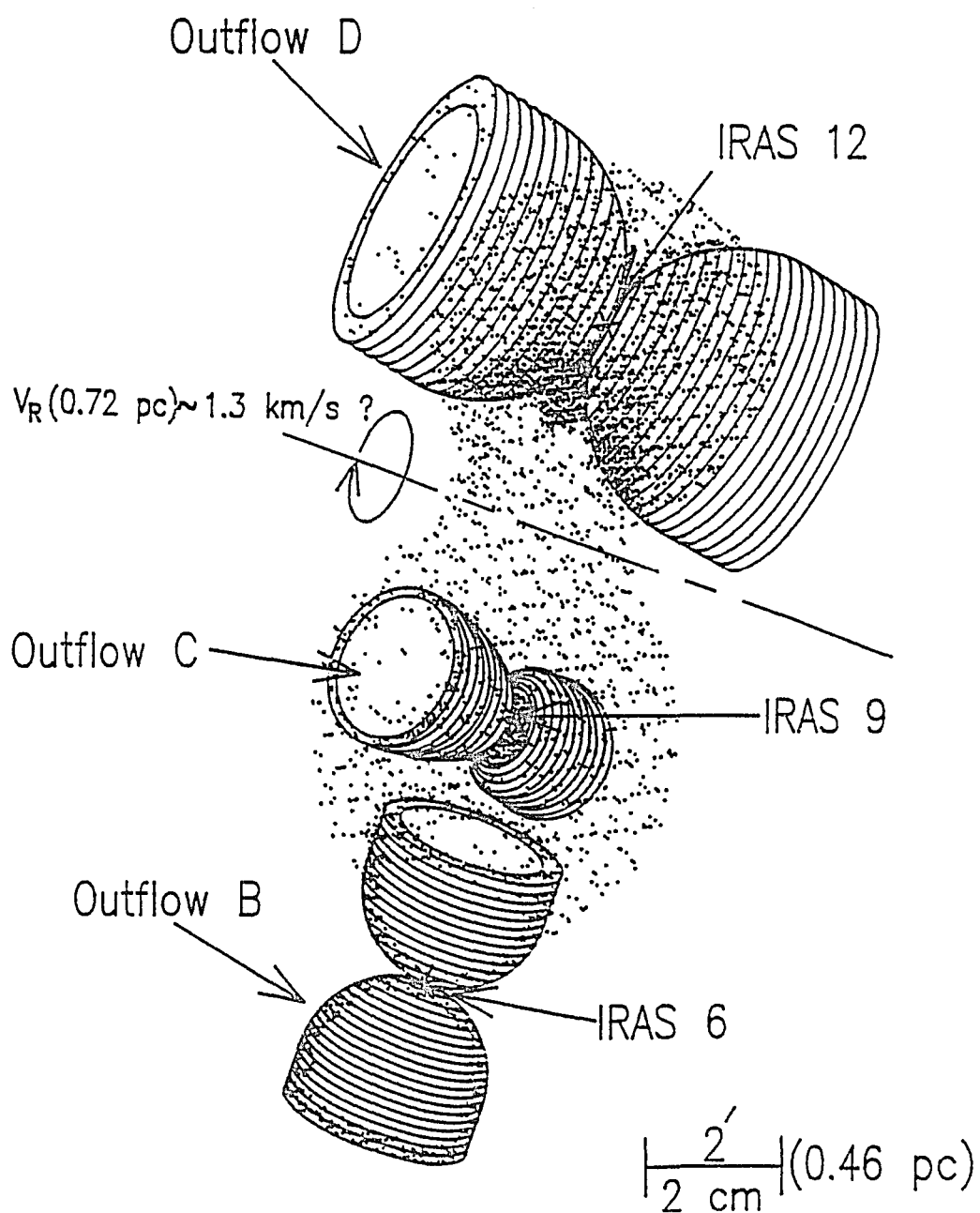


Fig. 3.25. Illustration depicting the relationship of outflows, cores, and YSOs in the SCL.

3.5.3. The SCL CS 5→4 and 7→6 Cores

The velocity structure of the CS 5→4 and 7→6 data is very confused and there is no definite evidence for rotation of these cores, although the large-scale velocity gradient from IRAS 12 to IRAS 9 is reflected in the 5→4 velocity centroid map about IRAS 12. It is possible to place an upper limit on the dynamical mass in these regions using the virial theorem and neglecting rotation. If rotation is present, the rotational velocities are less than 0.5 km s^{-1} at radii of $1'$ (0.23 pc). This makes the rotational terms negligible compared to the internal energy terms based on observed linewidths of $2.6 - 3.0 \text{ km s}^{-1}$ in these regions. The virial mass for these regions is given by:

$$M_{vir} = \frac{R(\sigma_{3D})^2}{c_1 G},$$

where $c_1 = 3/5$ for constant density and $c_1 = 1$ for $\rho \propto r^{-2}$. The virial masses for the 7→6 and 5→4 regions about IRAS 9 are approximately $260 M_\odot$ and $434 M_\odot$, respectively, and $326 M_\odot$ for the 5→4 region about IRAS 12. These are about an order of magnitude larger than the LTE masses of these regions. The difference may be reconciled if the outflows are disrupting the cores. We will explore this further in chapter 5. Figure (3.24) illustrates the relationship between outflows and cores in the SCL.

3.6. Comparison of Different Techniques

Several assumptions are made in the LTE analysis which may not be very well-founded. First, the assumption that the CS transitions are

thermalized may not be correct and is shakier for the higher transitions. Also, the CS isotope abundance ratio enters in the calculation for optical depth as $\exp(-A\tau^{34})$, where A is the abundance ratio $C^{32}S/C^{34}S$, so even small errors in abundance assumptions will result in relatively large errors in the optical depth. Also, calculating the H_2 column density from the $C^{34}S$ column density involves assuming an isotope ratio and a CS/H_2 ratio. Filling factors are not known a priori, so we must either assume a filling factor to calculate excitation temperatures or vice versa. Fortunately, certain errors tend to cancel out in the mass determination. For example, lower filling factors imply higher excitation temperatures.

Since Mon OB1 is a well-studied cloud, it is possible to compare some of my results with independent mass estimates found in the literature. Krügel et al. obtained independent H_2 column density and mass estimates for the SCL using $C^{18}O$ and NH_3 data and the submm dust continuum measurements of Chini et al. (1986). Their column density, density, and mass estimates over this region agree with ours to within a factor of two. In fact, they derive a column density estimate towards IRAS 9 from the $C^{18}O$ $J=1\rightarrow0$ data of $N_{H_2} = 8\times10^{22} \text{ cm}^{-2}$, in close agreement with our estimate (Table 3.1). This is especially encouraging because of the different sets of assumptions made in each technique. The LTE assumption is probably good for the $C^{18}O$ $1\rightarrow0$ transition. Also, each of the mass estimates relies on assuming different fractional abundances of the molecules used relative to H_2 .

The LTE results for the CS $7\rightarrow6$, $5\rightarrow4$, and $2\rightarrow1$ line ratios suggest that these transitions can not realistically be characterized by a

single excitation temperature. This is not surprising as the morphology of the maps suggests these transitions arise in very different regions and the densities required for the thermalization of the higher transitions is quite high; approximately $7.5 \times 10^6 \text{ cm}^{-3}$ for the $5 \rightarrow 4$ transition at 20 K.

The dynamical masses are larger than the LTE masses by factors of about four for the NCL cylinder and about ten for the SCL CS $5 \rightarrow 4$ and $7 \rightarrow 6$ cores. A possible explanation of the discrepancy could be low CS abundances. The fact that our mass estimate for the SCL is approximately a factor of two higher than Krügel's mass estimate based on NH_3 data suggests that this is unlikely. Actually, CS abundances may be enhanced in these regions. The most likely explanation for the discrepancy between the LTE and virial masses is that the virial masses are overestimates because the outflows are disrupting the cores.

3.7. Summary

In this chapter, we have shown that there exists a significant dense, low-velocity component to the most massive outflows in Mon OB1. The low-velocity component to the outflows in this cloud has been identified by asymmetric line wings in both the C^{32}S and C^{34}S $2 \rightarrow 1$ data in the vicinities of the outflows, by the spatial separation of the blue- and redshifted gas about the suspected driving sources, and by the differences in the spatial distributions of the gas traced by the CS $2 \rightarrow 1$, $5 \rightarrow 4$, and $7 \rightarrow 6$ transitions. The velocity ranges for the asymmetric line wings in the CS spectra lie *within* the line cores of the CO spectra used originally to identify the

outflows in this cloud. In addition, velocity centroid plots of the CS line *cores* in the outflow regions indicates that a significant portion of this gas has also been entrained in the outflows. The implications of this will be further discussed in chapter 5.

Dynamical masses for the 5→4 and 7→6 cores in the SCL are about an order of magnitude greater than the LTE masses. The dynamical mass for the 2→1 cylinder region in the NCL is approximately four times the LTE mass. Possible explanations for this result include outflows disrupting the cores, CS abundances lower than terrestrial abundances, the Virial masses being upper limits due to neglecting the effects of rotation and magnetic fields for the 5→4 and 7→6 cores, and the assumption that the CS 5→4 and 7→6 transitions are optically thin. The Virial masses computed for these regions assume a constant density. If an r^{-2} density law is adopted, the Virial masses are lowered by almost a factor of 2, but still significantly exceed the LTE masses.

The existence of a large low-velocity outflow component has important implications for the question of how molecular clouds are supported against collapse. Since the CS emission traces this component so well, it would be beneficial to search for lower-velocities outflows in molecular clouds, or regions of molecular clouds, that are apparently quiescent and do not show evidence of outflow activity in broad CO line wings. The morphology of the CS emission, combined with mapping the velocity centroids over the area of emission, will help sort out the relative signatures of outflows and rotation of dense core regions. In the next two chapters, we will present the results of our CS search around IRAS sources

unassociated with CO outflows and explore the overall dynamical effects of the outflows in the Mon OB1 cloud.

CHAPTER 4

RELATIONSHIP OF DENSE GAS TO YSOS

4.1. Introduction

YSOs are often associated with dense cores in molecular clouds. In the last chapter, the association of dense gas with molecular outflows was explored. In this chapter, we will investigate the connection between dense gas and YSOs in the active (outflows present) vs. quiescent (no evidence of outflow activity) parts of the Mon OB1 cloud. We wish to determine if the detection of CS gas is better correlated with the presence of energetic outflows, or with the presence of luminous infrared sources heating the surrounding dust, which in turn heats the gas. The results of the last chapter indicate that outflows may play a more important role in the temperature, density structure, and energetics of molecular clouds than previous studies suggest, so it is natural to compare the cloud core structure around active sources to that around quiescent sources.

4.2. IRAS Sources

4.2.1. Central Object SEDs

Lada and Wilking (1984) and Lada (1987) found that the spectral energy distributions (SEDs) of YSOs between 1 and 100 microns fall into three distinct classes. If a spectral index is defined as $\alpha = d \log \lambda F_{\lambda} / d \log \lambda$,

Class I sources have SEDs broader than a single blackbody function for which α is positive. These sources derive their steep positive spectral slopes from the presence of large amounts of circumstellar dust and are generally not detectable at visible wavelengths. Class II sources have SEDs broader than a single blackbody function for which α is negative. These sources generally are observed in the optical as well. Class III sources have SEDs comparable in width to single blackbody functions for which α is negative, consistent with energy distributions expected for reddened photospheres of young stars.

Margulis placed the IRAS sources in Mon OB1 in an evolutionary sequence based on the observed SEDs according to this convention. He was able to classify 27 of the 30 sources, of which he found 18 Class I, 6 Class II, and 3 Class III objects. Sixteen of these objects showed indications of being multiple sources.

4.2.2. Association of Dense Gas with Outflows

The CS J=2→1 transition was detected in the vicinity of 20 of the 30 IRAS sources cited in Margulis' thesis. Extended emission was found in the vicinity of 5 CO outflows (B, C, D, O, and H) associated with IRAS sources. I am designating the outflow associated with IRAS 25, which was not mapped by Margulis, outflow "O". Outflow E, associated with IRAS 11, was only marginally detected in CS. Outflow F, which may be associated with IRAS 14, was not detected in CS. No CS was detected to the 150 mK level in the vicinities of the CO outflows A, G, and I. These outflows are

not associated with *detectable* IRAS sources, although, faint CS emission has been mapped in a region offset from outflow G by Margulis et. al. (1990). They find two $2\ \mu\text{m}$ sources which may be physically associated with the outflow. The remaining 15 CS detections were not noticeably extended, but rather isolated regions in the immediate vicinity of the IRAS sources. Although the detection of CS in the vicinity of the most massive and/or most luminous outflows might be expected, and was in fact observed (with the exception of outflow G), there was no apparent correlation of IRAS source luminosity and the detection of CS. Rather, certain portions of the cloud which do contain IRAS sources appear to be deficient in dense gas. Notably, there was no CS detection at the position of the second brightest IRAS source in Margulis's surveyed region, IRAS 18, which is outshone only by IRAS 9, Allen's IRS. It is rather interesting that this region of the Mon OB1 cloud is apparently rather quiescent; that is, there is a notable lack of CO outflow activity in this region.

Figures (4.1) to (4.4) are plots of the CS integrated intensity and peak temperature vs. IRAS luminosity and IRAS ($12\mu/25\mu$) temperature. Points are included for 29 of the 30 IRAS sources (no temperature or luminosity was assigned to IRAS 4 by Margulis). Sources associated with a CO outflow are marked with the corresponding letter. Upper limits are used for CS integrated intensities and peak temperatures for the 10 IRAS sources which were nondetections at the 150mK level. The integrated intensity of the CS $2\rightarrow 1$ line is considerably greater in the vicinity of the IRAS sources associated with CO outflow, with the exception of the two weaker CO outflows E and F. Where CS was detected about quiescent sources,

the integrated intensity is significantly lower and displays no apparent correlation to the luminosity or temperature of the IRAS source. It might be expected that the outflows would broaden the lines in active regions, however it is interesting to note that the peak CS temperatures are also significantly greater in these regions, implying that the outflows heat the gas, CS abundances are enhanced in these regions, densities are enhanced in the swept-up outflow shells, or some combination of these factors. The one source not associated with an outflow which displays a high CS temperature and integrated intensity (IRAS 5) lies within the general outflow region in the SCL. In fact, this source is located in the southernmost extension of the CS gas, at the boundary of the extended outflow region identified by Margulis. It is also possible that IRAS 5, not IRAS 6, is the driving source of outflow B.

Figs. 4.1. - 4.4. CS $2\rightarrow 1$ integrated intensity vs. IRAS luminosity, CS $2\rightarrow 1$ peak temperature vs. IRAS luminosity, CS $2\rightarrow 1$ integrated intensity vs. IRAS ($12\mu/25\mu$) temperature, and CS $2\rightarrow 1$ peak temperature vs. IRAS ($12\mu/25\mu$) temperature for the 30 IRAS sources in Mon OB1. Sources associated with an outflow are labelled with the corresponding letter. The outflow associated with IRAS 25 is labelled "O".

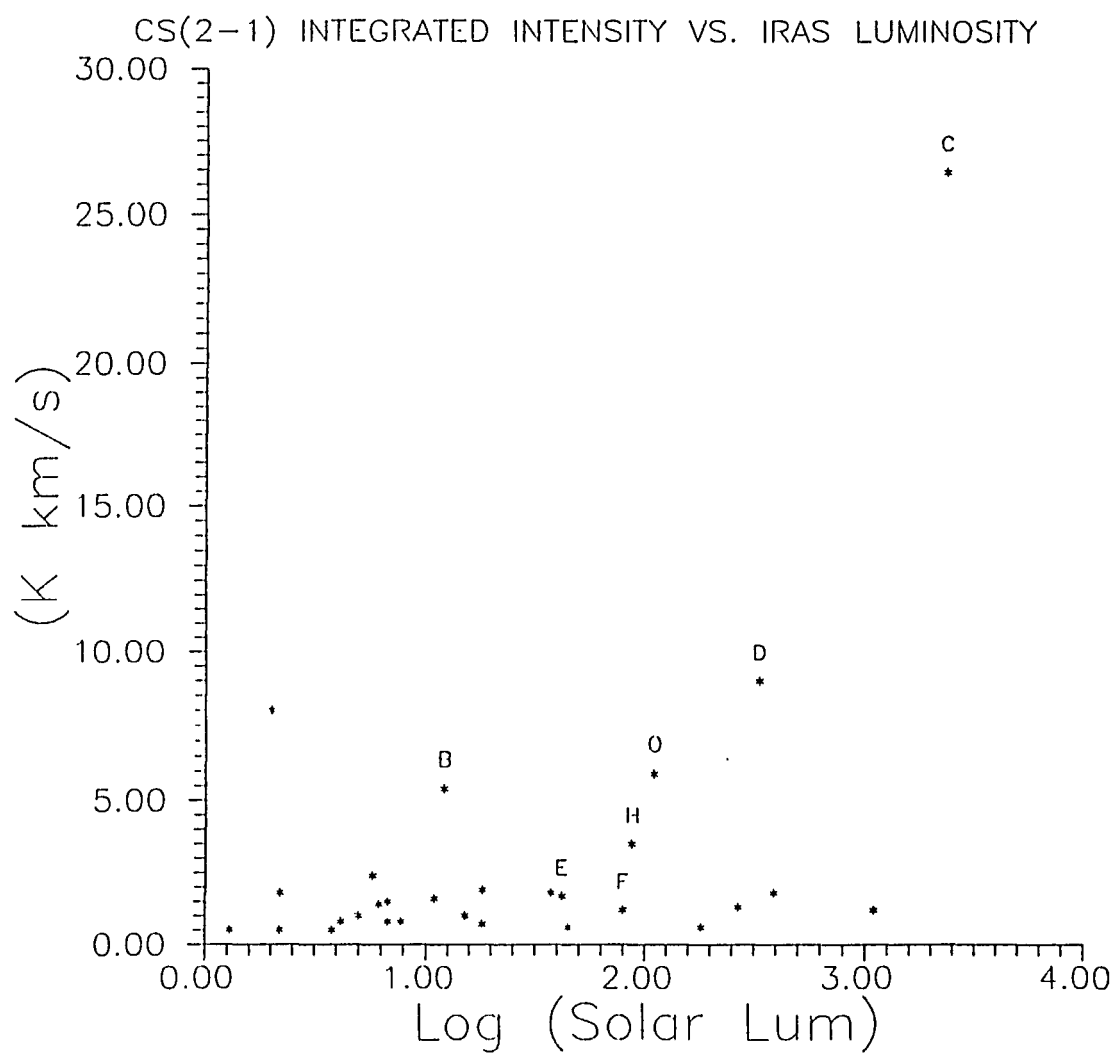


Figure 4.1

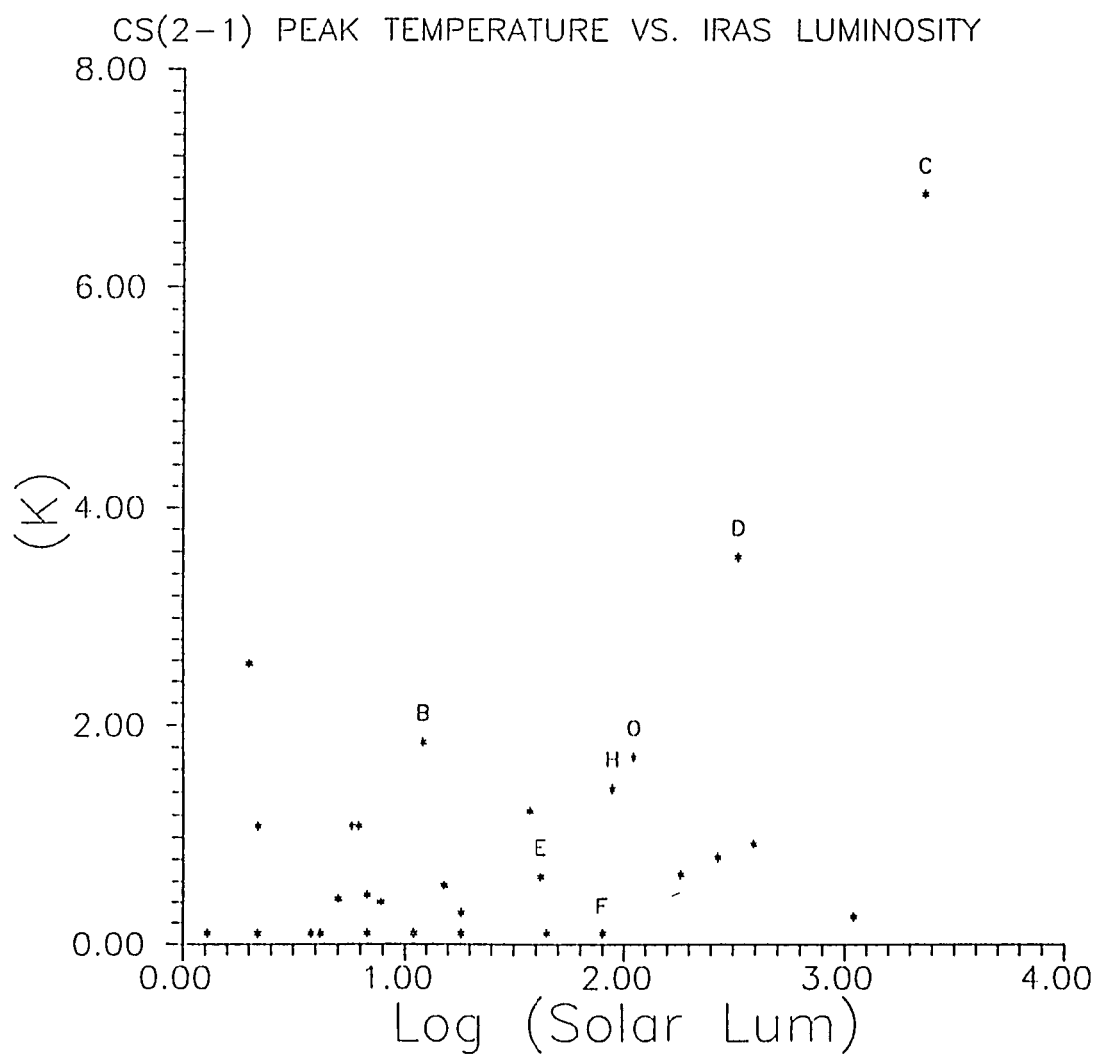


Figure 4.2

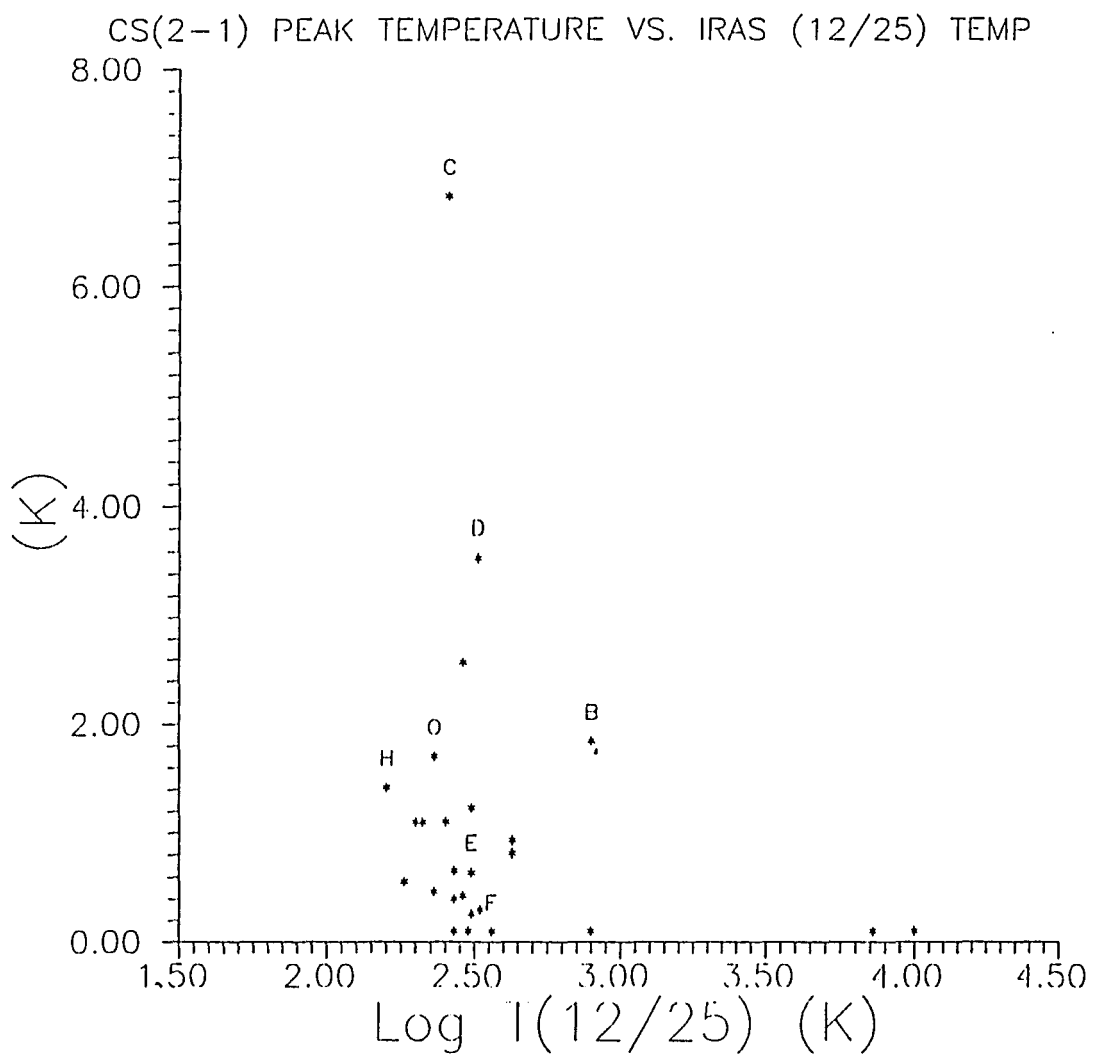


Figure 4.4

4.2.3. Relationship of Outflow to YSO Evolutionary Stage

Margulis found most of the outflows to be associated with Class I objects and a few to be associated with Class II objects. This relationship suggests the outflow phase occurs late in the Class I stage or early in the Class II stage. Of the 5 outflows detected in CS, only B is possibly associated with a Class II driving source. Inspection of Figures (4.1) to (4.4) indicates that the IRAS source associated with outflow B is hotter and less luminous than the sources associated with the other outflows, which is consistent with a more evolved object. The two hottest objects, near $\log T(12\mu/25\mu)=4$, are Class III objects, presumably foreground M giants.

Considering only the Class I sources with outflow, an increase both of CS integrated intensity and peak temperature with IRAS luminosity is apparent. In general, there is a correlation of source luminosity with outflow mechanical luminosity (Bally and Lada, 1983), so it is not surprising that the CS integrated intensity increases with IRAS luminosity. The increase observed in peak temperature may give an indication of the efficiency with which outflow energy is deposited in the ambient cloud and/or indicate higher CS production in the vicinity of the more energetic outflows, since CO outflow mechanical luminosity increases from outflows H to D to C. In fact, the ratio of CO mechanical luminosity for outflows C:D:H scales roughly with the ratio of the CS temperatures for these sources.

The CS integrated intensity and peak temperature are higher for the source associated with outflow B than expected for the relatively low luminosity of the source. This may be related to this source being older

and hotter than the Class I sources, or may be because outflow B lies close to the more luminous outflows C and D in the SCL, where a lot of gas has been swept up, and, perhaps the production of CS enhanced by the outflow activity. Also, there is no reason to expect that the sources associated with outflows H and O, which lie in the NCL, should follow the same trend as the SCL sources as the conditions in the two clouds may be different. Certainly, there is less mass and mechanical luminosity involved in the outflow activity occurring in the NCL. To investigate realistically the differences between different class objects, a much greater sample is required.

Tables (4.1a) and (4.1b) give a summary of the CS $2\rightarrow 1$ emission detected near the IRAS sources and outflows in Mon OB1. Table (4.1a) indicates the IRAS sources (numbers) and outflows (letters) which were detected above the rms noise level (typically ~ 150 mK). Column 4 identifies IRAS sources with outflows and vice versa. Table (4.1b) lists CS line parameters (peak temperature, velocity with respect to the local standard of rest, and linewidth) and approximate sizes of the regions over which CS was detected. These sizes are very approximate; where a detection was part of the two extended emission regions, the approximate size of the sub-clump in which the source lies is given. Sources which were essentially single detections are listed as the approximate size of one beamwidth ($1'$). For the two IRAS sources (4 and 5) associated with the faint southeastern extension of the SCL, the size of this extension is given. CS lines are approximately twice as broad in the outflow as opposed to the quiescent regions of Mon OB1.

TABLE 4.1.a. CS 2→1 DETECTIONS IN MON OB1

Source	$\alpha(1950)$	$\delta(1950)$	Assoc.	Source	CS?
1	$6^h39^m22^s$	$9^\circ13'15''$	No		Yes
2	$6^h39^m28^s$	$9^\circ15'00''$	No		Yes
3	$6^h37^m08^s$	$9^\circ18'29''$	No		No
4	$6^h38^m38^s$	$9^\circ24'15''$	No		Yes
5	$6^h38^m25^s$	$9^\circ27'30''$	No		Yes
6	$6^h38^m28^s$	$9^\circ29'00''$	B		Yes
7	$6^h37^m45^s$	$9^\circ29'30''$	No		Yes
8	$6^h37^m06^s$	$9^\circ31'59''$	No		No
9	$6^h38^m26^s$	$9^\circ32'30''$	C		Yes
10	$6^h36^m50^s$	$9^\circ38'14''$	No		Yes
11	$6^h37^m48^s$	$9^\circ38'30''$	E		Yes
12	$6^h38^m18^s$	$9^\circ39'04''$	D		Yes
13	$6^h38^m59^s$	$9^\circ40'30''$	No		Yes
14	$6^h37^m33^s$	$9^\circ42'29''$	F		No
15	$6^h38^m00^s$	$9^\circ43'45''$	No		Yes
16	$6^h38^m09^s$	$9^\circ46'00''$	No		No
17	$6^h39^m04^s$	$9^\circ50'00''$	No		No
18	$6^h37^m51^s$	$9^\circ50'15''$	No		No
19	$6^h37^m36^s$	$9^\circ51'59''$	No		Yes
20	$6^h38^m18^s$	$9^\circ52'00''$	No		Yes
21	$6^h37^m51^s$	$9^\circ55'00''$	No		Yes
22	$6^h37^m14^s$	$9^\circ55'43''$	No		Yes
23	$6^h38^m09^s$	$9^\circ58'00''$	No		No
24	$6^h37^m29^s$	$10^\circ16'44''$	No		No
25	$6^h38^m17^s$	$10^\circ18'00''$	O		Yes
26	$6^h38^m20^s$	$10^\circ29'30''$	No		Yes
27	$6^h38^m13^s$	$10^\circ39'45''$	H		Yes
28	$6^h37^m13^s$	$10^\circ53'59''$	No		No
29	$6^h38^m09^s$	$10^\circ59'30''$	No		Yes
30	$6^h38^m33^s$	$11^\circ03'01''$	No		No
A	$6^h39^m58^s$	$9^\circ16'20''$	No		No
B	$6^h38^m37^s$	$9^\circ27'40''$	6		Yes
C	$6^h38^m26^s$	$9^\circ32'00''$	9		Yes
D	$6^h38^m19^s$	$9^\circ37'32''$	12		Yes
E	$6^h37^m40^s$	$9^\circ39'31''$	11		Yes
F	$6^h37^m22^s$	$9^\circ40'40''$	14		No
G	$6^h38^m27^s$	$9^\circ58'28''$	No		No
O	$6^h38^m17^s$	$10^\circ18'00''$	25		Yes
H	$6^h38^m17^s$	$10^\circ39'56''$	27		Yes
I	$6^h38^m19^s$	$10^\circ52'39''$	No		No

TABLE 4.1.b. CS 2→1 LINE PARAMETERS

Source	$T_R^*(\text{CS})$ (K)	Size (')	V_{LSR} (km s ⁻¹)	ΔV_{FWHP} (km s ⁻¹)
1	0.56	2	8.5	1.9
2	0.47	2	7.8	1.7
4	1.75	5	8.0	1.3
5	2.57	5	6.5	3.6
6	1.84	5	7.1	2.9
7	0.40	1	6.0	1.8
9	6.84	5	7.9	4.0
10	1.10	2	3.5	1.2
11	0.64	1	4.9	3.4
12	3.54	5	5.3	3.4
13	0.30	1	6.5	2.5
15	0.43	1	5.7	1.8
19	1.10	2	10.6	1.2
20	0.81	1	8.5	2.0
21	0.93	2	11.0	1.3
22	0.66	1	10.3	1.0
25	1.70	3	7.8	2.5
26	1.23	2	8.2	1.7
27	1.42	7	7.8	2.7
29	1.10	1	5.4	1.0
B	1.82	5	7.1	2.9
C	6.84	5	7.9	4.0
D	3.92	5	6.4	4.4
E	0.28	1	5.0	3.0
O	1.70	3	7.8	2.5
H	1.42	7	7.8	2.7

4.3. Summary

Both the CS integrated intensity and peak temperature are enhanced about the IRAS sources associated with outflow. There are several possible explanations for this:

- (1) Gas densities are enhanced as a result of the outflow sweeping-up and entraining ambient molecular cloud material.
- (2) Ambient gas temperatures are enhanced by outflows.
- (3) CS abundances are enhanced in outflow regions in accordance with predictions of shock chemistry (Thronson and Lada, 1984).

Possibly some combination of the above effects holds true.

For IRAS sources unassociated with outflow activity, there appears to be no relationship between either integrated CS intensity or peak temperature and either IRAS source luminosity or temperature. There does, however, appear to be a relationship between both integrated CS intensity and peak temperature and IRAS source luminosity for the outflow-associated sources, although no correlation with IRAS source temperature is apparent. One might expect that more luminous sources would be able to drive more luminous outflows, however the luminosity of a YSO is not well-reflected by its temperature during the early evolutionary stages since the luminosity is dominated by accretion.

The implication of these plots is that the CS temperature and integrated intensity are regulated by the outflows rather than gas heating by warm dust surrounding the IRAS sources. In the next chapter, we will discuss the energy input of outflows into the molecular cloud and explore

the question of multiple generations of outflows.

CHAPTER 5

IMPACT OF OUTFLOWS ON CLOUD EVOLUTION

5.1. Introduction

The lifetimes of molecular clouds tend to be much greater than typical free-fall timescales for such clouds. This has raised the important question of how clouds are supported against large-scale collapse, and whether or not outflows play a principal role in supporting clouds. That is, whether outflows can impart sufficient energy into clouds at high enough efficiencies to support them against collapse. Other related questions regarding early stellar evolution which are not yet well understood include whether YSOs undergo multiple outflow phases, and whether a large fraction of old outflow episodes remains undetected due to the slowing down of outflows as they age.

In this chapter, I will discuss the overall contribution of outflows to cloud dynamics. I will investigate the implications of a significant dense, low-velocity outflow component on cloud energetics and discuss the possibility of multiple and/or old generations of outflows, which may be identified as “fossil” outflows, remnants of previous outflow episodes. I will address the question of cloud support by outflows.

5.2. Outflow Component within Spectral Line Cores

A large fraction of outflow gas may be indistinguishable from the ambient molecular cloud gas because its velocity lies in the core region of the spectral line used to probe the gas. Some of this gas is masked by the line core because of outflow geometry and projection effects, and some of this gas has simply been slowed down as more and more material is swept up and accumulated by the outflow. We have shown that a large fraction of the outflow gas does lie at velocities low enough to be masked by the CO line cores. In fact, the velocity centroid plot of the outflow D region (Figure 3.23a) implies a significant fraction of the outflow gas lies within the CS line core as well. A definite detection of blueshifted outflow gas in CS where no blueshifted outflow was evident in CO, around outflows B and C, suggests that many “monopolar” outflows may actually be bipolar, with outflow gas masked by ambient gas in the line core. There are several possibilities why redshifted CO outflows dominate in Mon OB1. These possibilities will now be discussed.

The existence of a dense, low-velocity component in the outflows in the SCL may be a result of the ambient density structure in this region. Since Allen’s IRS is a deeply embedded object ($A_v \geq 26$ mag in this part of the cloud), it is possible that the blueshifted gas is impeded by denser foreground gas (if Allen’s IRS is located near the backside of the cloud, for example). Conservation of momentum would require that the more mass swept up, the slower the outflow. Consequently, there may be little blueshifted gas at velocities high enough to be seen as line wings in CO. The blueshifted CS was detected at velocities within the line cores of the CO gas.

This possibility is somewhat supported by the velocity extent in the red and blue wings of those outflows which were observed to be bipolar in the CO spectra. The CO spectra in Figure (3.11) which were obtained near the peak blue- and redshifted emission of outflow H show the redshifted gas to be much more extended in velocity than the blueshifted gas.

One would expect the most marked differences in the distribution of higher and lower velocity outflow gas to be apparent in the oldest outflows, where a large fraction of material has been swept up into lower velocity shells. The angular size of the low velocity shells should be greater than that of the region in which high velocity gas is detected. For the Mon OB1 cloud, the oldest and spatially most extended outflow is outflow D. Inspection of the CS wing, channel, and LV maps indicates that not only is there a substantial amount of high density gas participating in this outflow, but the low velocity core emission traces the shell of the outflow and encompasses the high velocity gas, at least at the inner boundary near IRAS 12. The size of the CO outflow relative to the northern clump in the SCL suggests the outflow is “breaking out” of the core. Presumably, densities are too low at the northern boundary of outflow D to excite the CS gas. At the opposite end of the SCL, the redshifted gas associated with outflow B defines the southeastern boundary of this region. Comparison of the CO and CS red wing maps indicates the CS emission traces the boundary of the CO emission. The elongation of the CS $2 \rightarrow 1$ emission, which is not seen in either the $\text{NH}_3(1,1)$ or CS $3 \rightarrow 2$ maps presented in Chapter 3, suggests the morphology of this region is primarily due to outflow B.

5.3. CS vs. CO Outflow Parameters

Table 5.1 compares the CS and CO outflow parameters. The low-velocity components of the SCL outflows contain a large fraction of the total mechanical luminosity of the outflows, due to the large amount of mass involved.

In the NCL, the binding energy ($\Omega = c_1 GM^2/R$) of the “cylinder” structure is $\sim 10^{45}$ erg. Using the upper limit to the CO mechanical luminosity, the CO outflow energy ($L \times \tau_d$) is $\sim 10^{46}$ erg. It will be shown that the upper limits to the outflow parameters based on the CO analysis are extremely conservative. Even if the lower limit is used, the outflow energy is of the same order of magnitude as the core binding energy, implying the outflow is significantly disrupting the core. This may explain the curiously elongated appearance of the CS structure. The major axis of the CO outflow is oriented along a N - S direction. The core geometry appears to be that of a cylinder whose length is longer than its diameter. The outflow has apparently interacted with and expanded the parent molecular cloud core.

TABLE 5.1. COMPARISON OF CO & CS OUTFLOW PARAMETERS

MON OB1 SOUTH CLOUD

Outflow	τ_d (yrs)	M (M_\odot)	MV ($M_\odot \text{ km s}^{-1}$)	L (L_\odot)
B (CO)	4.2×10^4	1.4 - 2.9	7.4 - 26	.056 - .44
C	1.1×10^4	1.6 - 7.2	11 - 150	.32 - 25
D	6.9×10^4	16 - 30	92 - 520	.36 - 11
B (CS)	1.0×10^5	29 - 98	158 - 518	.68 - 2.3
C	9.5×10^4	98 - 233	608 - 1410	3.1 - 7.2
D	1.7×10^5	248 - 323	975 - 1283	35 - 40
MON OB1 NORTH CLOUD				
H (CO)	1.2×10^4	1.6 - 2.3	17 - 53	1.1 - 8.2
	v_{rot} (km s^{-1})	M (M_\odot)	n_{avg} (cm^{-3})	Ω (erg)
CYL (CS)	1.0	161 - 266	1.7×10^4	4.2×10^{45}

5.4. Interaction of Outflows with Cores

In Chapter 3, I suggested that outflows C and D might be responsible for perturbing the CS 5→4 and 7→6 cores. The binding energies of the 5→4 and 7→6 cores may be compared to the outflow energies to determine the extent to which the outflows are likely to affect the cores. If the LTE masses are used, the binding energies of the core regions defined by the 7→6 and 5→4 data for Allen's component, and the 5→4 data for the NW component, are 2.7×10^{44} erg, 2.0×10^{44} erg, and 8.9×10^{43} erg, respectively. If the virial masses are used, then the binding energies are 2.1×10^{46} erg, 4.2×10^{46} erg, and 2.4×10^{46} erg, respectively. Neglecting the CS outflow component, the energies of outflows C and D are 3.3×10^{46} erg and 9.2×10^{46} erg, respectively, using the CO upper limits. We use the upper limits because they include a correction for the outflow material masked by the CO line cores, which, based on the CS results, is extremely conservative. At best, the CS core binding energies are of the same order of magnitude as the outflow energies, but more likely they are smaller by a couple of orders of magnitude. This implies the cores have been disrupted by the outflows and may explain the chaotic velocity structure in these regions.

Figure (5.1) is a composite of spectra averaged over the "cylinder" in the NCL. This average was produced by summing the spectra which are aligned in velocity, weighted by the integration time divided by the square of the system noise, and dividing by the number of spectra. The self-absorption feature is slightly blueward of the line peak in the composite

spectrum. If the cylinder is rotating but neither expanding nor contracting, one would expect the self-absorption dip would occur at line center for the *composite* spectrum. The shift of the self-absorption dip towards the blue indicates there is a slight residual expansion, consistent with a picture in which the outflow is pushing against and expanding this structure.

5.5. Evidence for Fossil Outflows

Fossil outflows may be defined as swept-up shells which are remnants of outflows no longer being driven. Spectra averaged over the SCL where Margulis detected weak, extended CO emission show no evidence of extended, low-velocity outflow lobes in CS. The blueshifted gas detected at the southern end of the SCL is confined and adjacent to the redshifted outflow B, making it seem likely that this gas is associated more directly with the outflow than the extended region.

Although outflows are expected to become denser as they sweep up more material over their lifetimes, the amount of material they accumulate is, of course, dependent on the density structure of the ambient cloud and how rapidly density decreases away from the cores. The extended CO emission region reaches the edge of the cloud and is not likely to be impacting very dense gas in this region. It is reasonable to expect that the densities may not be high enough to excite the CS $J=2 \rightarrow 1$ transition.

The NCL composite spectrum shows a strong blue wing, which is perhaps composed of two cloud components broader (and less intense) than the component at the ambient velocity of the cloud (Figure 5.2). This

average was performed over the *entire* NCL so the relative intensities of the three components just reflect their overall distribution in the NCL. That is, the clump of material associated with IRAS 25 at the south end of the NCL, and the clump of material at the north end of the NCL both add to the intensity of the “red” component which actually peaks at the ambient cloud v_{LSR} . Figure (5.3) shows integrated intensity maps of the main component, the low velocity blue component, and the high velocity blue component, respectively. It is quite interesting that all these components are definitely spatially distinct, and confined, not extended areas of emission. The main component, which peaks at the ambient velocity of the cloud, shows several peaks: one at the positions of each of the 3 IRAS sources in the NCL (only the region near IRAS 27 is shown in Figure 5.3), one approximately $1'$ west of IRAS 27, and a peak north of IRAS 27 and the CO outflow, which is not obviously related to a “hot spot” or outflow. The low velocity blue component traces the blueshifted side of the cylinder region, and the high velocity blue component coincides with the blueshifted high velocity CO lobe of outflow H and indicates the dense, blueshifted gas entrained in the outflow.

Fig. 5.1. Composite CS 2→1 spectrum over the cylinder region in the NCL. Spectra averaged were aligned in velocity with positional offsets across the rotation axis set to zero. The spectra were weighted by the observing time divided by the square of the system noise, summed, and divided by the number of spectra.

Fig. 5.2. Composite CS 2→1 spectrum over the entire NCL. Spectra averaged were aligned in velocity with positional offsets set to zero over the NCL. The spectra were weighted by the observing time divided by the square of the system noise, summed, and divided by the number of spectra. Since spectra were averaged over the entire NCL, the intensity of the three components reflects only the *relative* strength of these components over the entire region.

Fig. 5.3. CS 2→1 integrated intensity maps of the 3 velocity components in the NCL and the CO outflow H. Contours for the CS maps start at 0.5 K km s^{-1} and increase in steps of 0.5 K km s^{-1} . The velocity ranges used for the NCL RED, NCL LV BLUE, and NCL HV BLUE are $7.2 - 12 \text{ km s}^{-1}$, $5.3 - 7.2 \text{ km s}^{-1}$, and $2 - 5.3 \text{ km s}^{-1}$, respectively. Contours (dashed) for the CO blue wing start at 0.5 K km s^{-1} and increase in steps of 0.5 K km s^{-1} . The velocity range used was $0 - 3 \text{ km s}^{-1}$. Contours (solid) for the CO red wing start at 2.0 K km s^{-1} and increase in steps of 2.0 K km s^{-1} . The velocity range used was $10 - 30 \text{ km s}^{-1}$. The position of IRAS 27 is marked (+). Axes units are in arcminute offsets.

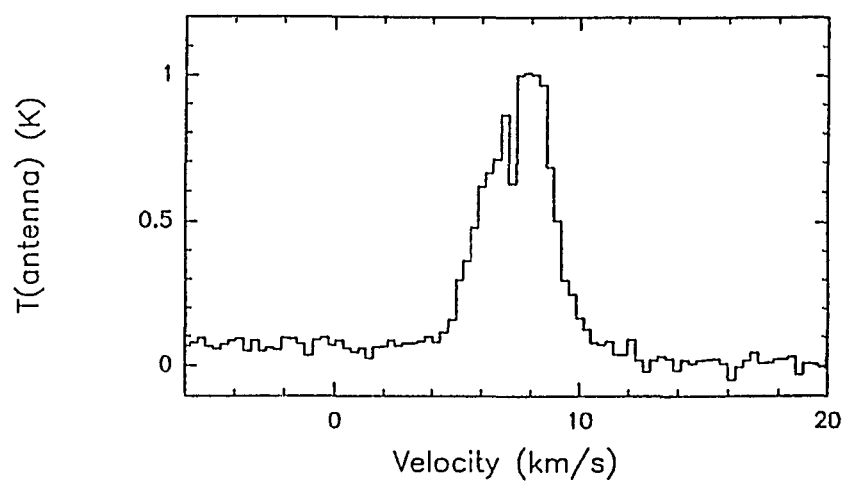


Figure 5.1

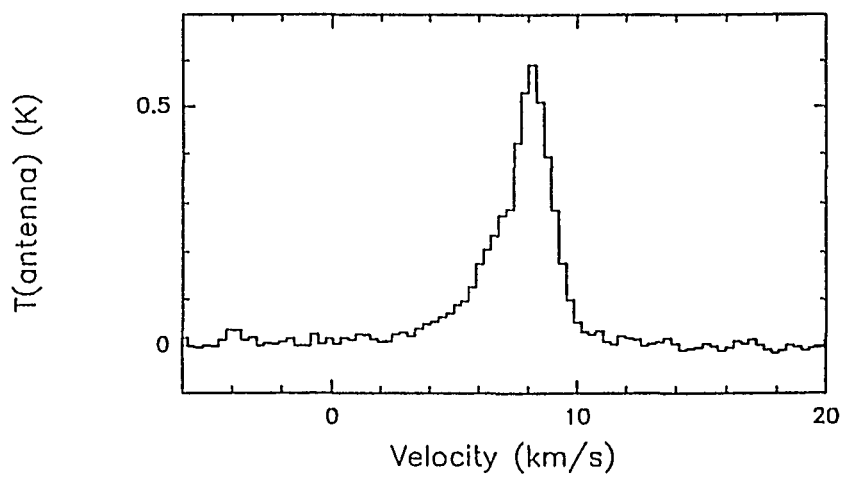


Figure 5.2

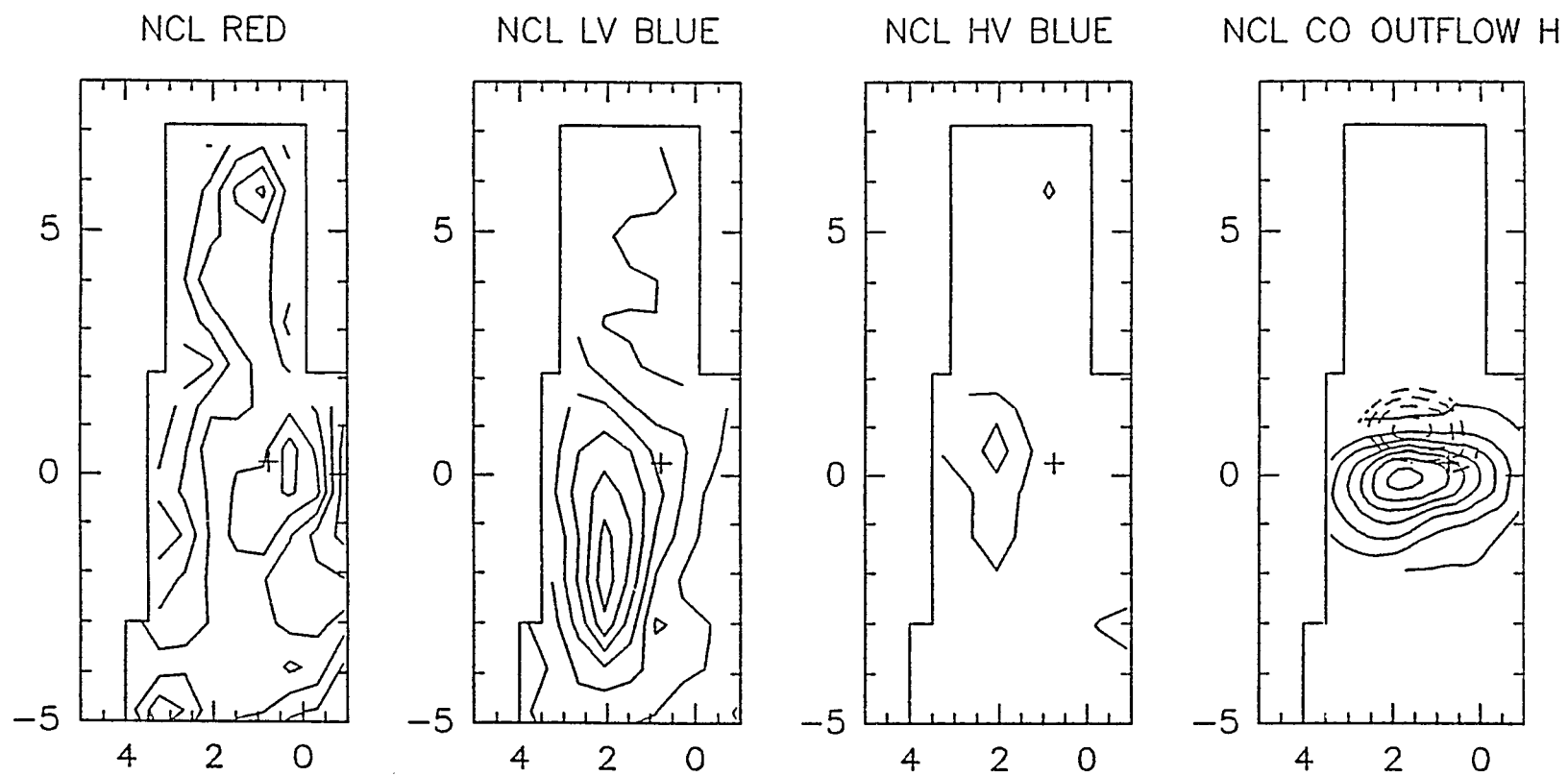


Figure 5.3

5.6. CS Sources Unassociated with CO Flows

Since fossil outflows are expected to be dense, low-velocity shells, it may not be possible to detect them in CO. To investigate properly the relationship of CS gas to potential fossil outflows, a full-cloud survey will be required. However, some general observations may be made based on the CS detections in quiescent regions of this cloud. The sources IRAS 19, 21 and 22 are located in the central, quiescent, region of Mon OB1; in other words, there is no CO outflow activity in this part of the cloud. Based on the CS detections, there is no evidence for fossil outflows associated with these objects. The CS lines are quite narrow (about 1 km s^{-1}) in this region, and the V_{LSR} of these lines is about 10 km s^{-1} , shifted by 2 km s^{-1} from the V_{LSR} of the ambient cloud. Thus, it appears likely that this represents a separate cloud component. As Margulis noted in his thesis, it is possible these sources are young objects which have not yet entered the outflow phase.

5.7. Mass Fraction of Cloud Participating in Outflows

Since the CS survey was biased toward the regions of CO outflow and IRAS sources, it is not possible to determine the amount of dense gas present or entrained in outflow over the extended region of Mon OB1 mapped in CO $1 \rightarrow 0$ by Margulis. However, it is possible to determine the extent to which the dense gas component has been entrained in the regions of the four most massive CO flows. In the SCL, comparing the CS masses

of outflows B, C, and D to the total CS mass of the SCL, we see that approximately 20% - 33% of the dense gas is participating in outflow over the extent of the SCL. This is, in fact, a lower limit since no account was taken for the outflow gas obscured by the *CS line core*.

In the NCL, 25% - 50% of the dense gas appears swept into a cylindrical shell showing evidence of rotation and perhaps, slight expansion. Although we are probably not seeing the remains of the initial circumstellar nebula, clearly much of the ambient dense gas surrounding IRAS 27 has been affected by outflow H. Interestingly, outflow H is the second youngest outflow in the cloud.

5.8. Implications for Cloud Support

Margulis investigated the possibility that the Mon OB1 molecular cloud is supported by the turbulence generated by embedded CO outflows. He found the total mass of outflow gas in the cloud to be 24 - 50 M_{\odot} , only 0.1 - 0.2 % of the total mass of the cloud. However, the total mechanical luminosity was found to be $1.4 \times 10^{34} - 2.5 \times 10^{35} \text{ erg s}^{-1}$. Using a worst-case scenario, in which the outflow driving engines have turned off and the outflows are expanding solely according to momentum conservation, Margulis found that 200 episodes of similar outflow activity should be required to sweep up the bulk of the cloud and accelerate it to highly supersonic speeds. In a more realistic calculation, he accounted for outflow inclination, outflow material at low velocities hidden by the line core, the possibility that additional energy and momentum is still being pumped into the outflows

by their driving sources, and the possibility that turbulent energy may be dissipated from molecular clouds on timescales much longer than their free-fall times. He found that only 40 episodes of outflow activity would be required to sweep the entire Mon OB1 cloud to 1 km s^{-1} and even fewer if the turbulent energy dissipation time is much longer than the free-fall time.

In order to account for the low-velocity material hidden in the line core, Margulis multiplied the total outflow momentum by a factor of 1.4. The CS results in this work indicate this number is conservative to the extreme. Based solely on contributions from the SCL outflows, this estimate is conservative by a factor of about 10 - 20, in which case less than 4 episodes of outflow activity would be required to “pump up” the molecular cloud!

The average CS linewidth in the vicinity of IRAS sources devoid of CO outflow is approximately 1.5 km s^{-1} . However, the average CS linewidth over the regions of CO outflow is about $2.5 - 3.0 \text{ km s}^{-1}$, enhanced by nearly 100% over the quiescent regions! This is significantly greater than Margulis’ findings of 10 - 50% based on the CO and ^{13}CO data, suggesting that the amount of energy being pumped into the dense cores is more than the amount of thermal and dynamical energy present in the absence of outflow.

The CS line widths in the outflow regions are comparable to the ^{13}CO line widths found by Margulis. The CS $5 \rightarrow 4$ line widths about outflow D and the CS $7 \rightarrow 6$ line widths about outflow C are comparable to both the CS $2 \rightarrow 1$ and ^{13}CO line widths in these regions.

5.9. Summary

There is a significant dense, low-velocity outflow component that can be identified with 3 of the CO outflows in Mon OB1. Inclusion of this component significantly reduces the number of outflow episodes required to support this cloud, to the extent that multiple generations of outflows may not need to be invoked for cloud support. The outflows are disrupting their parent cloud cores, which may explain why the virial masses calculated for these regions are systematically higher than the LTE masses.

No evidence is found for fossil outflows in Mon OB1 based on the CS observations in this thesis. However, it must be emphasized that an unbiased, full-cloud survey was not performed. Such surveys are required to fully explore the existence of prior generations of outflows.

CHAPTER 6

SUMMARY AND CONCLUSIONS

The major goal of this work has been to investigate the interrelationship of outflows, YSOs, and dense cores in a single molecular cloud. We chose the Mon OB1 cloud to accomplish this purpose as it has been previously searched for outflows and YSOs.

We will now readdress the goals we stated in the Introduction:

- 1) How do outflows alter their environments and vice versa?
 - a) How strongly do outflows interact with the ambient cloud cores and what is the effect on the structure and dynamics of both outflow and ambient cloud?

Outflows in Mon OB1 are interacting strongly with the dense cores in which they are imbedded. CS linewidths are approximately 100% greater in outflow regions than in quiescent regions of this cloud! CS $2 \rightarrow 1$ line temperatures and integrated intensities are enhanced by factors of 2 to 7 and 2 to 14, respectively, around IRAS sources associated with outflows over quiescent sources. This suggests that CS abundances may be enhanced in regions where outflows impact the ambient cloud. However, as the mass we derived for the SCL is in good agreement with the mass derived by Krügel using the $\text{NH}_3(1,1)$ transition, an anomalous CS abundance is unlikely to have a large effect on our results. Other possibilities for enhanced

temperatures and integrated intensities are density and/or temperature enhancements where the outflow impacts the ambient molecular cloud.

The morphology, velocity structure, and binding energies of the gas traced by the $5 \rightarrow 4$ and $7 \rightarrow 6$ transitions suggest that the cores are being disrupted by the outflows. The $5 \rightarrow 4$ and $7 \rightarrow 6$ cores we mapped in the SCL have radii of 0.1 - 0.2 pc. The morphology of the $7 \rightarrow 6$ region about Allen's IRS suggests that this structure may be a disrupted portion of the original collimating disk. This is supported by the 1.3 mm continuum map of the source (Walker *et al.*, 1990), where the morphology of the inner $30''$ contour is strikingly similar. Even if upper limits to the CS core masses are used and the dense, low-velocity outflow component is entirely neglected, the binding energies of these cores are, at best, the same order of magnitude as the outflow energies. More realistically, the core binding energies are a few orders of magnitude *less* than the outflow energies. In the NCL, the rotating cylindrical structure, which constitutes approximately 25% of the mass of the NCL, is probably the remains of a rotating cloud which has been swept out by outflow H.

- 2) Is there evidence of more than one outflow epoch among individual YSOs?
 - a) Is there evidence of "fossil" outflows?

Our results indicate that less than four generations of outflows may be sufficient to support this cloud against collapse. It is entirely possible that multiple generations of outflows are not required to support clouds

against collapse. We found no evidence of outflow activity or previous episodes of outflow activity among the sources Margulis found to be quiescent in CO. However, this result must be interpreted with caution as a full cloud survey was not carried out. Our results do not rule out the existence of fossil outflows in this cloud. Further large-scale cloud surveys are required to search for fossil outflows and investigate conditions in active and quiescent clouds.

- 3) What percent of the ambient molecular gas has been entrained in outflows?
 - a) How much of the outflow material is moving at low velocities, indistinguishable from the ambient gas when CO is used as an outflow probe?

One major result of this work has been the identification of a very large core component of outflow material which indicates that a high percentage of previously thought ambient gas has been entrained in outflow. The low-velocity outflow material is about ten times as massive as the high-velocity material in the SCL. Previous estimates have assumed the amount of low- and high-velocity material to be comparable. Therefore, previous estimates of outflow masses and energetics may be off by an order of magnitude. Traditionally, molecules which are thermalized only at high densities have been used to probe conditions in dense star-forming cores rather than the more extended, energetic regions of outflow. We have found that the lower rotational levels of CS can be useful tracers of the denser,

low-velocity outflow component. The momentum input of this component to the cloud is 5 - 20 times greater than the high-velocity component. The mechanical luminosities are at worst comparable to, and possibly considerably greater than, the luminosities of the high-velocity outflow component.

We have found evidence that two of the four outflows Margulis found to be monopolar are, in fact, bipolar. Margulis argued that sensitivity might be a factor in the lack of detection of blue wings in the CO data in the regions of these four outflows. Based on our results, it appears that the blueshifted gas associated with outflows B and C in the SCL lies at velocities too low to be distinguished from core emission in the CO data. The morphology of these outflows and the CS and C³⁴S spectra suggest that the bipolarity is real and not caused by intervening cloud components. If the foreground gas density is greater, this would explain why blueshifted velocities are smaller. Also, the blueshifted gas identified with outflow B lies within a denser portion of the SCL in projection than the redshifted gas. That is, the redshifted gas extends to the southeastern limit of the observed CS gas. This result is supported by the CO 2→1 spectrum and outflow map of Krügel et al. (1987), which does indicate slight blue wing emission in the vicinity of IRAS 9 (outflow C). It appears likely that much of the complex velocity structure seen in both the SCL and NCL may be due to the presence of the 4 massive outflows in these regions.

b) Does the large amount of outflow gas moving at low velocities help explain why there appears to be a paucity of outflow activity in certain molecular clouds or in certain regions of molecular clouds,

or has there been no outflow activity in such regions?

Since outflows are seen in all projections against the sky, there may be outflows in this cloud undetected in CO because all of the projected outflow gas is moving at low velocities and cannot be distinguished in the CO line profiles. Alternatively, outflow gas may be moving at low velocities because the outflow slows down as it ages and accumulates more material. As previously stated, we detected no evidence of outflow activity about sources previously found to be quiescent using CO. This question can realistically only be addressed by full-cloud surveys including both active and quiescent regions.

c) Since most of the molecular gas in an outflow is believed to be swept-up ambient gas (eg. Wolf, Lada, and Bally 1990), could lack of sufficient molecular gas in the vicinity of YSOs suggest emission from high velocity gas may just be below present limits of detectability?

Since CS gas was barely, if at all, detected around the IRAS sources not associated with CO outflows, it is possible that lower gas densities in these regions imply a smaller supply of outflow material. However, this is not necessarily the case. Increased CS abundances and temperatures in outflow regions could account for the stronger CS detections. Also, outflow G, which is near the edge of Mon OB1, exhibits a powerful CO outflow, although gas densities are lower in this region. It is quite possible

that outflows associated with the low luminosity sources are below limits of detectability. However, this does not explain why some of the high luminosity young sources do not have outflows. It is more likely that such sources have not yet “turned on”.

CHAPTER 7

SUGGESTED FUTURE WORK

7.1. Unbiased Molecular Cloud Surveys

To study global properties of star formation most effectively, unbiased surveys of individual clouds must be performed. Such surveys are possible on a reasonable timescale given the current generation of high-sensitivity and multi-beam receivers operational at millimeter wavelengths. Data available in the literature suggest that star formation is proceeding quite differently in different molecular clouds. A clear picture of the physical conditions in these clouds must be obtained to understand why this is so. Questions that need to be addressed include:

- (1) What physical conditions distinguish “active” from “quiescent” molecular clouds?
- (2) Do clouds which appear to be quiescent at present exhibit evidence of earlier epochs of outflow activity?

One of the results of this work has been the detection of a large outflow component in the dense, low-velocity gas traced by the CS emission. It is possible that CS is enhanced in such regions. If this is the case, the contribution of the outflow component may be overestimated using a terrestrial CS/H₂ abundance ratio. One way this hypothesis could be tested would be to use a molecular transition whose linewidths tend to be similar

to CS linewidths so that the amount of emission in the line wings might be accurately compared. This could be accomplished using ^{13}CO , which is often found to be optically thin or moderately optically thick in molecular clouds, and C^{18}O for example. This would enable us to determine if CS is overabundant compared to CO, or if the CS emission in outflow regions has more to do with density and temperature enhancements in these regions. The 4 Mon OB1 outflows which were mapped in CS could easily be completely mapped in ^{13}CO , with C^{18}O data obtained at selected points to calculate masses.

7.2. Surveys for Fossil Outflows

Clearly, in order to disentangle the various effects, it would be desirable to study a number of clouds where star formation is progressing differently. One such study would be to survey a “quiescent” cloud, such as ρ Oph, in CS to search for dense, swept-up shells indicative of earlier episodes of outflow activity. Such a survey could be carried out using the CS $2\rightarrow 1$ transition toward a $10' \times 10'$ region of a nearby molecular cloud in only 30 hours of observing time! Detection of very evolved outflows would place important constraints on the timescale over which YSOs participate in outflow activity. On the other hand, if no such indication of old outflows is present in clouds such as ρ Oph, then the question of why certain clouds containing young PMS objects are quiescent must be explored. It is possible that certain physical conditions required for outflow activity are not met in these clouds.

APPENDIX A

My childhood friend and skating companion since 1968, Elisabeth L'Heureux, and her family have been family to me through the years. In fact, all the folks at Fritz Dietl's Ice Skating Arena were in some sense an extended family. I shall always be grateful for the stamina and self-discipline those years of competition taught me. The one family member who made the trip to Arizona with me, Princess (1968 - 1983), was a faithful friend for many years.

I owe a great deal of thanks not only to Steward Observatory, but to the National Radio Astronomy Observatory (NRAO), which employed me during a time of great financial need, as well as helped acquire most of my thesis data, the NOAO folks stationed on Kitt Peak, for companionship during those long operator nights, the Lunar and Planetary Lab (LPL) for the friendships I formed as soon as I arrived in Tucson, as well as many outstanding parties, the Sub-Millimeter Telescope Lab (SMT), particularly Bob Martin, for funding me during my penultimate year at Steward, and to the Flandrau Planetarium for employing me as a console operator during the summer of 1986. Thanks go to Jeff Capara for drawing Figures 3.24 and 3.25 using AUTOCAD.

Many thanks go to my committee, Chris Walker, Charlie Lada, John Black, and Rob Kennicutt, for their support and encouragement. Chris and Charlie have both been outstandingly patient advisors. Thank you, Chris, for rejoining Steward and helping me regain direction after a very dark period in my life. Mike Margulis' dissertation laid the groundwork for the

research in this work.

Special thanks go to the NRAO operators and Phil Jewell for their respective help in data acquisition and observing advice. In particular, (and alphabetically), Dennis Chase, Duane Clark, Lisa Engel, John Fitzner, Tom Folkers, Paul Hart, Werner Scharlach, and Harry Stahl have been instrumental in obtaining some fine thesis data. Paul Rhodes employed me as an NRAO operator for a few years after my funding ran out.

I hope to be attending Bratfests and Bacchanalia at Hawthorne House for a long time to come, even in absentia (I wonder how well Faith Vilas' grasshopper cheesecakes travel...). From Bratfest originators Billy Merline, Nick Schneider, and Gordy Bjoraker, to current tenders of the brats and corn, Mike Nolan, Bob Marcialis, and Bill Bottke, you have all been very special to me.

The Steward grads, LPL grads, and Kitt Peak support group have been a great bunch down through the years, and I am grateful to many of you for your continuing friendship. Just to list a *few* of those individuals whose abilities are matched by their colorful personalities and abilities to enjoy themselves in the face of stress, strain, or overwork: Bill Binkert, Kim Dow, Erica Ellingson, Richard Elston, Bret Goodrich, Tom Greene, Dave Grinspoon, Hal Halbedel, Todd Henry, Eric Hooper, Davy Kirkpatrick, Phil Maloney, Beatrice Müller, Steve Pearce, Valerie and Allen Schiano, Iguana Brother Kevin Schramm, and Peter Tamblyn.

Pat Hartigan taught me to question everything I think I know, never take anything for granted, always derive everything from first principles (well that's the ideal, anyway), and *never ever* believe anyone who claims *anything*

is trivial. Thank you, Pat, for your companionship as well as your unique insights.

There are several people who have been exceptional beyond the ordinary concept of friendship. I'd have to put Liz Alvarez, Rex and Janet Saffer, Mark Sykes, and Chris and Connie Walker on this list. These are some of the most caring and devoted individuals it has ever been my pleasure to know, and each of you is special to me in a different way. From Thanksgiving and Christmas dinners, purple balloons and surprise parties, bananas and whippets, to the opera and belly dancing, I don't think any of you truly realizes the difference having friends like you has made in my life. You have each been an inspiration to me. Don't any of you ever dare skip town without leaving a forwarding address!

Last, but hardly least, I hope Dennis Chase, the one special person whose companionship means more to me than I could ever put down in words, will be a part of my life long after I'm too senile to remember why I spent eleven years in graduate school in the first place.

REFERENCES

- Allen, D. A. 1972, *Ap. J. (Letters)*, **172**, 55.
- Arquilla, R., and Goldsmith, P. F. 1986, *Ap. J.*, **303**, 356.
- Bally, J., and Lada, C. J. 1983, *Ap. J.*, **265**, 824.
- Black, J. H., van Dishoeck, E. F., Willner, S. P., and Woods, R. C. 1990, *Ap. J.*, **358**, 459.
- Blitz, L. 1978, Ph. D. thesis, Columbia University, New York City.
- Blitz, L. 1980, in *Giant Molecular Clouds in the Galaxy*, ed. P. M. Solomon and M. G. Edmunds (New York: Pergamon Press).
- Castelaz, M. W. and Grasdalen, G. 1988, *Ap. J.*, **335**, 150.
- Chini, R., Krügel, E., and Kreysa, E. 1986, *Astr. Ap.*, **167**, 324.
- Crutcher, R. M., Hartkopf, W. I., and Giguere, P. T. 1978, *Ap. J.*, **226**, 839.
- Dickman, R. L. 1976, *Ap. J. Suppl.*, **37**, 407.
- Downes, D., Winnberg, A. Goss, W. M., and Johansson, L. E. B. 1975, *Astr. Ap.*, **44**, 243.
- Draine, B. 1983, *Ap. J.*, **270**, 519.
- Feldbrugge, P. T. M. and van Genderen, A. M. 1991, *Astr. Ap. Suppl.*, **91**, 209.
- Fleck, R. C., and Hunter, J. H. 1976, *M. N. R. A. S.*, **175**, 335.
- Graedel, T. E., Langer, W. D., and Frerking, M. A. 1982, *Ap. J. Suppl.*, **48**, 321.
- Hasegawa, T. 1987, private communication.
- Humphreys, R. M. 1978, *Ap. J. Suppl.*, **38**, 309.
- Krügel, E., Güsten, R., Schulz, A., and Thum, C. 1987, *Astr. Ap.*, **185**, 283.
- Kutner, M. L., and Tucker, K. D. 1975, *Ap. J.*, **199**, 79.

- Lada, C. J. 1985, *Ann. Rev. Astr. Ap.*, **23**, 267.
- Lada, C. J. 1987, in *IAU Symposium No. 115: Star Forming Regions*, eds. M. Piembert and J. Jugaku (Dordrecht: Reidel), 1.
- Lada, C. J. 1988, in *Galactic and Extragalactic Star Formation*, eds. R. E. Pudritz and M. Fich (Kluwer Academic Publishers), 5.
- Lada, C. J. and Wilking, B. A. 1984, *Ap. J.*, **287**, 610.
- Lada, E. A. 1990, Ph. D. thesis, University of Texas, Austin.
- Lada, E. A., Bally, J., and Stark, A. A. 1991, *Ap. J.*, **368**, 432.
- Lada, E. A., DePoy, D. L., Evans, N. J. II, and Gatley, I. 1991, *Ap. J.*, **371**, 171.
- Lang, K. and Willson, R. 1980, *Ap. J.*, **238**, 867.
- Lizano, S., and Shu, F. H. 1989, *Ap. J.*, **342**, 834.
- Loren, R. B. 1977, *Ap. J.*, **215**, 129.
- Loren, R. B. 1981, *Ap. J.*, **249**, 550.
- Loren, R. B., Plambeck, R. L., Davis, J. H., and Snell, R. L. 1981, *Ap. J.*, **245**, 495.
- Loren, R. B., Peters, W. L., and Vanden Bout, P. 1974, *Ap. J. (Letters)*, **194**, 103.
- Maddalena, R. J., Morris, M., Moscowitz, J., and Thaddeus, P. 1986, *Ap. J.*, **303**, 375.
- Margulis, M. 1987, Ph. D. thesis, University of Arizona, Tucson.
- Margulis, M., Lada, C. J., Hasegawa, T., Hayashi, S. S., Hayashi, M., Kaifu, N., Gatley, I., Greene, T. P., and Young, E. T. 1990, *Ap. J.*, **352**, 615.
- Margulis, M., Lada, C. J., and Young, E. T. 1989, *Ap. J.*, **345**, 906.
- Mathieu, R. D., Benson, P. J., Fuller, G. A., Myers, P. C., and Schild, R. E. 1988, *Ap. J.*, **330**, 385.

- Mestel, L. 1985, in *Protostars & Planets II, Magnetic Fields*, edited by D. C. Black and M. S. Matthews (University of Arizona, Tucson), 320.
- Morris, M., Zuckerman, B., Turner, B. E., and Palmer, P. 1974, *Ap. J. (Letters)*, **192**, 27.
- Mouschovias, T. Ch. 1978, in *Protostars and Planets, Formation of Stars and Planetary Systems in Magnetic Interstellar Clouds*, edited by T. Gehrels (University of Arizona, Tucson), 209.
- Myers, P. C., and Goodman, A. A. 1988, *Ap. J.*, **326**, 27.
- Myers, P. C., and Goodman, A. A. 1988, *Ap. J.*, **329**, 392.
- Plambeck, R. L., Snell, R. L., and Loren, R. L. 1983, *Ap. J.*, **266**, 321.
- Pudritz, R. E., and Norman, C. A. 1983, *Ap. J.*, **274**, 677.
- Pudritz, R. E., and Norman, C. A. 1985, *Ap. J.*, **293**, 216.
- Racine, R., and van den Bergh, S. 1970, in *The Spiral Structure of Our Galaxy*, IAU Symposium No. 38, edited by W. Becker and G. Contopoulos (Reidel, Dordrecht), 219.
- Rickard, L. J., Palmer, P., Buhl, D., and Zuckerman, B. 1977, *Ap. J.*, **213**, 654.
- Sagar, R. and Joshi, U. C. 1983, *M. N. R. A. S.*, **205**, 747.
- Sargent, A. I., Van Duinen, R. J., Nordh, H. L., Fridlund, C. V. M., Aalders, J. W. G., and Beintema, D. 1984, *Astr. Ap.*, **135**, 377.
- Schwartz, P. R., Thronson, H. A. Jr., Odenwald, S. F., Glaccum, W., Loewenstein, R. F., and Wolf, G. 1985, *Ap. J.*, **292**, 231.
- Shibata, K., and Uchida, Y. 1985, *Publ. Astr. Soc. Japan*, **37**, 31.
- Shu, F. H., Lizano, S., Ruden, S. P., and Najita, J. 1988, *Ap. J.*, **328**, L19.
- Shibata, K., and Uchida, Y. 1986, *Publ. Astr. Soc. Japan*, **38**, 631.
- Snell, R. L., Loren, R. B., and Plambeck, R. L. 1980, *Ap. J.*

- (*Letters*), **239**, 17.
- Snell, R. L., Mundy, L. G., Goldsmith, P. F., Evans, N. J. II, Erickson, N. R. 1984, *Ap. J.*, **276**, 625.
- Snell, R. L., and Schloerb, F. P. 1985, *Ap. J.*, **295**, 490.
- Solomon, P. M., Huguenin, G. R., and Scoville, N. Z. 1981, *Ap. J. (Letters)*, **245**, 19.
- Spitzer, L. 1978, *Physical Processes in the Interstellar Medium* (Wiley, New York).
- Thronson, H. A. Jr., Harper, D. A., Keene, J. , Loewenstein, R. F., Moseley, H. , and Telesco, C. M. 1978, *Astr. J.*, **83**, 492.
- Thronson, H. A. Jr., Gatley, I. , Harvey, P. M., Sellgren, K., and Werner, M. W. 1980, *Ap. J.*, **237**, 66.
- Thronson, H. A. Jr. and Lada, C. J. 1984, *Ap. J.*, **284**, 135.
- Torrelles, J. M., Rodriguez, L. F., Canto, J. , Carral, P. , Marcaide, J. , Moran, J. M., and Ho, P. T. P. 1983, *Ap. J.*, **274**, 214.
- Uchida, Y. , Kaifu, N. , Shibata, K. , Hayashi, S. , and Hasegawa, T. 1987, in *Star Forming Regions*, IAU Symposium No. 115, edited by M. Peimbert and J. Jugaku (Reidel, Dordrecht), 287.
- Uchida, Y., Kaifu, N., Shibata, K., Hayashi, S. S., Hasegawa, T. and Hamatake, H. 1987, *Publ. Astr. Soc. Japan*, **39**, 907.
- Uchida, Y., and Shibata, K. 1985, *Publ. Astr. Soc. Japan*, **37**, 515.
- Ulich, B. L. and Haas, R. W. 1976, *Ap. J. Suppl.*, **30**, 247.
- Walker, C. K. 1988, Ph. D. thesis, University of Arizona, Tucson.
- Walker, C. K., Adams, F. C., and Lada, C. J. 1990, *Ap. J.*, **349**, 515.
- Walker, C. K., Carlstrom, J. E., Bieging, J. H., Lada, C. J., and Young, E. T. 1990, *Ap. J.*, **364**, 173.
- Walker, M. F. 1956, *Ap. J. Suppl.*, **2**, 365.
- Walker, M. F. 1957, *Ap. J.*, **125**, 636.

- Walker, M. F. 1959, *Ap. J.*, **130**, 57.
- Walker, M. F. 1961, *Ap. J.*, **133**, 438.
- Walker, M. F. 1969, *Ap. J.*, **155**, 447.
- Walker, M. F. 1972, *Ap. J.*, **175**, 89.
- Walsh, J. R., Ogura, K., and Reipurth, B. 1992, *M. N. R. A. S.*, **257**, 110.
- Wolf, G. A., Lada, C. J., and Bally, J. 1990, *Astr. J.*, **100**, 1892.
- Zuckerman, B., Morris, M., Palmer, P., and Turner, B. E. 1972, *Ap. J. (Letters)*, **173**, 125.